NANOSCALE STRUCTURES FOR TUNABLE AND LOW-LOSS RESONATORS

MR. CHEN YIGUO

(B. ENG. (Hons.), NUS)

A THESIS SUBMITTED

FOR THE DEGREE OF NATIONAL UNIVERSITY OF SINGAPORE – IMPERIAL COLLEGE LONDON JOINT DOCTOR OF PHILOSOPHY

DEPARTMENT OF ELECTRICAL AND COMPUTER ENGINEERING

NATIONAL UNIVERSITY OF SINGAPORE

AND

DEPARTMENT OF PHYSCIS

IMPERIAL COLLEGE LONDON

2015

DECLARATION

I, Chen Yiguo, hereby declare that this thesis titled 'Nanoscale Structures for Tunable and Low-Loss Resonators' is my original work and it has been written by me in its entirety. I have duly acknowledged all the sources of information which have been used in the thesis.

Acknowledgements

I would like to express my heart felt appreciation and gratitude to my supervisors, Prof. Hong Minghui, Prof. Stefan A. Maier and Prof. Boris Lukiyanchuk for their invaluable guidance throughout my PhD course, and the opportunities to participate in the wonderful projects with collaborators in the top tier of the nanophotonic community. They also supported my attendance to several international conferences which broadened my horizons and contributed to my research.

It is also my pleasure to express my appreciations to all my lab members in Singapore, Dr. Yang Jing, Dr. Tang Min, Dr. Chen Zaichun, Dr. Xu Le, Dr. Thanh Nguyen, Dr. Luo Fangfang, Dr. Du Zheren, Dr. Qin Fei, Ms. Wu Mengxue, Mr. Wang Dacheng, Mr. Ma Zhijie, Mr. Xu Kaichen, Mr. Liu Hongliang, and Mr. Xu Jianfeng. I would like to thank all the members of the Plasmonic group at Imperial College who were always very approachable and helpful. In particular, Dr. Tyler Roschuk, Dr. Pablo Albella Echave, Dr. Stephen Hanham, Dr. Paloma Arroyo Huidobro, Dr. Adam Gilbertson and Dr. Stéphane Kéna-Cohen. Enormous help was given by Dr. Vincenzo Giannini, Dr. Antonio Fernández-Domínguez, Dr. Mohsen Rahmani, Dr. Joshua Caldwell, as well as Dr. Yannick Sonnefraud. Moreover, I would like to extend my gratitude to Dr. Li Xiong and Prof. Luo Xiangang for their kind help in the collaborated projects.

Most importantly, I must thank Dr. Ng Binghao, Dr. Yan Francescato, Dr. Konstantinos Daskalakis, and Mr. Tarik Abdelmoula for the daily conversations on literally any topics.

Last but not the least, I would like to give my great thanks to my father Mr. Chen Xianqing and my mother Mdm. Xiao Yaqiong. Without their support, I could not have the passion and determination to go so far along my studies.

Contents

DECLARATION i

Acknowledgements ii

Contents iv

Summary vii

List of Tables ix

List of Figures x

List of Publications xiii

1 Introduction 1

1.1 General Introduction 1

1.2 Current Research and Challenges 3

1.2.1 Tunable Plasmonics 3

1.2.2 Low-loss Materials for Plasmonics 5

1.3 Significance and Scope 7

1.4 Organization of Thesis 10

2 Theoretical Background 12

2.1 Surface Polaritons 12

2.1.1 Polaritons 12

2.1.2 Surface Plasmon Polaritons 13

2.1.3 Optical Phonon Polaritons 16

2.2 Localized Surface Polaritons: Resonances of Nano-particles . . . 20

2.2.1 Spectrum of LSPR 21
2.2.2 Quality of a Resonator 23

3 Methods **26**
3.1 Numerical Simulations 26
3.1.1 Finite-Difference Time-Domain 26
3.1.2 Finite Element Method 29
3.2 Sample Preparations 30
3.2.1 Substrate Cleaning 31
3.2.2 Photoresist Coating 32
3.2.3 Thin Film Deposition 32
3.2.4 Laser Interference Lithography 35
3.2.5 Ion Milling 37
3.3 Sample Characterization 39
3.3.1 UV-Vis-NIR Spectroscopy 39
3.3.2 Fourier-Transform Infrared Spectroscopy 40
3.3.3 Scanning Confocal Microscopy 45

4 Tunable Nanoscale Resonators **48**
4.1 Phase-Change Material $Ge_2Sb_2Te_5$ 48
4.2 Tuning Lattice Resonance of Au Disk Array 52
4.2.1 Experimental 52
4.2.2 Results and Discussion 54
4.2.3 Conclusions 56
4.3 Tunable Perfect Absorbers 56
4.3.1 Design and Simulation 57
4.3.2 Results and Discussion 60
4.3.3 Conclusions 63
4.4 Controlling Hotspots in Sub-diffraction Scales 63
4.4.1 Design and Simulation 64
4.4.2 Conclusions 67
4.5 Tuning Resonances of Slits in a Metal Film 68
4.5.1 Resonance of a Single Slit 69

4.5.2 Theoretical Demonstration of the Focus Tuning 72
4.5.3 Numerical Simulation of Planar Lens 79
4.5.4 Experimental Results of the Planar Lens 82
4.5.5 Conclusions 85
4.6 Summary 86

5 Low-Loss Nanoscale Resonators 87
5.1 Silicon Carbide Resonators 88
5.1.1 Experimental 89
5.1.2 Results and Discussion 90
5.1.2.1 Reflection Spectrum of a SiC Substrate 90
5.1.2.2 Localized SPhP Modes in SiC Nano-pillars . . . 91
5.1.2.3 Size and Interpillar Gap Dependence in Square Lattices 92
5.1.2.4 Spectral Tuning of Monopoles with Constant Efficiency 99
5.1.3 Conclusions 101
5.2 Hexagonal Boron Nitride Resonators –from Isotropic to Hyperbolic 102
5.2.1 Introduction to Hyberbolic Materials 102
5.2.2 Optical Properties of hBN 104
5.2.3 Geometry of Nano-patterned hBN 105
5.2.4 Modes of Nano-patterned hBN resonators 107
5.2.4.1 Upper Reststrahlen Band 107
5.2.4.2 Lower Reststrahlen Band 112
5.2.5 Conclusions 115
5.3 Summary 115

6 Conclusions 117
6.1 Conclusions 117
6.2 Future Work 120

References 121

Summary

Light manipulation at the nanoscale, which is known as nanophotonics, has attracted enormous attention. Particularly, metallic nano-resonators, which support localized surface plasmons, have been under intense study. The potential applications of metallic nano-resonators include surface-enhanced spectroscopy, plasmon-enhanced solar energy harvesting, ultra-thin optical components, etc. However, two issues that hinder their applications in real life have long been identified. On the one hand, the optical response lacks tunability once the nano-resonators are fabricated. On the other hand, the large Ohmic losses inherent in noble metals severely limit their performance. In this thesis, these two issues are investigated through both numerical and experimental studies. In the first part, phase-change material $Ge_2Sb_2Te_5$ (GST) is introduced to add tunability to the nano-resonators. GST has a large refractive index contrast between its amorphous and crystalline phases. In this research, it is used as a tunable dielectric environment for the resonators, achieving significant shifts of the resonances. Practical applications, such as hotspot manipulation and phase-front engineering, are studied in detail. In the second part, nano-resonators made of polar crystals (4H-SiC and hexagonal BN) that support phonon polaritons are investigated. Due to the absence of free charge carriers, Ohmic losses are greatly

reduced in these materials. The field enhancements and quality factors of the corresponding resonators are therefore found to be much larger than their plasmonic counterparts. Further analyses of the near-field distributions reveal the natures of the resonances, providing fundamental knowledge for future nanophotonic designs based on phonon polaritons.

List of Tables

3.1 Ultrasonic cleaning recipe 32

4.1 Parameters of planar lenses for comparison 78

4.2 Comparisons of "optimal","quasi-optimal" and "realistic" cases at $W = 32\,\mu m$ 79

List of Figures

1.1 Different methods to achieve tunable plasmonic structures 4

1.2 Identifying low-loss materials for plasmonics 6

2.1 Dispersion relation of surface plasmon polariton 13

2.2 Schematic diagram of an interface between metal and dielectric . 14

2.3 Transverse and longitudinal optical phonons 16

2.4 Permittivity of 4H-SiC 18

2.5 Reflection spectrum and Raman shift of a 4H-SiC flake 18

2.6 Dispersion relation of 4H-SiC 19

2.7 Field enhancement comparison between LSPhP and LSPP 25

3.1 Configurations in FDTD simulations 28

3.2 Configurations in FEM simulations to model an isolated structure 31

3.3 Electron beam evaporator 33

3.4 Sputtering evaporator 34

3.5 Laser-interference lithography setup 35

3.6 Fabricating dots array by using two-step laser-interference lithography 37

3.7 Samples fabricated by laser-interference lithography 38

3.8 Ion-milling system 38

3.9 Spectrophotometer 40

3.10 Interferometer and interferogram 42

3.11 Bruker Vertex 70 FTIR bench 43

3.12 Bruker Hyperion 2000 FTIR microscope 44

3.13 Cassegrain objective lens 45

3.14 Grazing angle objective (GAO) lens 46

3.15 Schematic diagram of a confocal microscope 47

4.1 Optical properties of $Ge_2Sb_2Te_5$ at different crystallization levels 50

4.2 Transmission spectra of $Ge_2Sb_2Te_5$ at different crystallization levels 51

4.3 Schematic diagram of tunable plasmonic disk array 52

4.4 Fabrication steps of tunable plasmonic nano-disk array 53

4.5 Spectral evolution of tunable plasmonic disk array 54

4.6 Schematic drawing of tunable plasmonic absorber 58

4.7 Absorption spectra of tunable plasmonic absorber 59

4.8 Near fields of modes supported by tunable plasmonic absorber . 60

4.9 Absorption and Q-factor as a function of GST crystallization level 61

4.10 The absorption as a function of lattice constant and thickness of SiO_2 layer 63

4.11 Design for hotspot control 65

4.12 Spatial control of hotspots 67

4.13 Spectra of field enhancement at $d = 50\,\text{nm}$ and $d = 500\,\text{nm}$ . . . 68

4.14 Optical properties of a single slit filled with GST 70

4.15 Schematic of planar lens and the model for theoretical calculation 73

4.16 Theoretical calculation of the focus from a point source array . . 75

4.17 Longitudinal focus shifting 80

4.18 Lateral focus shifting 82

4.19 Proof-of-concept demonstration of focus shifting 85

5.1 SEM images of SiC nano-pillar array 90

5.2 Reflection spectra of SiC slab 90

5.3 Reflection spectra of SiC nano-pillar array 91

5.4 Near fields of SiC monopole 93

5.5 Near fields of SiC dipole 1 94

5.6 Near fields of SiC dipole 2 95

5.7 Spectral evolution of SiC nano-pillars arrays in square lattices . . 96

5.8 Spectral positions of the modes supported by SiC nano-pillars arrays in square lattices 97

5.9 SEM image of randomly arranged SiC nano-pillars 98

5.10 Reflection spectra of randomly arranged SiC nano-pillars 98

5.11 Constant modal efficiency of monopolar modes 99

5.12 Charge distribution of isolated monopole 101

5.13 Iso-frequency surfaces of different media 103

5.14 Schematic of hexagonal boron nitride van der Waals crystal . . . 104

5.15 Permittivity of hBN 105

5.16 Typical k-space plot of hBN 106

5.17 Schematic drawing of hBN nanostructure 106

5.18 SEM of boron nitride nanostructures 107

5.19 Spectra of hBN nanostructure in the upper Reststrahlen band . . 108

5.20 Near fields of hBN Nanostructure in the upper Reststrahlen band 109

5.21 Directionality of modes supported by hBN nano-cones in the upper Reststrahlen band 110

5.22 Spectral positions of modes supported by hBN nano-cones in the upper Reststrahlen band 111

5.23 Spectra of hBN nanostructure in the lower Reststrahlen band . . 112

5.24 Near fields of $^{L}TM_{10}$–$^{L}TM_{16}$ modes in the lower Reststrahlen band 113

5.25 Directionality of modes supported by hBN nano-cones in the lower Reststrahlen band 114

5.26 Near fields of $^{L}TM_{01}$–$^{L}TM_{03}$ modes in the lower Reststrahlen band 114

List of Publications

1) **Y. G. Chen**, T. S. Kao, B. Ng, X. Li, X. G. Luo, B. Lukiyanchuk, S. A. Maier and M. H. Hong,"Hybrid phase-change plasmonic crystals for active tuning of lattice resonances," Optics Express *21*, 13691–13698 (2013).

2) T. S. Kao, **Y. G. Chen** and M. H. Hong,"Controlling the near-field excitation of nano-antennas with phase-change materials," Beilstein Journal of Nanotechnology *4*, 632–637 (2013).

3) **Y. Chen**, Y. Francescato, J. D. Caldwell, V. Giannini, T. W. W. Maβ, O. J. Glembocki, F. J. Bezares, T. Taubner, R. Kasica, M. Hong and S. A. Maier,"Spectral Tuning of localized surface Phonon polariton resonators for low-loss Mid-IR applications," ACS photonics *1*, 718–724 (2014).

4) J. D. Caldwell, A. V. Kretinin, **Y. Chen**, V. Giannini, M. M. Fogler, Y. Francescato, C. T. Ellis, J. G. Tischler, C. R. Woods, A. J. Giles, M. Hong, K. Watanabe, T. Taniguchi, S. A. Maier and K. S. Novoselov, "Sub-diffractional volume-confined polaritons in the natural hyperbolic material hexagonal boron nitride," Nature Communication *5*, 5221 (2014).

5) **Y. Chen**, X. Li, X. Luo, S. A. Maier and M. Hong, "A tunable near-infrared plasmonic perfect absorber based on phase-change materials," Photonics Research *3*, 54–57 (2015).

6) **Y. Chen**, X. Li, Y. Sonnefraud, A. I. Fernández-Domínguez, X. Luo, M. Hong and S. A. Maier, "Engineering the phase front of light with phase-change material based planar lenses," Scientific Reports *5*, 8660 (2015).

7) A. M. Gilbertson, Y. Francescato, T. Roschuk, V. Shautsova, **Y. Chen**, T. P. H. Sidiropoulos, M. Hong, V. Giannini, S. A. Maier, L. F. Cohen and R. F. Oulton, "Plasmon-induced optical anisotropy in hybrid graphene-metal nanoparticle systems," Nano letters *15*, 3458-64 (2015)

8) A. Pusch, A. D. Luca, S. S. Oh, S. Wuestner, T. Roschuk, **Y. Chen**, S. Boual, Z. Ali, C. C. Phillips, M. Hong, S. A. Maier, F. Udrea, R. H. Hopper and O. Hess, "A highly efficient CMOS nanoplasmonic crystal enhanced slow-wave thermal emitter improves infrared gas-sensing devices," Scientific Reports, Accepted on 23 Sep 2015.

Chapter 1

Introduction

1.1 General Introduction

Since the pioneering work of Wood on grating anomalies and Ritchie on surface plasmon polaritons supported in thin metallic foils [1, 2], an increasing attention has been devoted to the manipulation of light at the nanoscale, known as nanophotonics. Nanophotonics requires therefore an ability to confine light into sub-diffractional volumes. Plasmonics, which describes the interaction between electromagnetic field and free electrons, has proven to be a promising solution in that context. With the advances in nano-fabrication techniques, nanostructures of complex designs have become feasible, and their interesting properties have led to many promising applications. In particular, the demonstration of guided surface plasmons launched the fields of integrated plasmonic circuits and optical computing, which are able to operate at a much higher speed and in a much smaller volume compared with the electronic counterparts. Plasmon-enhanced

devices for displays and telecommunications have also been proposed by companies to boost the performance of their current products. The photo-thermal effect of metallic nanoparticles has been used successfully to kill cancer cells [3], and the strong localized electric field of nanoparticles is essential for surface-enhanced spectroscopy and nanolasing [4, 5]. More recently, various cloaking and super-resolution imaging methods based on plasmonics have been demonstrated with tailored refractive properties and phase fronts [6–13].

However, despite the significant efforts undertaken within this research field, the promises for many applications have remained unfulfilled. This stems from two issues associated with plasmonics. One is the fixed optical response once the geometries, materials, and substrates of the nanostructures are chosen [14]. This hinders the application of plasmonics in practical devices that require fine tuning or real-time shifting of a resonance. The other one is the relatively large optical losses inherent in metals due to their Ohmic nature [15, 16]. The charge transport in plasmons suffers from fast scattering, which is inevitable and severely limits the performance [15, 17–20]. A variety of ideas has been proposed to overcome these difficulties. Some of them will be highlighted in the following sections.

1.2 Current Research and Challenges

1.2.1 Tunable Plasmonics

Current solutions aimed at achieving tunable plasmonics include varying the geometries in situ or modulating electrical and dielectric properties of the components of a system.

Geometric tuning can be realized by micro-electro-mechanical systems (MEMs) upon electrical signals [21, 22]. Such systems use electrostatic forces to control distances between elements, which result in a varied resonant strength and frequency. An example is shown in Fig. 1.1 a. As the voltage bias is applied to the suspended layer and the ground plane, an electrostatic force brings them into contact, causing the resonance of the structure to be tuned. Another geometric tuning mechanism is based on bilayer structures consisting of two materials with different thermal expansion coefficients [23, 24]. In response to a thermal stimulus, out-of-plane bending takes place, causing the geometries to be altered. These approaches usually involve complicated and bulky geometries which are difficult to be fabricated, and the modulation rates are low due to the slow response of the physical change.

The electrical properties of graphene and doped semiconductors can be changed by modulating their charge carrier concentrations via electrical signals or optical excitations. By placing such materials in the vicinity of plasmonic structures, plasmonic resonances can be tuned due to the conductivity change of the system. Several works have demonstrated the modulations of plasmonic resonances under

this scheme (see Fig. 1.1 b) [25, 26]. In a work by J. Gu, semiconductors are placed inside the gap regions of split-ring resonators, serving as tunable resistors inside the capacitors [27]. Fast tuning of the optical response based on these designs has been proven. However, as shown in Figs. 1.1 d–e these methods behave like a switch, which controls the intensities of the plasmonic resonances, instead of spectrally shifting them.

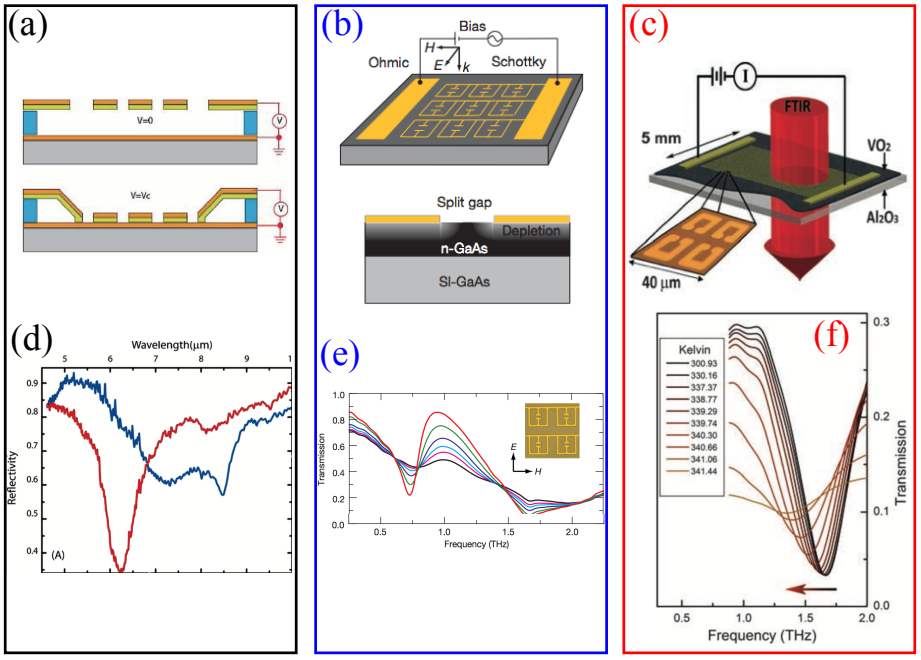

FIGURE 1.1: (a) Schematic of micro-electro-mechanical systems to achieve tunability via electrostatic forces. (b) A layer of semiconductor is used to tune the resonances of the plasmonic structures via modulating the carrier density. (c) Phase-change material VO_2 is used to change the resonances of the split-ring resonators. Figures (d)–(f) show the corresponding optical modulations of the proposed solutions. Significant modulations of intensity are observed, but efficient frequency tuning is missing. (a) and (d) are reprinted from [22], (b) and (e) are reprinted from [25], (c) and (e) are reprinted from [28]

Recently, phase-change materials have been used to serve as a tunable dielectric environment, modulating the resonances of plasmonic resonators in the vicinity (see Fig. 1.1 c). Phase-change materials are a group of materials that support variable atomic arrangements (also termed as phases), and different phases can

be switched easily by external stimulus, such as an electric current, optical pumping and direct heating. Two phases are widely considered, namely amorphous and crystalline phases. Amorphous phase refers to the case that atoms are randomly arranged, while crystalline phase means highly ordered atomic arrangements. The optical contrast associated with the two phases can be significant in some phase-change materials. Vanadium dioxide (VO_2) and gallium lanthanum sulphide have been investigated under this scheme [28–31]. Significant spectral shifts of the resonances have been demonstrated. However, losses of these phase-change materials are high in their crystalline phase. For instance, in the work from M. Dicken [32], a layer of 60 nm thick VO_2 in the crystalline phase completely screens the plasmonic resonance. Although the use of phase-change materials is promising, better choices of phase-change materials need to be found, and proper structures that can effectively utilize the phase-change properties are required.

1.2.2 Low-loss Materials for Plasmonics

The other issue considered in this thesis is the losses associated with nanophotonics. Because plasmonics has the capability to achieve subwavelength confinement, it lays the basis of nanophotonics. Plasmonics relies on free electrons in metals to interact with incident light. Major contributors to intrinsic losses in metals include electron-electron scattering, electron-phonon scattering and interband absorption. This issue renders a broad resonance with limited electric field enhancement, making plasmonics fail to deliver the expected performance

in applications such as sensing. To tackle the loss issue, potential lower-loss materials with less electron scattering have been proposed to replace noble metals. By examining the carrier mobility, carrier concentration and interband losses, several oxides, nitride and semiconductors were demonstrated to have improved performance compared with the noble metals [17, 18, 33–35]. As summarized in Fig. 1.2, semiconductors Sb, Ge and III-V's are the most promising candidates, with carrier mobilities about 10 times higher than those of the noble metals.

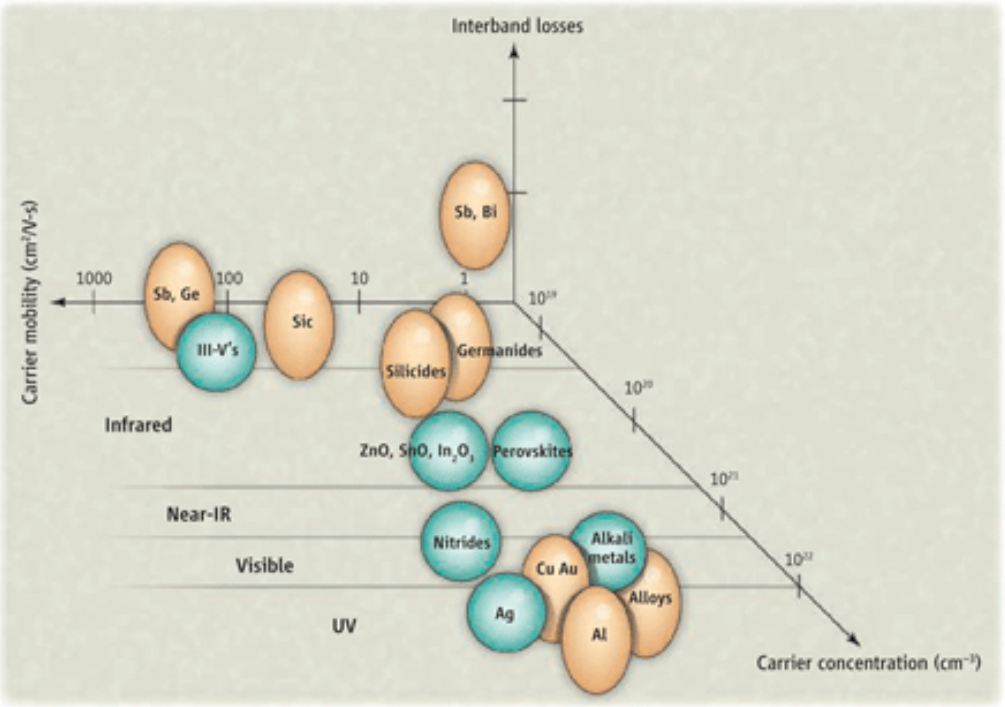

FIGURE 1.2: Carrier concentration, carrier mobility and interband losses of a variety of materials. (Reprinted from [18])

However, one should note that carrier mobility and carrier concentration are usually inversely related, which means that a material with a large carrier concentration usually has a low carrier mobility. This is because a large carrier concentration leads to an increased probability of electron−electron and electron−phonon

scattering, which in turn limits the carrier mobility. Therefore, there is no such a material with both high carrier mobility and large carrier concentration. It is worth stressing that even though materials, such as Sb and Ge, have much higher carrier mobilities compared with the noble metals, they still suffer from Ohmic losses due to the carrier scattering which happens on the order of 10∼100 femto-seconds [19, 20].

Recently, phonon polaritons are found to be another promising solution. Phonon polaritons describe the strong coupling of electromagnetic waves with the lattice oscillations of a polar crystal which has a non-zero polar moment. This mechanism does not suffer from Ohmic losses, because no scattering of the atoms or free electrons is involved [36]. Therefore, significantly stronger and narrower resonances can be achieved in polar crystals with the excitations of phonon polaritons [36]. However, most of the research so far deals with flakes or thin layers of such materials, and there are very few works focusing on user-defined polar crystal nanostructures. Investigations into nanoscale polar crystal resonators are highly necessary to see whether the effects manifested in plasmonic resonantors can be realized in this promising low-loss alternative.

1.3 Significance and Scope

As we discussed above, plasmonics is strongly limited by a fixed optical response. Moreover, it suffers from high losses at the same time. In this thesis, I report my research of tunable and low-loss nano-resonators for applications in the near and

mid-infrared. The main objective of this thesis is to investigate new materials and designs that can help ease the limitations mentioned above and possibly improve the performance of plasmonic/nanophotonic devices. The presented work consists of two parts, the first part deals with the tunability which is based on the phase-change materials, and the latter focuses on the low-loss materials that support phonon polaritons. Simple geometries, such as disks, pillars and bars are considered. In both parts of the research, theoretical and experimental studies are performed to provide a full picture of the proposed nanoscale designs.

In the first part of this thesis, to overcome the issue of lack of tunability, phase-change material $Ge_2Sb_2Te_5$ (GST) is hybridized with nano-resonators to achieve spectral tuning. GST is a widely used optical data storage medium and it is non-volatile at room temperature. The tuning of its phases and the associated optical properties have been well studied [37–41]. Here, it is used as a tunable dielectric environment to tune the optical response of nano-resonators. A gold nano-disk array on a thin layer of GST is used as the proof-of-concept. Significant spectral shifts of the resonances are achieved by changing the phase of GST. Further investigations are thus conducted to exploit the spectral tunability. Firstly, by hybridizing GST into a perfect absorber structure, a resonant peak with nearly 100% absorption is demonstrated to be tunable over a few hundred nanometers. Next, by tuning the resonances of an array of strongly coupled nano-resonators, spatial controls of the near-field hotspots are realized by changing the crystallization level of GST. Moreover, phase manipulations of the electromagnetic waves scattered from nano-slit cavities are further investigated. With the tunability

achieved by GST, a planar lens with configurable focal point is demonstrated. This part of my research proves the potential of phase-change material GST for tunable nanophotonics and plasmonics.

In the second part, through the collaborations with Dr. Caldwell's team at Naval Research Laboratory in Washington D.C. and Prof. Novoselov's group at University of Manchester, U.K., polar crystals which support phonon polaritons are investigated as a low-loss alternative to plasmonics. Due to the absence of free charge carriers, the losses of phonon polaritons are significantly reduced compared with surface plasmon polaritons. Since phonon polariton nano-resonators have rarely been studied, my attention is mainly focused on the resonance modes and their spectral behaviors as functions of the geometric parameters. Optical modes which are rarely observed in the conventional plasmonic structures are supported by phonon polariton resonators. For instance, monopolar modes, which are special longitudinal modes, are identified on SiC nano-pillar array. Compared with dipolar modes, monopolar modes are coupled to light with high quality-factors and can be easily positioned over a large frequency range by changing lattice size. Furthermore, hexagonal boron nitride (hBN), a van der Waals polar crystal, is investigated. Due to different in-plane and out-of-plane phonon polaritons associated with this material, hyperbolic optical modes are supported. A careful study of the modes reveals the distinct hyperbolic nature which is directional and volume-bounded. Quality factors of the modes observed in this part are found to be more than 50, with a few even in the range of 200. In contrast, the quality factor for a gold nano-resonator array is no more than 20,

and the value of a metal-based hyperbolic structure is ~ 4 [42, 43]. This work proves that phonon polaritons are a promising low-loss alternative to plasmonics, and it serves as a guideline for future nanophotonics designs in the mid-infrared region.

1.4 Organization of Thesis

Chapter 2 introduces the fundamental physics of surface polaritons. Started with the basics of surface plasmon polaritons supported at the interface between a metal and a dielectric, we extend the discussion to their analogue – surface phonon polaritons. Furthermore, the resonances of nanoscale resonators due to the excitation of localized surface polaritons are introduced. The relationship between resonant wavelength and dielectric constant of the environment, as well as quality factors that describe line widths of resonances are also covered.

Chapter 3 provides a brief introduction to simulation methods and experimental techniques used for sample preparation and characterization. Two computational methods and the basic configurations used in the simulations are covered in the first section. In the second section, sample preparation techniques from substrate cleaning to patterning are introduced. In the last section of this chapter, three optical characterization techniques are discussed.

In chapter 4, nano-resonators hybridized with phase-change material GST are

investigated in detail. This chapter discusses how GST can be used as a changeable dielectric environment to achieve tunability in geometrically fixed nano-resonators. Possible applications based on the tunable nano-resonators are demonstrated.

Chapter 5 deals with the challenge of Ohmic losses in the metals for nanophotonics. Phonon polaritons supported by polar crystals are proposed as an alternative to metal-based plasmonics. Silicon carbide nano-pillar arrays are investigated to illustrate the exotic optical modes supported by such nanoscale structures and the geometric dependence of near-field coupling. Furthermore, hexagonal boron nitride nano-cone arrays are also studied to reveal the unique optical responses associated with the material's hyperbolic nature. These low-loss alternatives provide a novel platform for mid-infrared applications.

Chapter 6 summarizes the results and contributions from my research, and proposes the future research directions for nanoscale resonators.

Chapter 2

Theoretical Background

2.1 Surface Polaritons

2.1.1 Polaritons

Polaritons are the quasiparticles which are used to describe the strong interaction between photons and electric or magnetic dipole-carrying excitations [44]. This process follows the level repulsion or anti-crossing principle, which means that two uncoupled dispersion curves form two different branches. The bandgap between the upper and lower branches changes in accordance with the coupling strength. An example is shown in Fig. 2.1. The upper branch above the light line marked in green asterisks represents the unbounded modes. The lower branch marked in red asterisks represents the bounded modes since it has a larger wave vector than the light, and essentially it can be used in applications [44, 45]. Two

kinds of polaritons, namely surface plasmon polariton (SPP) and surface phonon polariton (SPhP) will be discussed in the following sections.

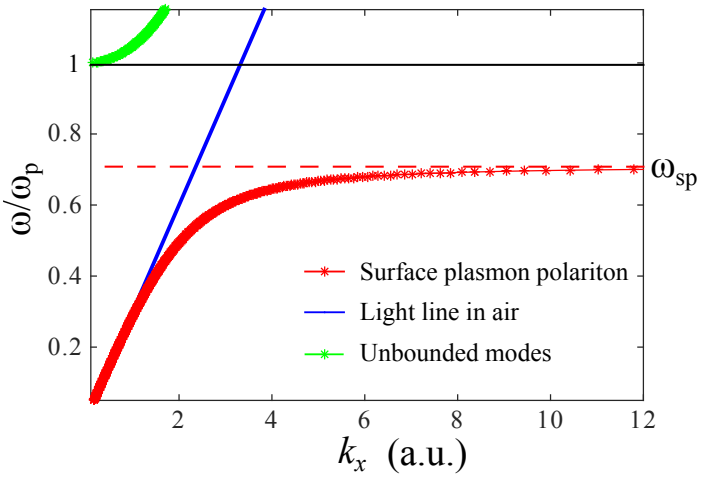

FIGURE 2.1: Dispersion relation of surface plasmon polariton. The metal considered is described by the Drude model. The bounded modes are marked in red asterisks and the unbounded modes are plotted in green asterisks. At very large wave vectors, the dispersion of surface plasmon polariton approaches the surface plasmon frequency (ω_{sp}) marked by the dash line.

2.1.2 Surface Plasmon Polaritons

SPP describes the strong interaction between light and free electrons. For a bulk of metal, the plasma frequency is defined as [44]

$$\omega_p = \sqrt{\frac{Ne^2}{\epsilon_0 m_e}}, \tag{2.1}$$

where N is the electron density, with e the electron charge, ϵ_0 the permittivity of free-space and m_e the effective mass of the electron. The Drude model can be used to estimate the permittivity of a metal, which can be expressed as

$$\epsilon(\omega) = 1 - \frac{\omega_p^2}{\omega^2 + i\omega\gamma}, \tag{2.2}$$

with ω_p denoting the plasma frequency and γ the damping constant of the metal. At visible and infrared frequencies, $\gamma \ll \omega_p$ and the dielectric constant can be further simplified as

$$\epsilon(\omega) = 1 - \frac{\omega_p^2}{\omega^2}, \tag{2.3}$$

Eq. 2.3 explains why metals look glossy. If light with frequency ω below ω_p is incident on the metal, $\epsilon(\omega) < 0$ and the incident light is reflected. Otherwise if $\omega > \omega_p$, $\epsilon(\omega) > 0$ and the metal is not metallic anymore at these frequencies.

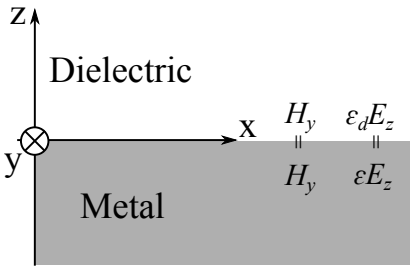

FIGURE 2.2: Schematic diagram of an interface between metal and dielectric. For TM waves, across the interface of the two media, H_y is continuous and $\epsilon_d E_z = \epsilon E_z$.

Considering the dielectric-metal interface shown in Fig. 2.2, by solving the Maxwell's equations of TM waves with the conditions that H_y is continuous across the interface as well as $\epsilon_d E_z = \epsilon E_z$, the dispersion relation of the surface modes supported can be expressed as [44, 46]

$$k_x = k_0\sqrt{\frac{\epsilon\epsilon_d}{\epsilon+\epsilon_d}}, \tag{2.4}$$

Combining Eqs. 2.4 and 2.2, the dispersion relation can be plotted as Fig. 2.1. The dielectric considered is air ($\epsilon_d = 1$). At small k_x, SPP is close to the light line plotted in blue color. At large k_x, SPP approaches the dashed line which corresponds to the frequency that the denominator in Eq. 2.4 is equal to zero. This frequency ω_{SP}, named as surface plasma frequency, is calculated as [44]

$$\omega_{SP} = \frac{\omega_p}{\sqrt{1+\epsilon_d}}, \tag{2.5}$$

.

Since SPP always has a larger k_x compared with the light in the considered dielectric, the wave vectors of SPP in the other directions have to be imaginary. Considering the 2D case of SPP propagating along x-axis, an imaginary k_z suggests that $e^{ik_z|z|}$ exponentially decays as $|z|$ increases, meaning no EM waves are propagating in $\pm z$-directions. At z that $e^{ik_z|z|}$ drops to e^{-1}, one can retrieve the value of skin depth, which is the quantity showing how far a field extends into a medium. The skin depth δ is expressed as

$$\delta = \frac{c}{\omega}\mathrm{Im}(\sqrt{\frac{\epsilon+\epsilon_d}{\epsilon_x^2}}), \tag{2.6}$$

.

where $\epsilon_x = \epsilon$ if the skin depth is calculated in metal, or $\epsilon_x = \epsilon_d$ if it is calculated for the dielectrics. At small wave vectors, the skin depth inside the metal is very small and the speed of SPP is close to the light speed. In contrast, at large wave vectors with ω close to ω_{SP}, the speed of SPP approaches zero, and a large portion of the field is inside metal.

2.1.3 Optical Phonon Polaritons

Phonon polaritons describe the strong coupling of photons with optical phonons. Phonons are the vibrational modes of atoms in crystals. Crystals with two or more than two different atoms in a primitive support vibrational modes that can be excited optically, known as optical phonons [47]. There are two types of optical phonon, a longitudinal optical phonon (LO) and a transverse optical phonon (TO). As illustrated in Fig. 2.3, LO represents the displacement of the atoms parallel to the wave vector while TO corresponds the displacement of the atom perpendicular to the wave vector. In both cases, the neighboring atoms are moving in the opposite directions.

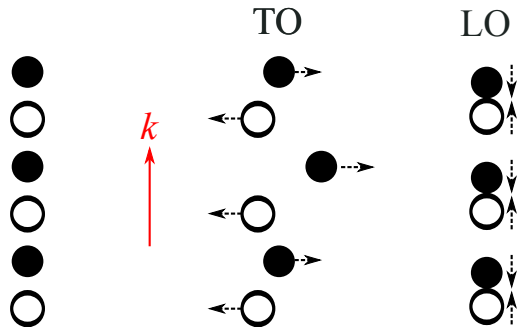

FIGURE 2.3: Schematic drawings of transverse and longitudinal optical phonons

For polar crystals, such as SiC [36, 47–49] and GaAs [50, 51], the splitting of TO and LO results in a frequency window with negative real part of permittivity ($\mathrm{Re}(\epsilon) < 0$), which is termed as Reststrahlen band [20, 52]. The permittivity of such polar crystals is modeled as

$$\epsilon = \epsilon_\infty (1 + \frac{\omega_{LO}^2 - \omega_{TO}^2}{\omega_{TO}^2 - \omega - i\gamma\omega}), \tag{2.7}$$

.

where ϵ_∞ is the high frequency dielectric constant and γ represents the phonon damping. Due to the absence of free charge carriers, the scattering of the optical phonons is on a timescale of picoseconds. Whereas for metals, the scattering of free electrons is under a hundred femtoseconds. The relatively long optical phonon lifetime results in exceptionally small values of the imaginary part of the permittivity. 4H-SiC is chozen for the illustration, with $\omega_{LO} = 970cm^{-1}$, $\omega_{TO} = 797cm^{-1}$, $\epsilon_\infty = 6.56$, and $\gamma = 1.3$ [49]. The real and imaginary parts of the permittivity of SiC ($\mathrm{Re}(\epsilon)$ and $\mathrm{Im}(\epsilon)$) are plotted in Fig. 2.4

Because of $\mathrm{Re}(\epsilon) < 0$ within the Reststrahlen band, SiC behaves like metals that reflects the incident light. The energies of TO and LO relative to this high-reflectivity Reststrahlen band is shown in Fig. 2.5. Raman shifts spectrum reveals the peaks due to TO and LO, and the Reststrahlen band identified from the reflection spectrum of a SiC flake is bounded by the TO and LO phonons.

The light-phonon interactions at the surface of a medium are termed as surface phonon polaritons (SPhP). An analogy can be established between SPhP and

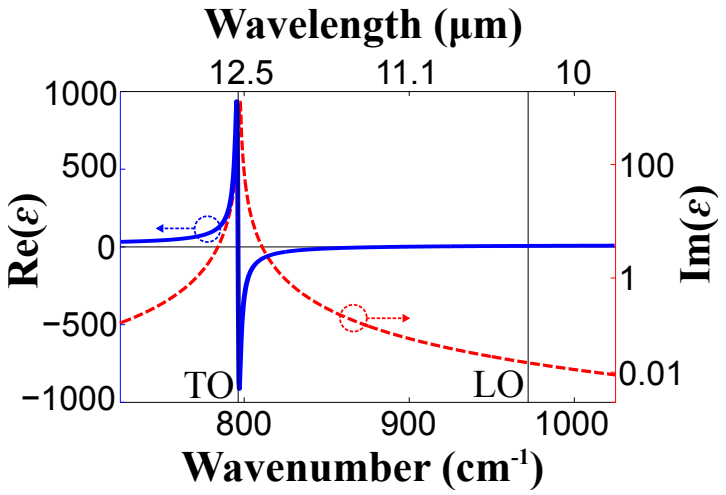

FIGURE 2.4: Permittivity of 4H-SiC around its Reststrahlen band [53]. The blue line denotes the real part and the red line (in log scale) represents the imaginary part of the permittivity. The thin vertical line marks the positions of TO ($797cm^{-1}$) and LO ($970cm^{-1}$) (Reprinted from [53]).

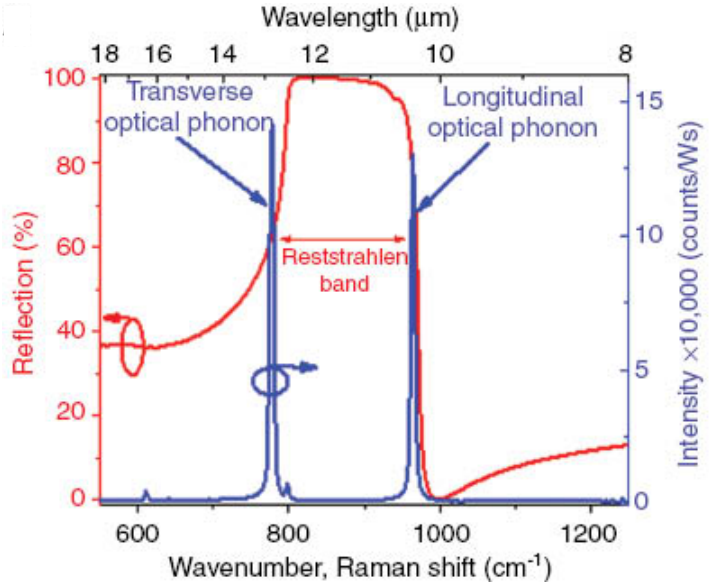

FIGURE 2.5: Reflection Spectrum (red line) and Raman Shift (blue line) of a 4H-SiC flake. The Raman shift peaks corresponding to TO and LO phonons are clearly shown, and the Reststrahlen band with high reflectivity is bounded by the two phonon peaks. Reprinted from [20]

SPP. Considering the same interface shown in Fig.2.2 with Eq. 2.4 valid for TM waves, assigning the dielectric constant of SiC to ϵ, the dispersion relation of the bounded modes supported at SiC-air interface is shown by the red solid line in Fig. 2.6. Similar to SPP, SPhP starts to deviate from the light line as the wave vectors k increases. At large wave vectors, phonon polaritons approach the frequency similar to ω_{SP} at which $\mathrm{Re}(\epsilon + \epsilon_d) = 0$. This frequency corresponds to the situation that k_x becomes infinitely large. Compared with Fig. 2.1, an additional curve plotted in black color below the frequency ω_{TO} can be seen in Fig. 2.6. This curve shows the dispersion relation of SiC as a normal dielectric medium outside the Reststrahlen band.

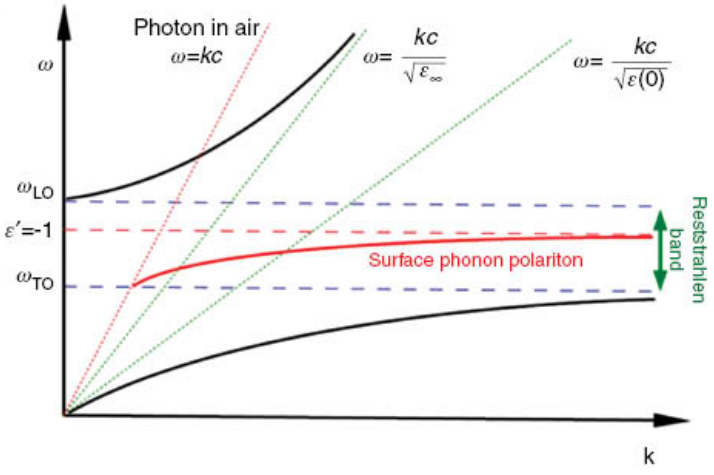

FIGURE 2.6: Dispersion relation of 4H-SiC. The red solid line represents the bounded modes that are supported on the surface of SiC. Note that outside the Reststrahlen band, SiC and polar crystals in general are dielectric materials which are transparent. Reprinted from [20]

Polar crystals possess negative permittivity due to the vibrations of the atoms, while metals possess negative permittivity due to free electrons oscillations. Although the causes are different, the optical responses from materials of negative permittivities are essentially the same. However, optical phonons polaritons are

free of Ohmic losses as a result of the absence of free charge carriers. This property provides a new route to realize nanophotonic devices of lower loss compared with SPP. The advantages include large field enhancement and high Q-factors [36, 48].

2.2 Localized Surface Polaritons: Resonances of Nano-particles

In the previous sections, the discussions were based on a flat interface between dielectric and a metallic substrate. The fields of either SPP or SPhP were confined close to the interface. If the metallic substrate shrinks to a nanoscale particle, the polaritons (SPP and SPhP) are further restricted in the propagation directions. Localized surface polaritons (LSP) are used to describe such situations [54, 55].

LSP has several attractive properties, for example, sub-diffractional confinement of light and large electric field enhancements [56–58]. The possible applications based on these properties include surface-enhanced Raman spectroscopy (SERS) and surface-enhanced infrared absorption spectroscopy (SEIRA). Furthermore, the resonant frequency of LSP is highly dependent on the surrounding medium, spectral tuning of a geometrically fixed metallic nanostructure is therefore feasible by changing the dielectric constant of the environment. In the following sections, LSP resonances (LSPR) supported by nano-particles will be discussed in detail.

2.2.1 Spectrum of LSPR

Considering a sub-wavelength sphere with diameter $d \ll \lambda$ under the illumination of an incident light with wavelength λ, the phase of the oscillating electromagnetic field can be regarded as constant across the entire sphere. Therefore, the oscillating field can be simplified as an electrostatic field. With free electrons driven by the external electric field E_0, the sphere is polarized and the dipole moment p as a result of the polarization can be described as

$$p = \epsilon_0 \epsilon_d \alpha_p E_0, \tag{2.8}$$

The polarizability α_p, which is the ratio between the dipole moment and the amplitude of the incident field, can be expressed as [59]

$$\alpha_p = 4\pi (\frac{d}{2})^3 \frac{\epsilon - \epsilon_d}{\epsilon + 2\epsilon_d}, \tag{2.9}$$

where ϵ is the permittivity of the metallic sphere and ϵ_d is the permittivity of the environment. To maximize α_p, $\epsilon = -2\epsilon_d$ is required. The frequency-dependent ϵ of a metal can be estimated by the Drude model as described in Eq. 2.2. Combined with the condition $\epsilon = -2\epsilon_d$, the frequency at which the maximum α_p is achieved can be written as [60]

$$\omega_{max} = \frac{\omega_p}{\sqrt{2\epsilon_d + 1}}, \tag{2.10}$$

Converting the frequency to wavelength and permittivity to refractive index, the above equation can be re-written as [60]

$$\lambda_{max} = \lambda_p \sqrt{2n_d^2 + 1}, \tag{2.11}$$

where $\lambda_p = 2\pi c/\omega_p$ and $n_d = \sqrt{\epsilon_d}$. Based on this equation (Eq. 2.11), it can be concluded that for a sub-wavelength metallic sphere of a given material, the spectral position of LSPR can be tuned by varying the environment refractive index n_d. Because the difference between $\sqrt{2n_d^2 + 1}$ and $\sqrt{2}n_d$ is less than 5% when $n_d > 2.2$, Eq. 2.11 can be further simplified as

$$\lambda_{max} \sim \sqrt{2}\lambda_p n_d, \tag{2.12}$$

The discussion above is based on the precondition that the sphere is much smaller than the incident wavelength. For larger sizes, the structures support strong scattering modes which vary with the geometry. For example, a nano-bar with length L is illuminated by an incident light with electric field polarized along the nano-bar. The nano-bar can be regarded as a Fabry-Pérot (FP) cavity. The resonances are expected to take place when $\sin(2\pi L/\lambda_{eff}) = 0$, where λ_{eff} is the wavelength of the modes excited on the surface of the nano-bar. As a rough estimation, λ_{eff} can be considered as $\lambda_{eff} = m_1 + m_2 \frac{\lambda_0}{n_d \lambda_p}$, where m_1 and m_2 are the parameters determined by the permittivity and the geometry of the structure, λ_0 is the wavelength in vacuum. The relation between the refractive

index of the environment (n_d) and the FP resonances can be further estimated as

$$\lambda_{max} = ((\frac{2L}{n} - m_1)\frac{\lambda_p}{m_2})n_d, \tag{2.13}$$

where $n = 1, 2, 3...$ denotes the order of the mode. If the geometry and the material of the nano-bar are fixed, L, m_1, m_2, and λ_p can be regarded as constants for simplicity, therefore λ_{max} is in proportion to n_d.

Both Eqs. 2.12 and 2.13 state that the resonance supported by a nano-particle can be shifted by changing n_d, and the relation between λ_{max} and n_d is approximately linear. These two equations provide the theoretical basis of spectrally tuning a LSPR by changing the optical properties of the environment. In Chapter 4, detailed discussions about resonance tuning via phase-change materials and the related applications will be covered.

2.2.2 Quality of a Resonator

To evaluate the performance of a nanoscale resonator, quality factor (Q-factor) is usually used as the gauge for comparison. Q-factor is defined as the ratio between the bandwidth of a resonance and the central frequency,

$$Q = \frac{\omega_{res}}{\Delta\omega_{res}}, \tag{2.14}$$

where ω_{res} is the resonant frequency and $\Delta\omega_{res}$ quantifies the full width at half maximum (FWHM) of the resonance. It is dimensionless, therefore, it can be used to compare the resonances across different frequency regions.

FWHM of a resonance sometimes can be tricky to retrieve directly. The following two steps are used to calculate the FWHM in such cases. Firstly, the line shape of the resonance is fitted by a Gaussian distribution, which can be expressed as

$$f(x) = A\exp(-\frac{(x-B)^2}{2C^2}), \tag{2.15}$$

with parameters A, B and C to be varied. The maximum value of $f(x)$ is A. By solving the equation $f(x) = A/2$, x is found to be $B \pm \sqrt{2\ln 2}C$. Therefore, the full width at half maximum of the resonance is calculated as $FWHM = 2\sqrt{2\ln 2}C$.

Q-factor reflects the losses associated with resonators. A higher Q-factor corresponds to a resonator with less losses and a sharper peak in the spectrum. In order to realize low-loss nano-resonators (high Q-factor), one approach is to employ low-loss materials. In particular, polar crystals have much smaller Ohmic losses compared with metals, thanks to the absence of free charge carriers. An example is shown in Fig. 2.7, in which a SiC sphere demonstrates a stronger and sharper resonance than its counterparts (Au and Ag). Detailed discussions about polar crystals SiC and hexagonal BN will be covered in Chapter 5.

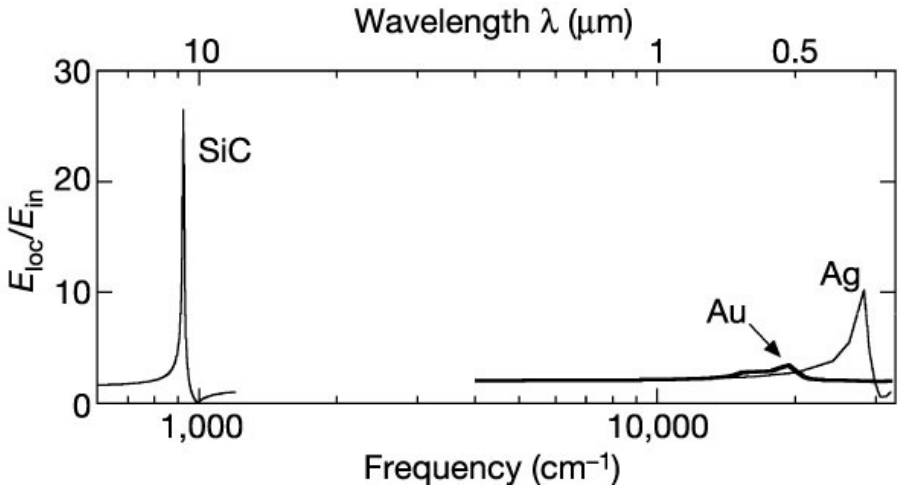

FIGURE 2.7: Field enhancement of LSPhP from a SiC sphere compared with LSPP from spheres of noble metals (Au and Ag). The diameter of the spheres is 10 nm for all the cases. The resonance is due to Fröhlich condition that $\epsilon = -2$ (reprinted from [36]).

Chapter 3

Methods

3.1 Numerical Simulations

Nano-resonators in simple geometries, such as spheres, can be modeled analytically by using Mie theory. For more complicated geometries, numerical simulations are the most efficient way to predict and understand the optical response. Two computational methods are widely used, namely Finite-Difference Time-Domain (FDTD) and Finite Element Method (FEM). In this thesis, commercial packages Lumerical FDTD Solutions using the FDTD algorithm and COMSOL Multiphysics using FEM are employed.

3.1.1 Finite-Difference Time-Domain

FDTD runs in the time domain. An electromagnetic pulse that contains the frequency range of interest is launched from a source. The electromagnetic pulse

propagates and interacts with the structures in the FDTD simulation region defined by the users. The FDTD simulation region is divided into small cuboids or rectangles (known as meshes) in 3D and 2D simulations, respectively. Finer meshes offer a more precise interpretation of the designed geometries, but require more time and computing resources. Monitors are placed in the locations of interest and they record the fields as a function of time. Results in frequency domain are further calculated via Fourier transforms.

Two situations are often considered in FDTD simulations, one is to calculate the optical response from a periodic structure, and the other is to study the properties of an isolated structure. For the former case, the configuration is illustrated in Fig. 3.1 a. A unit cell of the structure is enclosed by the simulation region. The top and bottom boundaries are set to be perfectly matched layers (PMLs) to prevent any reflections from these two boundaries. The boundaries on the sides are set to be periodic for normal incidence or bloch boundary conditions when plane waves are injected at an angle. Above the plane wave source, Monitor 1 is used to collect the reflected light from the structure. Monitor 2 below the structure is used to collect the transmitted light. For the situation that an isolated structure is simulated, the configuration is shown in Fig. 3.1 b. All the boundaries of the simulation region are set to be PMLs to prevent any reflections. Plane waves are launched towards the structure within the box defined by the total-field scattered field source (TFSF). TFSF divides the simulation region into two – inside the TFSF box, both incident field and scattered field exist; outside the box, only scattered field exists. The inner monitor records the difference

between the power of light that enters the monitor box and the power of light exits the box. This net power is further normalized by the incident power to retrieve the absorption cross section. The TFSF source is enclosed by an outer monitor, which records the scattered fields from the structure. The sum of the absorption and scattering cross sections represents the overall interaction strength of the structure with light, which is termed as extinction cross-section.

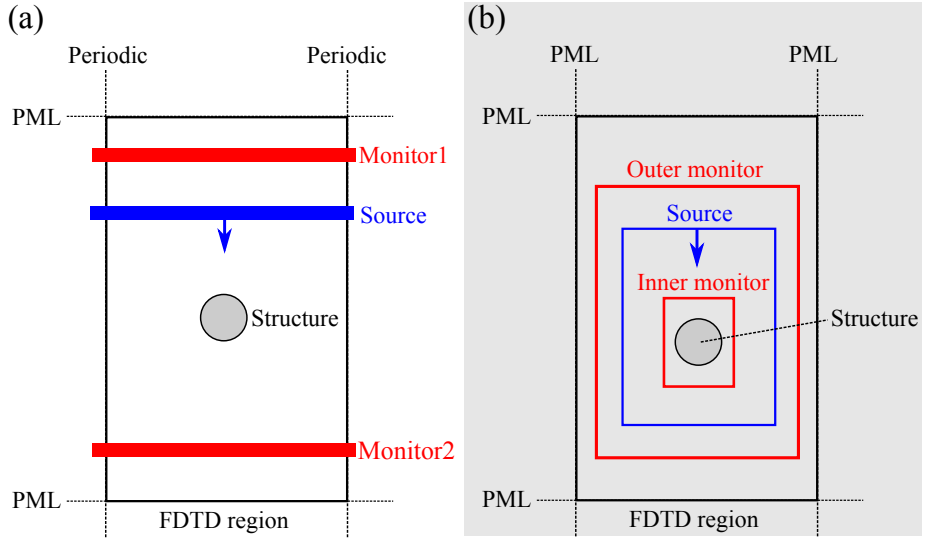

FIGURE 3.1: (a) Schematic of the FDTD configuration to simulate periodic structures. The top and bottom boundaries of the simulation region are set to be PMLs to prevent any reflections from these two boundaries. The boundaries on the sides are set to be periodic. Plane waves are injected towards the structure. Above the plane wave source, Monitor 1 is used to collect the reflected light from the structure. Monitor 2 below the structure is used to collect the transmitted light. (b) Schematic of the configuration of FDTD to simulate an isolated structure. All the boundaries of the simulation region are set to be PMLs to prevent any reflections. Plane waves are launched towards the structure within the box defined by the total-field scattered field source. The data recorded by the inner monitor is used to calculate the absorption cross-sections and the data from the outer monitor is used to retrieve the scattering cross-sections.

FDTD has several advantages. It calculates a spectrum in a single run, which means no iteration is needed for each frequency point. Since it runs in time

domain, non-linear responses, such as the second and third harmonic generation, can be simulated easily.

The disadvantages of FDTD usually appear when grazing angle excitations are needed, or the optical properties of the materials are too dispersive. For a broad-band source in FDTD, the actual incident angle varies with frequency if the injection angle is not set as zero. As for a material's optical property, a continuous function is required to describe the refractive index or the permittivity.

3.1.2 Finite Element Method

FEM is a popular alternative to FDTD method. Instead of injecting a pulse, FEM injects steady-state electromagnetic (EM) waves defined in the frequency domain. As a result, each frequency point needs to be computed separately in order to construct a spectrum. Apart from this drawback, COMSOL offers a few advantages over Lumerical FDTD. First of all, since each frequency is calculated separately, no fitting to the material's optical property is needed. Without the errors in fitting, results are more accurate. Secondly, meshing in COMSOL is very flexible. In addition to cuboids and rectangles, tetrahedrons and triangles can be used to mesh a volume and a surface, respectively. Geometries can be resolved more accurately without increasing the total number of meshes. Moreover, injection angle can be well defined in COMSOL and it does not suffer from the frequency-dependent variations as discussed in FDTD section.

In COMSOL, the configuration used for calculating the optical responses from a periodic structure is similar to the FDTD configuration as shown in Fig. 3.1 a.

Periodic boundary conditions are set to the boundaries on the sides. Instead of defining a source and a monitor, two ports are assigned to the top and bottom boundaries, with excitation turned on for port 1. No monitors are needed because COMSOL saves all the results automatically at every mesh. After running the simulation, transmission and reflection are calculated as $|S21|^2$ and $|S11|^2$. SXY means the response at port X due to port Y.

To calculate the scattering and absorption from an isolated structure, the configurations illustrated in Fig. 3.2 are used. The calculations consist of two steps. In the first step (Fig. 3.2 a), an empty region is simulated to retrieve the EM field of the plane wave. This EM field is used in step 2 as background field, and the program is set to calculate the scattered field only. The power absorbed is calculated by integrating the total power dissipation density across the structure, and the scattered power is calculated by integrating the average power flow normal to the surface of the structure.

3.2 Sample Preparations

Nano-fabrication techniques are used to prepare the samples. In order to ensure the quality, each step from substrate cleaning to patterning is crucial. In this section, the techniques I used for sample preparation will be discussed.

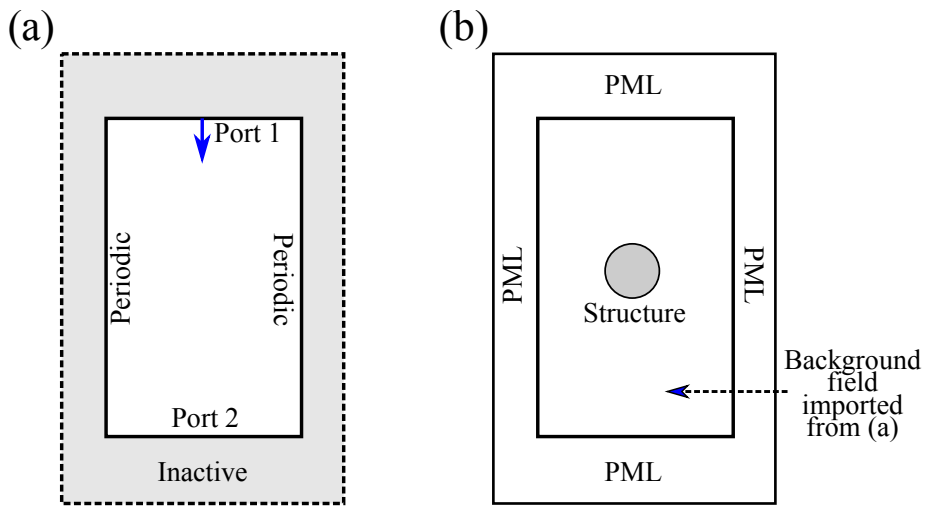

FIGURE 3.2: Schematics of the 2-step configuration of FEM to simulate an isolated structure. (a) Calculation of the plane wave in an empty region. (b) With the background field imported from step (a), scattered field is solved with the structure and PMLs enabled.

3.2.1 Substrate Cleaning

Substrates (glass, quartz, and silicon) need to be cleaned first because they may be contaminated by dust, oil, etc. Such contamination greatly compromises the flatness of the substrate surfaces and severely affects the quality of final structures. To clean the substrates, ultrasonic bath is employed. An ultrasonic bath is a water tank with a transducer that produces high-power ultrasonic waves oscillating in the tank. The intense physical vibration assists solvent to dissolve the soluble contamination and detaches the insoluble particles. The recipe for substrate cleaning is summarized in Table 3.1. After the last step of ultrasonic bath, the substrates are dried by nitrogen gas.

TABLE 3.1: Ultrasonic cleaning recipe

Solvent	Ultrasonic time
Acetone	30 minutes
Isopropyl alcohol	30 minutes
Deionized water	15 minutes

3.2.2 Photoresist Coating

In order to define patterns by light, chemicals that can vary their solubility based on the degree of exposure to light are needed. These chemicals are named photoresist. Because the sizes of the resonators are designed to be in the nanoscale, the thickness of photoresist is required to be thin (usually less than 500 nm) and uniform. Spin-coating is used to fulfill the task. It utilizes a centrifugal force to spread the liquid photoresist uniformly over an area on the substrate surface and the thickness of photoresist is controlled by the spin speed. Two-step spin-coating is usually used: slowly spinning (e.g. 500 rpm) for a few seconds in the beginning, then ramping upwards to the spin speed for the desired thickness (e.g. 4000 rpm for photoresist S1805 to be 500 nm thick). Soft baking at 75° for 1 minute is usually employed after spin-coating to evaporate the residual solvent, which improves the quality of lithography.

3.2.3 Thin Film Deposition

Thin film deposition is done by using either an evaporator or a sputtering machine. To ensure the purity of the films, vacuum is always needed to reduce the number of impurities during the deposition process. A schematic of electron-beam (e-beam) evaporator is shown in Fig. 3.3. At the bottom of the vacuum

chamber, electrons emitted from a filament are focused on target materials. The kinetic energy from the electrons is transferred into thermal energy, raising the temperature and eventually vaporizing target materials. At the top of the chamber, substrates are attached to a rotation stage to ensure the uniformity. This technique is used to deposit metals and dielectrics, such as gold and SiO_2. The system used is a BOC Edwards EB03 e-beam evaporator.

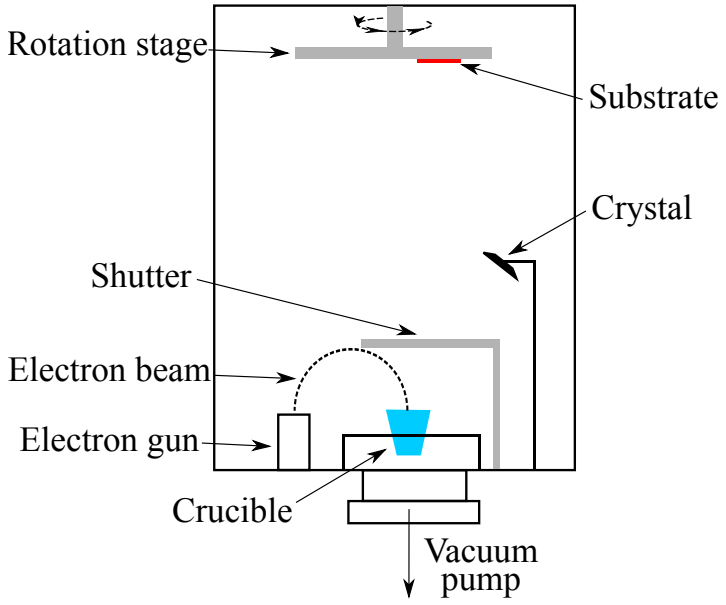

FIGURE 3.3: Schematic of electron beam evaporator based on BOC Edwards EB03 with the basic components highlighted.

A sputtering system, as illustrated in Fig. 3.4, uses ions in the plasma to bombard the target material directly. The kinetic energies from the ions in the plasma transfer to the atoms or molecules of the target, detaching the atoms/molecules from the target. The atoms/molecules from the target travel across the chamber and deposit on the substrates. This technique is used to deposit phase-change material $Ge_2Sb_2Te_5$, and the piece of equipment is a Balzers CUBE sputtering system.

Comparing the two techniques (e-beam evaporation and sputtering), they have their advantages and disadvantages. For the e-beam evaporation, the pressure during the evaporation is controlled below 8×10^{-6} Torr by adjusting the deposition rate. Although the sputtering system has a similar base pressure as the e-beam evaporator ($\sim 2 \times 10^{-6}$ Torr), the working pressure is usually above 1×10^{-3} Torr because gases are directed into the chamber to generate plasma. The lower working pressure of the e-beam evaporator ensures a better quality of the deposited film. However, the principle of the e-beam evaporator requires the target materials to be melt, which means that high temperature is involved in this step. Materials, such as $Ge_2Sb_2Te_5$, organic molecules and plastic substrates which change properties at high temperature, are not suitable for this process. Instead, sputtering offers a deposition process below the melting temperature, which is suitable for the temperature-sensitive materials and substrates.

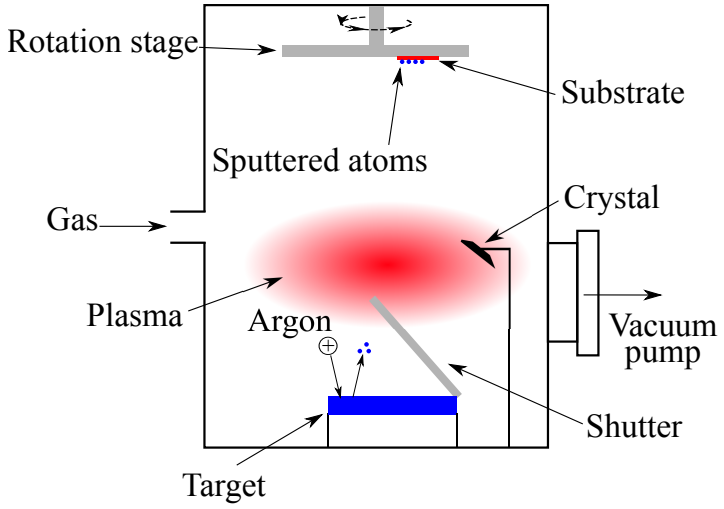

FIGURE 3.4: Schematic of sputtering evaporator with the basic components of the system illustrated.

3.2.4 Laser Interference Lithography

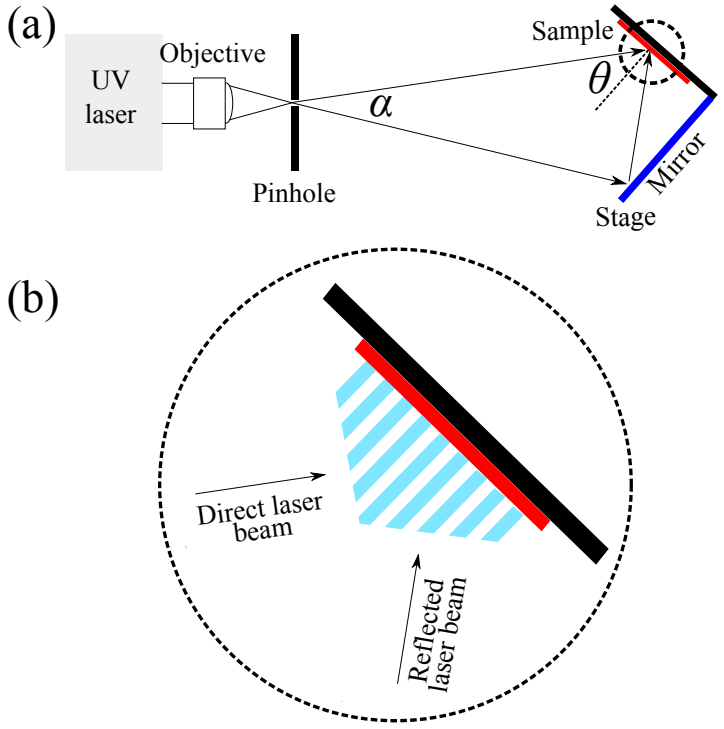

FIGURE 3.5: (a) Schematic of a laser-interference lithography setup. (b) The direct laser beam interferences with the reflected laser beam on the sample surface, forming a stable intensity distribution with the alternating maximum and minimum.

Laser-interference lithography (LIL) is a simple and fast method to generate simple periodic structures. It uses the interference patterns of two coherent laser beams to expose photoresist [61]. A LIL setup employing Lloyd's mirror is shown in Fig. 3.5 a. A Helium-Cadmium (He-Cd) laser is used to generate a continuous laser beam at the wavelength of 325 nm with an average output power of 40 mW. This laser beam is focused slightly before a pinhole to achieve a clean coherent circular wavefront. The stage is placed far from the pinhole which is about 1.2 m, so that the whole substrate (25 mm by 25 mm) can be covered by the zero order of the diffraction pattern. The laser beam incident on the sample directly

from the laser and the laser beam reflected from the mirror result in a stable periodic maximum and minimum intensity distribution, as shown in Fig. 3.5 b. The period P of the interference pattern can be approximately calculated as [61, 62]

$$P = \frac{\lambda}{2 \sin \theta} , \tag{3.1}$$

where λ is the wavelength of the laser and θ denotes the angle marked in Fig. 3.5a. Note that an assumption is made that $\alpha \sim 0°$.

Although the interference patterns generated by this setup are limited to 1D grating, more complex structures can be fabricated by two or multi-step exposure. The cartoons in Fig. 3.6 illustrate the steps to fabricate a 2D dot array. Firstly, a 1D grating is patterned by LIL. Then the sample is rotated by a certain angle, and it is exposed for the 2nd time. Depending on the type of photoresist and the subsequent step whether it is an etch-down or lift-off, fish-net structures or dot arrays can be fabricated. In the example shown, positive photoresist is used, and the sample is rotated by 90° between the two exposures. Therefore, 2D dot array in square lattice are formed.

Photos of the samples fabricated by the 2-step LIL described above are shown in Fig. 3.7 a. The substrates are 1×1 inch quartz substrates. A SEM image of the the sample illustrating the 2D dot array is shown in Fig. 3.7 b. The dot array is uniform and the square lattice is well-defined.

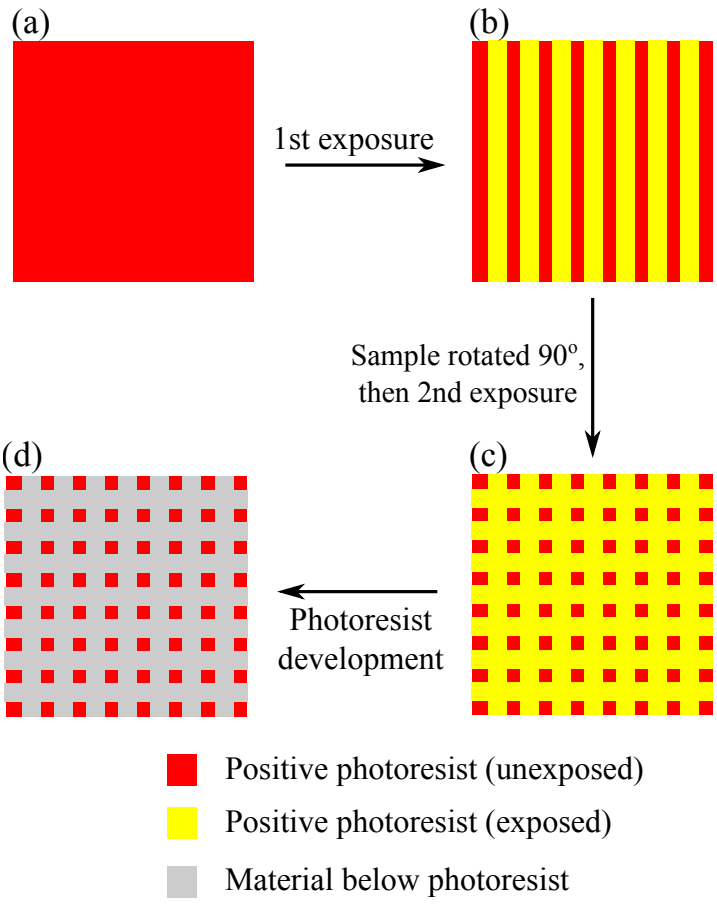

FIGURE 3.6: Schematic drawings of 2-step laser-interference lithography to form dots array. (a) The photoresist-coated substrate. (b) The patterns of the exposed photoresist after the 1st round of exposure on the LIL setup. (c) The patterns of the exposed photoresist after the 2nd round of exposure on the LIL setup. Before the 2nd round, the sample is rotated by 90°. (d) The residual photoresist after the development.

3.2.5 Ion Milling

Ion milling is a dry etching method, with a working principle similar to sputtering. As shown in Fig. 3.8, instead of bombarding a target by plasma, samples after the lithography are struck by the ions of high kinetic energy. The unprotected regions on the samples are etched away, forming the designed structures protected by the mask. The stage is usually tilted downward by an angle $\theta \sim 10°$

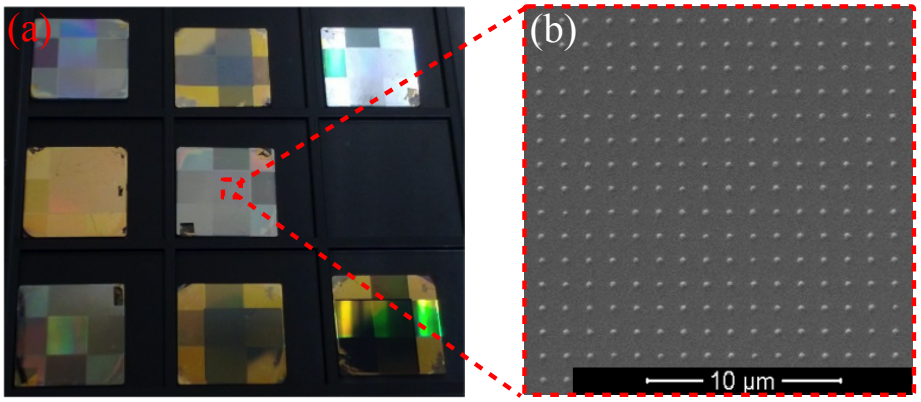

FIGURE 3.7: (a) A photograph of the samples fabricated by laser-interference lithography taken by a camera. The samples were exposed to UV light twice. Before the 2nd exposure, the sample was rotated by 90°. (b) A SEM image of the 2D dot array fabricated by laser-interference lithography.

to reduce the possibility of re-deposition. The ion milling system used is from Vecco.

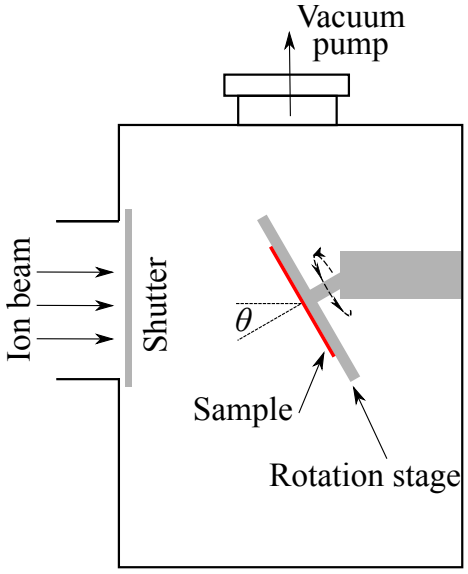

FIGURE 3.8: Schematic drawing of an ion-milling system based on Vecco NEXUS IBE-350Si (http://www.veeco.com/products/ion-beam/etch/nexus-350si.aspx). Ar plasma removes the materials on the sample by striking the atoms away from the sample surface.

3.3 Sample Characterization

Several optical characterization techniques are used to investigate the responses from the nano-resonators. To retrieve the spectral information, UV-Vis-NIR spectroscope (Shimadzu UV-3600) and Fourier-Transform Infrared (FTIR) Spectroscope (Bruker Vertex 70, with Bruker Hyperion 2000 microscope) are used. To spatially map electromagnetic field distributions, confocal microscope (Nanonics scanning confocal microscope) is used. The detailed information of each technique is provided in the following sub-sections.

3.3.1 UV-Vis-NIR Spectroscopy

The basic idea of a spectroscopy is shown in Fig. 3.9. A light source emits light in a range of frequencies. A monochromator, which is usually a prism or gratings, selects one frequency at a time and passes the single-color light to the sample. Depending on the configuration, either the transmitted (Fig. 3.9 a) or reflected (Fig. 3.9 b) light from the sample is collected by the detector. This raw data is then normalized to the corresponding reference data of a bare substrate, air or mirror to obtain the transmission or reflection spectrum of the patterned structures.

The UV-Vis-NIR spectroscope is Shimadzu UV-3600. Three detectors are used to cover the wavelength range from 185 nm to 3300 nm, namely a photomultiplier tube (PMT) covering UV and visible regions, InGaAs and cooled PbS detectors

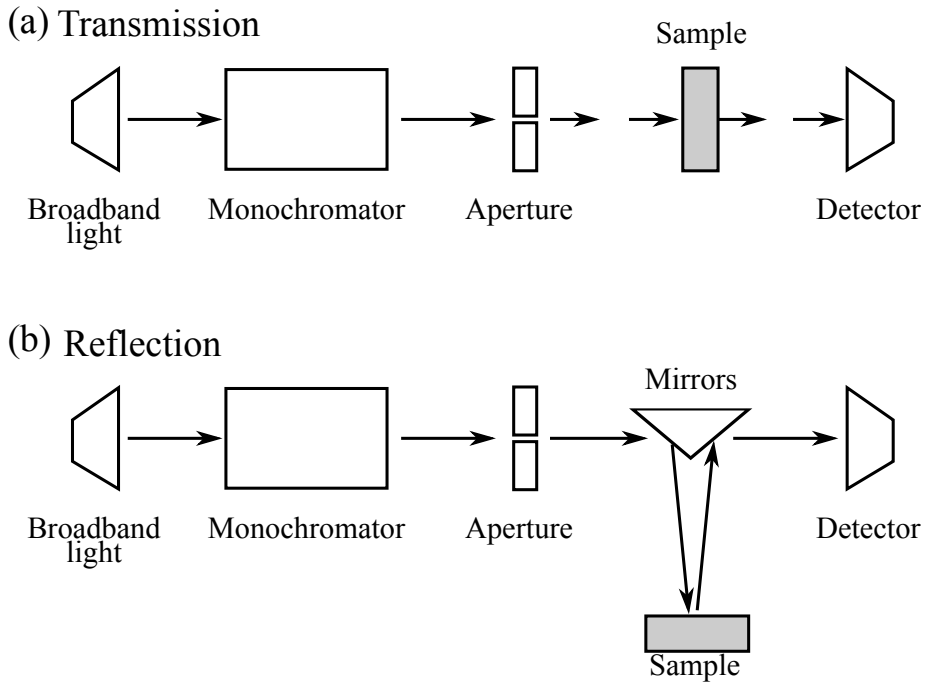

FIGURE 3.9: Schematic diagrams of a spectrophotometer for (a) transmission measurement and (b) reflection measurement based on Shimadzu UV-3600. A broadband light source emits light into a monochromator, which is usually a prism or gratings that select a single color. This single-frequency light is directed to the sample and the reflected or transmitted light is collected by the detector. (http://www.shimadzu.com/an/spectro/uv/uv-3600plus.html)

covering the shorter and longer wavelengths in the near-infrared regions, respectively. It has two light sources, one for UV and visible regions and the other for NIR. This machine is suitable for samples of large patterned area (the diameter of light beam is $\sim$ 2mm) and has an optical response below 3000 nm.

3.3.2 Fourier-Transform Infrared Spectroscopy

Fourier-Transform Infrared Spectroscopy (FTIR) is another method to measure the transmission and reflection of a sample. Instead of probing the sample with monochromatic light in the frequency domain, FTIR measurements are performed in the time domain. The light containing a wide range of wavelengths

from the broadband source is temporally modulated by an interferometer as shown in Fig. 3.10 a. The interferometer consists of a beamsplitter, a fixed mirror and a moving mirror. The beamsplitter splits the light into two. The reflected light from the fixed mirror and the moving mirror with a speed p result in a temporally modulated signal due to interference. The modulated signal is named as interferogram, and it can be expressed as

$$S(x) = S_0(\bar{v}) \cos(2\pi \bar{v} x)\,, \tag{3.2}$$

where $x = pt$ is the displacement of the moving mirror at time t and $S_0(\bar{v})$ denotes the source profile as a function of the wavenumber $\bar{v}$. If $S_0(\bar{v})$ has a Gaussian profile as $S_0(\bar{v}) = \exp(-\frac{(\bar{v}-4000)^2}{5\times10^6})$ with $500\,\mathrm{cm}^{-1} < \bar{v} < 5000\,\mathrm{cm}^{-1}$, the interferogram as a result of the Eq. 3.2 is shown in Fig. 3.10 b.

This time-variant EM wave is then directed onto the sample. By performing Fourier transform on the detected signal, spectrum containing the information of the whole system (source, mirrors, beamsplitters, absorption in the air, etc) is retrieved. Normalization as the last step gets rid of the unwanted information of the system.

The FTIR system is Bruker Vertex 70. The schematic of the system is shown in Fig. 3.11. A spectral range from $\sim$0.6 µm to $\sim$20 µm can be covered with the two sources (one for NIR, the other for MIR), the three detectors (Si diode for visible region, InGaAs detector for NIR, and liquid nitrogen cooled mercury-cadmium-telluride detector for MIR) and more importantly, the beamsplitters

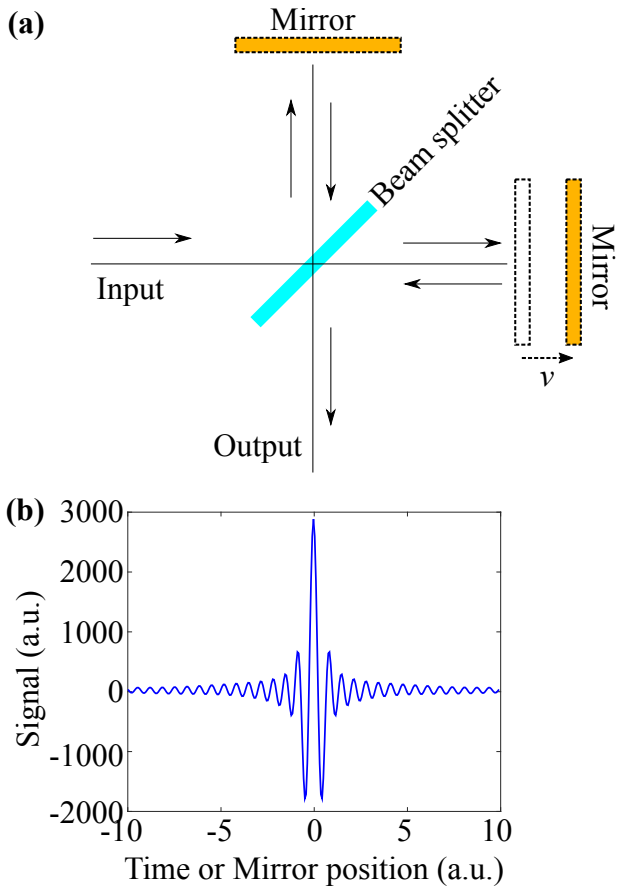

FIGURE 3.10: (a) Schematic diagram of an interferometer. With one mirror at a fixed position and the other mirror moving at a speed p, the output light has an intensity as a function of time (or the position of the moving mirror) due to constructive and destructive interferences. (b) An example of the interferogram.

(quartz beamsplitter for Visible-to-NIR regions and KBr beamsplitter for MIR region).

This FTIR bench is connected to the Bruker Hyperion 2000 FTIR microscope in order to measure nano-resonator arrays. The light is directed out of the FTIR bench through the port OUT 2. The schematic of the microscope is shown in Fig. 3.12. By adjusting the size of the apertures, samples with patterned area as small as 10 µm × 10 µm can be characterized. This microscope also

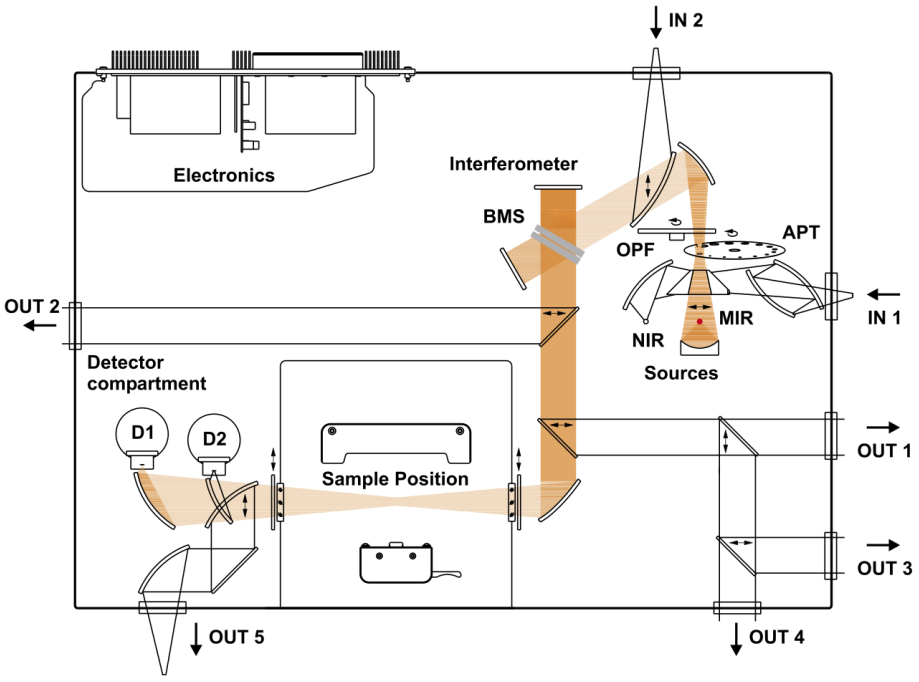

FIGURE 3.11: Schematic diagram of the Bruker Vertex 70 FTIR bench. A broadband light is directed into the interferometer. The light is then focused on the sample and collected by the detector. (https://www.bruker.com/products/infrared-near-infrared-and-raman-spectroscopy/ft-ir-research-spectrometers/vertex-series/vertex-7070v/overview.html)

supports polarizers to be placed in the light path, offering more controls over the measurement.

Three types of objective lenses are used with the FITR microscope. The Cassegrain objective lens consists of a primary concave metal mirror and a secondary convex metal mirror as the focusing components. Due to the reflecting nature, zero chromatic aberration can be realized across the whole infrared region. The cross-section of a typical Cassegrain objective lens is shown in Fig. 3.13. Note that the incident angles are bounded by α_1 and α_2, and there is no normal incident light focused on the sample.

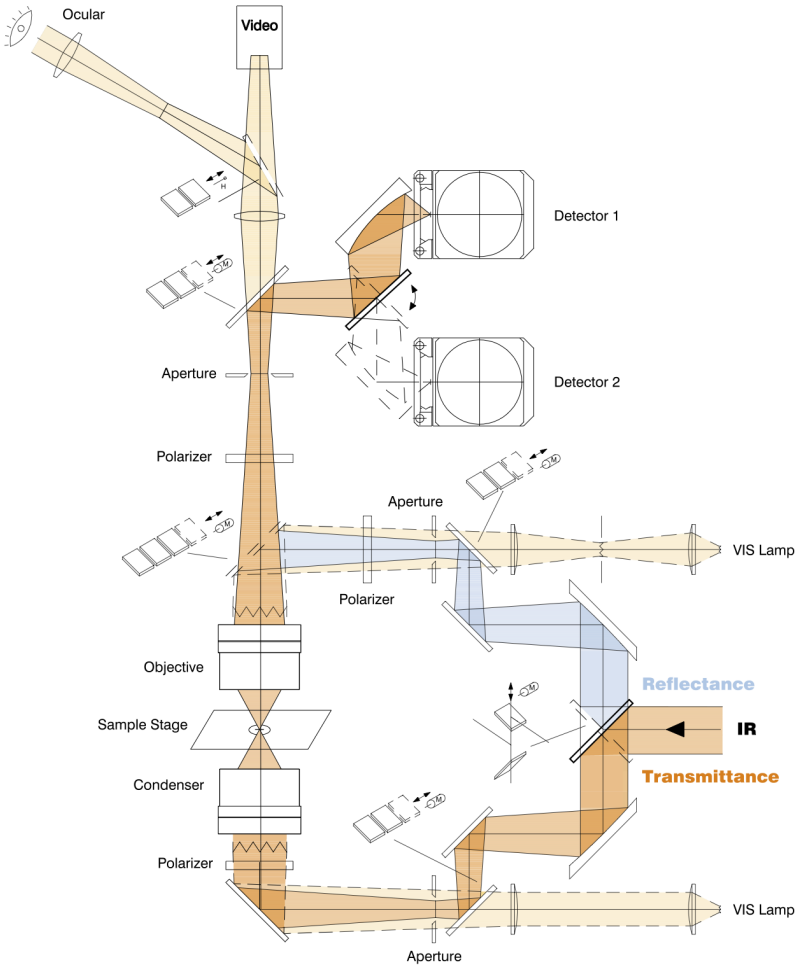

FIGURE 3.12: Schematic diagram of the Bruker Hyperion 2000 FTIR microscope. The light after the interferometer of the Bruker Vertex 70 FTIR bench can be directed into this microscope for spectral measurement over a small area on the sample. The size of the area being measured is be controlled by the aperture. (https://www.bruker.com/products/infrared-near-infrared-and-raman-spectroscopy/ft-ir-microscopes-raman-microscopes/hyperion/overview.html)

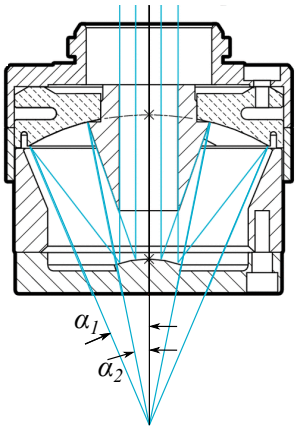

FIGURE 3.13: Schematic diagram of a Cassegrain objective lens. The light is reflected inside the lens instead of being refracted. Incident angle has a range between α_1 and α_2. 25° is used as an estimation of the averaged incident angle in the simulations. (http://www.newport.com/Reflective-Microscope-Objectives/409972/1033/info.aspx)

A grazing angle objective (GAO) lens is also used for measurement. This objective lens provides large incident angles, which are useful to study the modes that require large wave vectors in $xy-$plane or electrical filed in z-axis. Two configurations are shown in Fig. 3.14. Fig. 3.14 a shows the viewing configuration which is used to find the patterns on the sample. Fig. 3.14 b shows the measurement configuration which injects and collects light at large angles.

We have also gained the access to ZnSe IR objective lens. This objective lens has a small numerical aperture ($\sim$ 0.08 NA). Optical responses at near normal incidence can be collected by this objective lens.

3.3.3 Scanning Confocal Microscopy

Scanning confocal microscopy is a technique which is widely used in biology. It has a point source and a spatial pinhole at the conjugate focal plane of the

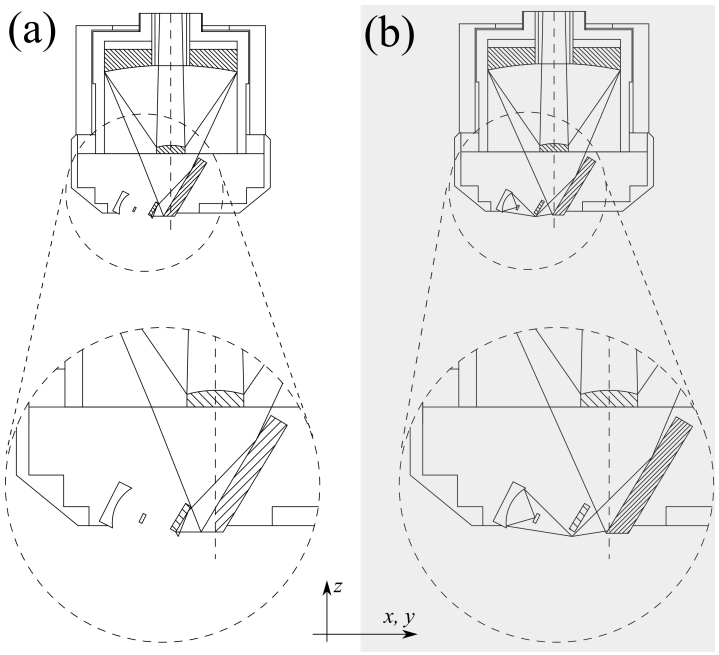

FIGURE 3.14: Schematic diagram of a grazing angle objective (GAO) lens. GAO has two modes. Panel a shows the viewing mode in which the light is focused on the sample from top. Panel b shows the measurement mode in which the light is focused on the sample from left side. 70° is used as an estimation of the grazing incident angle in the simulations. (https://www.bruker.com/products/infrared-near-infrared-and-raman-spectroscopy/ft-ir-microscopes-raman-microscopes/hyperion/accessories.html)

lens, eliminating light that is out-of-focus. The resolution and contrast are increased compared with conventional optical microscopy, and 3D images can be constructed.

The scanning confocal microscope from Nanonics is customized to measure optical field distributions from nano-structures. The schematic shown in Fig. 3.15 illustrates the configuration. A laser beam is injected upwards into the system from the bottom. An objective lens of ten times (10×) magnification is used to slightly focus the laser beam, balancing the power delivered to the sample and the spot size. The upper objective lens (50×) together with a fiber (50 μm in diameter) serves as a pinhole to probe the transmitted EM field. The collected

photons are transmitted through the fiber and detected by an InGaAs IR photon counter.

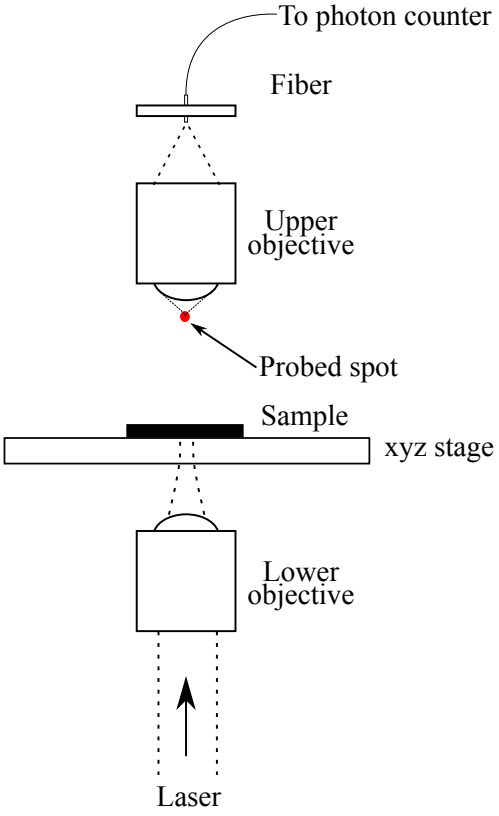

FIGURE 3.15: Schematic diagram of the confocal microscope. The upper objective lens together with the fiber probes the electromagnetic field intensity at a single point in the 3D space marked by the red dot. The intensity distribution of the transmitted field can be mapped by scanning the region above the sample.

Chapter 4

Tunable Nanoscale Resonators

In this chapter, spectral control of nanoscale resonators will be discussed. Phase-change material $Ge_2Sb_2Te_5$ (GST) is chosen to be hybridized with nano-structures to achieve the spectral tuning. Firstly, the optical properties of GST is introduced, followed by a proof-of-concept demonstration of the spectral tuning on a gold nano-disk array. Two applications, namely a tunable perfect absorber and a hot-spot position controller, are therefore discussed in detail. Lastly, phase front manipulation as a result of the spectral tuning is investigated, and a tunable planar lens is further demonstrated.

4.1 Phase-Change Material $Ge_2Sb_2Te_5$

GST is a ternary compound of germanium, antimony, and tellurium which has been widely used in commercial optical disks and phase-change memories. By

varying the ratio among these three atoms, the activation energy for crystallization and the crystallization speed can be varied [63]. GST is employed in this research. It has many attractive intrinsic properties including the large contrast between the amorphous and crystalline phases in terms of the dielectric constant, short tuning time (less than 30 ns), high stability at room temperature, and large cycle number ($> 10^5$ cycles) [37, 41, 63]. Unlike VO_2 thin films [64], the crystallization level of a GST thin film does not change at room temperature. This non-volatile property of GST makes it promising in applications that require zero-standby-power.

The optical properties of the amorphous and crystalline GST thin films are plotted in blue and green colors as shown in Fig. 4.1, respectively [65]. In the near-infrared, the real part of the refractive index changes drastically from the amorphous to crystalline phase, while the imaginary part remains moderately low. This low-absorption wavelength window allows GST to act as a variable dielectric environment for the nano-resonators with manageable losses.

Due to the nucleation-dominated nature, small crystalline nuclei are formed first as GST is heated above its crystallization temperature ($\sim$130 °C). These numerous randomly-distributed small crystals then grow and merge together to form a crystalline structure [66, 67]. Partial crystalized GST can be regarded as a mixture of amorphous and crystalline molecules. A rough estimation of the refractive index can be calculated as $n_{eff} = p \times n_c + (1-p) \times n_a$ and $k_{eff} = p \times k_c + (1-p) \times k_a$, where p ranging from 0 (amorphous) to 1 (crystalline) is the crystallization level, and $n_a + ik_a$ and $n_c + ik_c$ are the refractive indice of amorphous and crystalline

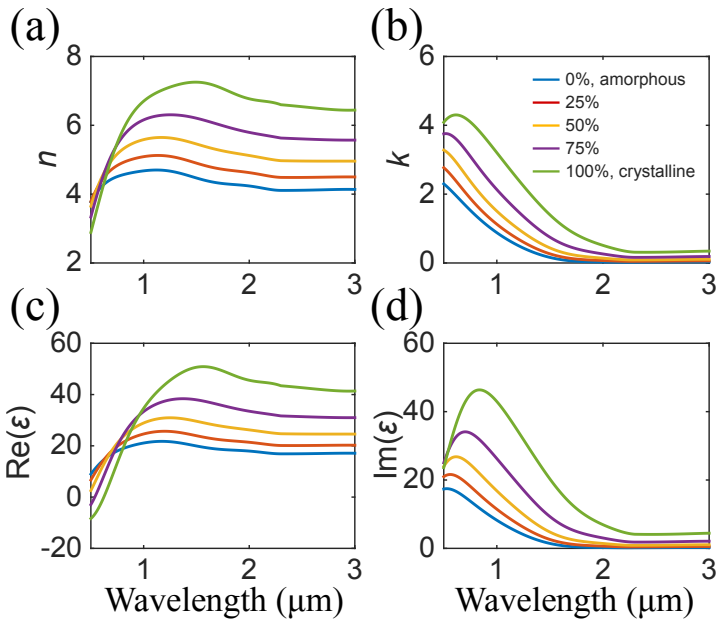

FIGURE 4.1: (a) Real part and (b) imaginary part of the refractive index as well as (c) real and (d) imaginary part of the permittivity of $Ge_2Sb_2Te_5$ at different crystallization levels as a function of wavelength. The crystallization levels plotted here are 0% (amorhpous), 25%, 50%, 75% and 100% (crystalline).

GST, respectively. A more precise approximation can be achieved by applying effective-medium theory using the Lorentz-Lorenz relation [67–69], in which the effective permittivity $\epsilon_{eff}(p)$ of the partially crystallized GST is defined as

$$\frac{\epsilon_{eff}(p)-1}{\epsilon_{eff}(p)+2} = p \times \frac{\epsilon_c - 1}{\epsilon_c + 2} + (1-p) \times \frac{\epsilon_a - 1}{\epsilon_a + 2}\,, \tag{4.1}$$

where ϵ_a and ϵ_c are the permittivities for amorphous and crystalline GST, respectively. The optical properties of the partially crystallized GST with crystallization levels at 25%, 50% and 75% are also plotted in Fig.4.1. Changing the crystallization level of GST can be easily realized through various heating methods, such as electric current, focused laser beam and heat exchange. By precisely

controlling the energy and duration of the heat stimuli, the crystallization level of GST can be tuned to the designed values.[70–72]

A test was conducted to check the crystallization of GST when it was heated. A 20 nm thick GST film was sputtered on a glass substrate, and it was baked on a hot plate at 135°C. At this temperature, it takes about 30 minutes for GST to be fully crystallized. Transmission spectra were measured after every 5 minutes of baking to capture the spectral change due to phase change of GST. A comparison between simulation (dashed lines) and experimental (solid lines) transmission spectra of a GST thin film is shown in Fig.4.2. The simulation results at GST crystallization levels equal to 0%, 10%, 30%, 50%, 70% and 90% are found to match the experimental curves. The decrease in transmission marked by the arrow with the increasing baking time can be clearly seen. This plot suggests that the partially crystallized GST thin films are accessible, and the partially crystallized GST can be well modeled by the effective medium approximation.

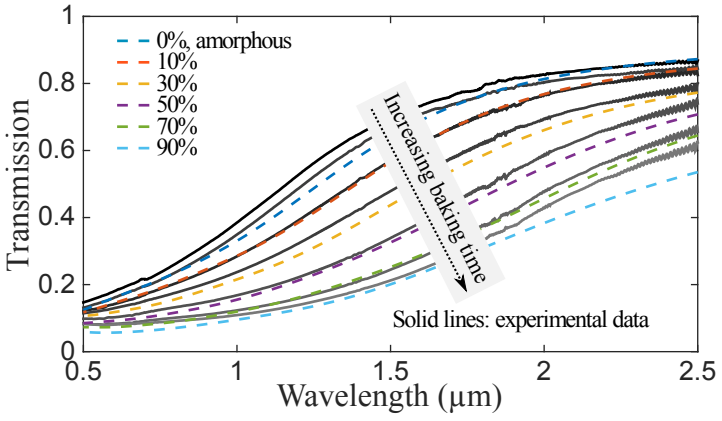

FIGURE 4.2: Transmission spectra of a 20 nm thick GST thin film. The solid lines are the experimental results from one piece of sample measured every 5 minutes during the baking process at 135°C. The dashed lines are the simulation results at different crystallization levels.

4.2 Tuning Lattice Resonance of Au Disk Array

A simple hybrid structure is chosen as a proof-of-concept to demonstrate the resonance tuning. The geometry considered is shown in Fig.4.3. It consists of a GST thin film of 20 nm thickness and a gold nano-disks array above it. The diameter and thickness of each nano-disk are designed to be 280 nm and 40 nm, respectively. The nano-disks are arranged in square lattices with a period of 1.2 μm. This work has been published in Ref. [69].

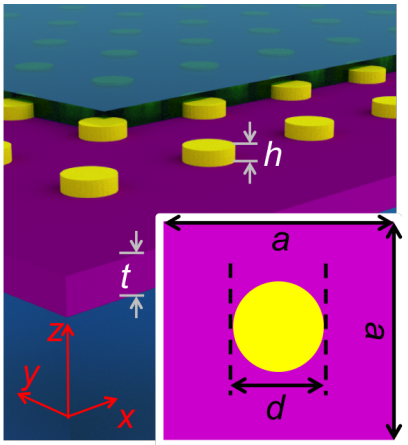

FIGURE 4.3: Schematic diagram of the plasmonic disk array hybridized with phase-change material GST (Reprinted from [69]).

4.2.1 Experimental

The samples were fabricated by the laser interference lithography (LIL). A 20 nm thick GST film was sputtered onto a quartz substrate followed by the e-beam evaporation of a 40 nm gold film. 500 nm thick positive photoresist S1805 was spin-coated followed by a one-minute soft bake at 75°C. The 2-step LIL described in Chapter 3 was then applied to the substrate, with each exposure taking 100

seconds. O_2 plasma was used to trim the photoresist disk array and the pattern of photoresist was transferred to the underneath gold layer by ion milling. 50 nm thick ZnS-SiO_2 was used to cover and protect the structure and provides good thermal conductivity at the same time. The cartoons summarizing the fabrication steps are plotted in Fig.4.4.

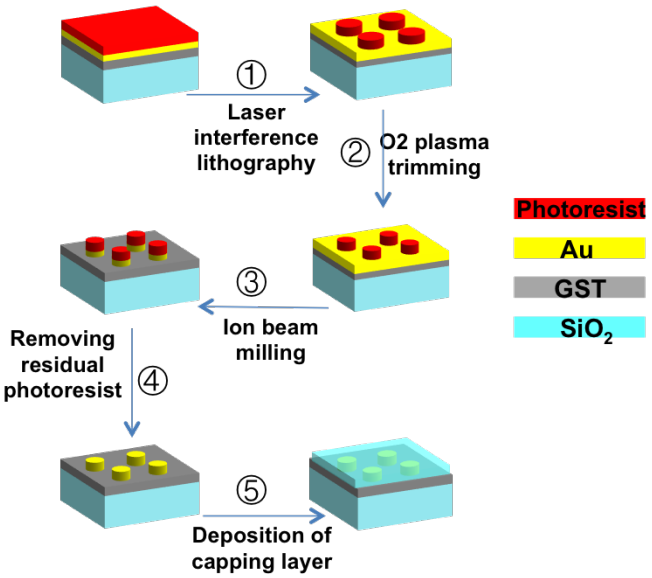

FIGURE 4.4: Fabrication steps of the tunable plasmonic nano-disk array. LIL was used to define the patterns and ion milling was used to transfer the patterns to the gold layer.

In order to study the shift of the resonance, the sample was baked at 135°C for GST to be crystallized, and the spectral measurements of the sample were taken every 5 minutes after rapid cooling to room temperature. The crystallization process was deemed to be finished when the transmission spectra do not show further red-shifts with the extended baking time.

4.2.2 Results and Discussion

From the experimental results, the tuning of the resonance at different crystalline levels are revealed. Fig. 4.5 a shows the measured transmission spectra of the hybrid nano-disk array at different baking time, or different GST crystallization levels. As anticipated, a red-shift of the lattice resonance is observed with an increasing baking time, indicating that the real part of the refractive index n of GST is increased during the process. A total spectral shift from 1.89 µm to 2.27 µm is observed.

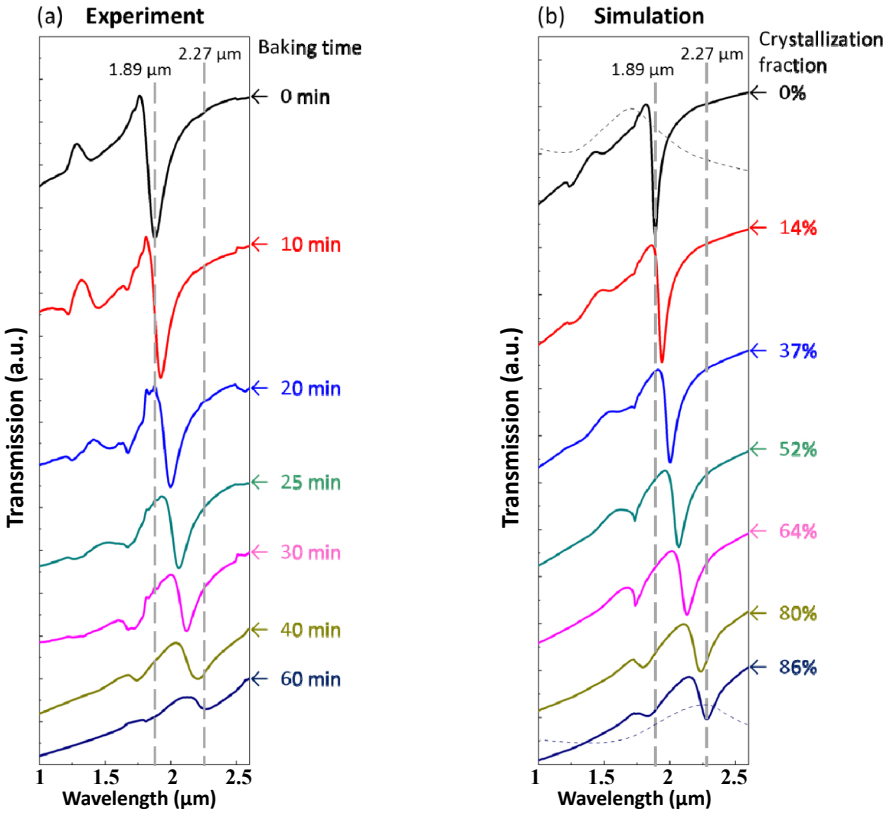

FIGURE 4.5: (a) Transmission spectra of the hybrid nano-disk array measured at different baking time. (b) Tansmission spectra of the hybrid nano-disk array from the FDTD simulations at different crystallization levels (Reprinted from [69]).

FDTD simulations are used for numerical analyses of the proposed structure. A x-polarized broadband plane wave is injected to excite the structure at normal incidence. Periodic boundary conditions are applied to x and y directions of a unit cell containing one disk. The dielectric functions of Au and SiO_2 are obtained from the experimental data of Palik book [73]. By carefully choosing the value p to match the experimental resonance shifts, the corresponding simulated transmission spectra at different crystallization levels are shown in Fig. 4.5 b. A good agreement can be observed between the experimental and simulation results. The gradually widened and shallowed resonance dip as the crystalline level increases can be qualitatively explained by the higher loss associated with the crystalline GST compared with the amorphous GST. When the GST thin film is switched from the amorphous to crystalline phase, the imaginary part of the refractive index, namely the extinction coefficient k, increases. The intensity LSPR on each nano-disk decreases. This can be confirmed by the extinction cross-sections which are plotted in the black and dark blue dashed curves in Fig. 4.5 b, in which a less pronounced LSPR mode is generated when the GST thin film is in the crystalline phase. Moreover, there exists a refractive index mismatch between the substrate (GST on quartz in our case) and the space above the sample (air) and the propagation length of the lattice surface mode is reduced if the mismatch is increased [74]. The increased n of GST from amorphous to crystalline phases, together with the increased k, suppresses the diffractive coupling. It is noticeable that the GST thin film can only be crystallized to a maximum of $\sim$80% in our current experimental apparatus. Such a result may be due to the vacancy defects in the lattice that GST cannot be entirely crystallized

[38], and the possible damage to the GST surface caused by ion milling during the fabrication. These problems are expected to be alleviated by using non-destructive fabrication methods, such as nanostencil lithography [75].

4.2.3 Conclusions

In summary, a GST-hybridized nano-disk array has been investigated. A wide tuning range (∼500 nm) of the lattice resonance has been demonstrated. By controlling the crystallization level of GST, the plasmonic resonance from the gold nano-disk array can be spectrally positioned at any wavelength within the tuning range. This primary study demonstrates the feasibility of spectrally manipulating the resonance of nano-resonators via phase-change material GST, and it served as a fundamental framework for the following studies.

4.3 Tunable Perfect Absorbers

Based on the primary results of tunable nano-resonators shown in the previous section, it is worthwhile to investigate whether GST can be applied in any practical plasmonic structures. One of such structures is the perfect absorber. Perfect absorption is one of the extraordinary optical properties of plasmonics [76–85]. A popular design to achieve perfect absorption is the one-side patterned metal-insulator-metal structure, which has been shown to have an absorption up to 0.99 [77]. This extraordinary property is promising in a variety of applications, for instance, optical modulation, communication and thermal imaging.

Spectrally tunable absorbers based on semiconductor and phase-change materials have been studied before. However, a significant decline in the absorption is observed as the resonance is shifted, which can be no longer regarded as a perfect absorber. Together with the limited tuning range from the demonstrated designs, the drawbacks severely affect the optical performance of these devices.

GST, as a promising alternative, could overcome the disadvantages mentioned above due to the large optical contrast between the amorphous and crystalline the GST films. It is therefore possible to design a perfect absorber that incorporates a thin layer of GST, achieving a significant tuning range, and at the same time minimizing the effect from the loss associated with GST to obtain high-quality absorption peaks.

In this section, I will demonstrate a hybrid perfect absorber which can maintain perfect absorption while the resonance is shifted. This is achieved by carefully controlling the thickness of the insulator layer and the lattice size. This work has been published in Ref. [86].

4.3.1 Design and Simulation

The proposed structure is shown in Fig. 4.6. A GST layer and a SiO_2 insulating layer are sandwiched between the gold nano-disk arrays and the gold mirror. The thickness of GST is fixed at 20 nm. The size of the Au disks is set to be 20 nm in thickness and 300 nm in diameter.

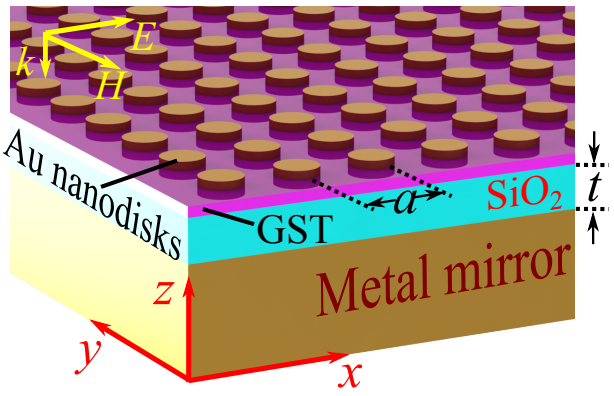

FIGURE 4.6: Schematic drawing of the plasmonic perfect absorber hybridized with phase-change material GST (Reprinted from [86]).

A numerical model was constructed in Lumerical FDTD to investigate the tunable perfect absorption. A unit cell with periodic boundary conditions set in x- and y-directions is defined, and a broadband plane wave polarized in x-axis is injected towards the structure at normal incidence. An example is illustrated in Fig. 4.7 to provide a general idea of the spectral evolution as the GST crystallization level is varied. The lattice constant $a = 800$ nm and the thickness of SiO_2 layer $t = 75$ nm are used in this model. The absorption is defined as 1-Reflection-Transmission, note that transmission equals to zero due to the thick metal mirror at the bottom. As one can easily see in Fig. 4.7, each spectrum has two absorption peaks. The set of peaks at shorter wavelengths in each spectrum is shaded in grey color. As the crystallization level of GST is varied from 0% to 100%, the two sets of peaks shift significantly for a range about 650 nm.

To identify which set of peaks is due to the plasmonic resonance of the nano-disks, the near-field intensity distributions for the corresponding peaks are shown in Fig. 4.8. Without the loss of generality, GST at 0% crystallization level is chosen.

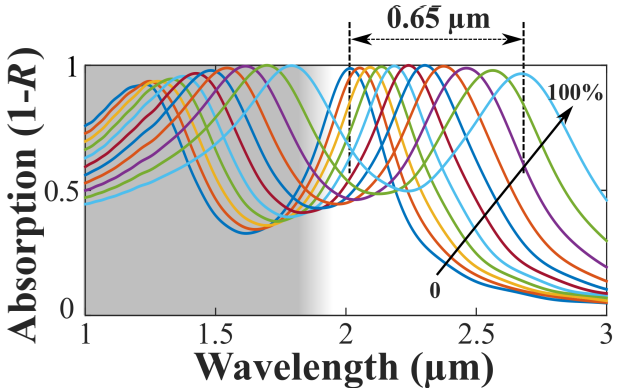

FIGURE 4.7: Absorption spectra of the plasmonic perfect absorber as GST varies from amorphous phase to crystalline phase (Reprinted from [86]).

The normalized electric field distribution in the xy plane at 10 nm above the GST layer of the peak at the longer wavelength (the 2nd peak, $\lambda \sim 2\mu m$) is plotted in Fig. 4.8 a, showing a clear dipole-like pattern. In contrast, the electric field distribution of the peak at the shorter wavelength (the 1st peak, $\lambda \sim 1.2\mu m$) reveals no obvious hotspots, as shown in the inset of Fig. 4.8 a. Note that the main panel and the inset of Fig. 4.8 a share the same color bar. Therefore, it can be concluded that the 1st peak is not a result of the plasmonic resonance.

Fig. 4.8 b reveals that the localized electric fields of the dipolar resonance tunnel through the underneath GST and SiO_2 layers, and extend to the metal mirror in the $-z$ direction. The strong coupling between the Au disks and the mirror results in a magnetic resonance confined in the sandwiched region (Fig. 4.8 c). The combined response of the electric and magnetic fields leads to an impedance matching between the free space and the proposed structure. The matched impedance manifests as $\sim$ 0% reflection or $\sim$ 100% absorption. For the 1st peak on the other hand, the corresponding near-field intensity distributions are plotted as the insets in Figs. 4.8 b and c. These near-field distributions suggest

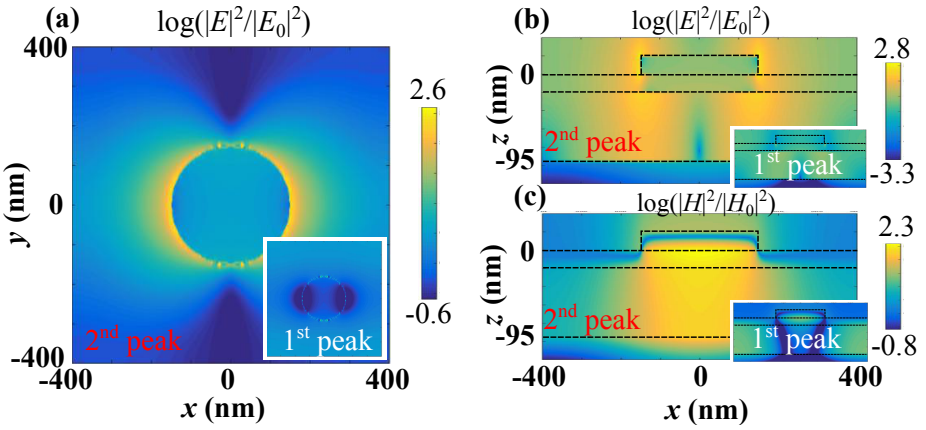

FIGURE 4.8: (a) The normalized electric field intensity distribution in the xy cross section at 10 nm above the GST layer. The intensity distribution of (b) electric and (c) magnetic fields in the xz cross section along the diameter of the disk. Panels (a) – (c) are extracted from the perfect absorber with amophous GST (0% crystallized) at the peak of longer wavelength (2nd peak). The insets in Panels (a) – (c) are the corresponding near-field distribution at the peak of shorter wavelength (1st peak) (Reprinted from [86]).

that the 1st absorption peak is due to the destructive interference as a result of the multi-layer structure.

4.3.2 Results and Discussion

The focus of the discussion is on the 2nd absorption peaks because of the plasmonics nature and their attractive properties, for instance, it is obvious that the 2nd absorption peaks have the larger localized field enhancement, and the absorptions are closer to the unity. Indeed, at the resonant wavelength, the impedance experienced by the incident light can be well-matched to free space, so the reflection is almost zero. And due to the thick metal mirror, no light transmits through the structure. Therefore, light is confined in the sandwiched layers between the Au disks and the mirror. The confined light further changes to other form of energy – heat, due to the Ohmic losses from the metal. And

eventually, this energy dissipates back into the environment. The main purpose of GST in this design is to shift the resonance. However, the side effect is the impedance change of the whole structure that decreases the absorption due to the change of GST's optical property. To study the performance, absorption values at the peaks are plotted as a function of the GST crystallization level together with the corresponding quality factors (Q-factors), as shown in Fig. 4.9. When the crystallization level of GST is 60%, the absorption reaches 0.999, which is the maximum value in the sampled data. Although the absorption is smaller at other crystallization levels, the absorption is still reasonably high and the minimum value is 0.965 when GST is 100% crystallized. The Q-factors of the peaks drop from 6 to 4 as the crystallization level of GST increases. This decreasing trend is expected because the Ohmic losses associated with the crystalline GST are increased, which results in the broadened line shape of the resonance.

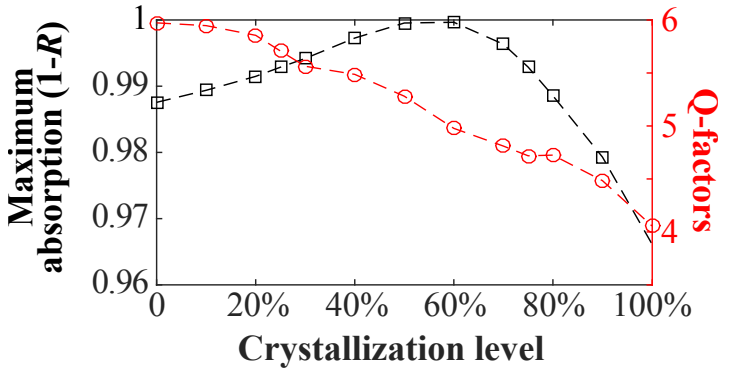

FIGURE 4.9: Maximum absorption at the 2nd peak and the quality factor of the 2nd peak as functions of crystallization fraction (Reprinted from [86]).

To maintain a high absorption at every crystallization level, the general idea is to design a structure with the largest absorption value happening around the half crystalline phases and reasonable absorption values at both 0 and 100%

crystallization. Therefore, the effects of lattice constant a and the thickness of the SiO_2 layer t are investigated. 2D color maps are used to illustrate the absorption value at the plasmonic resonance when the two parameters are varied. The color range is set to display any value below 0.95 as dark blue and any value above 0.97 as bright yellow. Note that the number 0.97 is regarded as a reference value to define if an absorption is "perfect". Considering the two extreme crystallization cases (0% and 100%), two color maps are presented in Fig.4.10. A band highlighting the combinations of a and t, which result in more than 0.97 absorption can be clearly seen in each case. The overlapping region of these two maps indicates the values of a and t that support "perfect" absorption. The example demonstrated in Figs. 4.7–4.9 with $a = 800$ nm and $t = 75$ nm falls inside the enclosed region. It is worth mentioning that the two maps share a similar pattern that a and t need to change in proportion to maintain "perfect" absorption. This observation has also been confirmed by the circuit models used in the studies of the Terahertz perfect absorbers [87, 88]. From the circuit-based view, the change of the refractive index in the GST layer not only shifts the resonant wavelength of the Au disks, it also modifies the impedance of the structure [87–89]. Fortunately, if the GST layer and the SiO_2 layer are considered as one component in the circuit model, the impedance change caused by the crystallization variation in the GST layer is averaged by the thicker and fixed SiO_2 layer, limiting the overall impedance change of the whole structure caused by the phase change of GST. This explanation can be confirmed by the region marked by the red dashed lines in Fig. 4.10, where a larger thickness of SiO_2 corresponds to a wider range of lattice constant that

satisfies the perfect absorption.

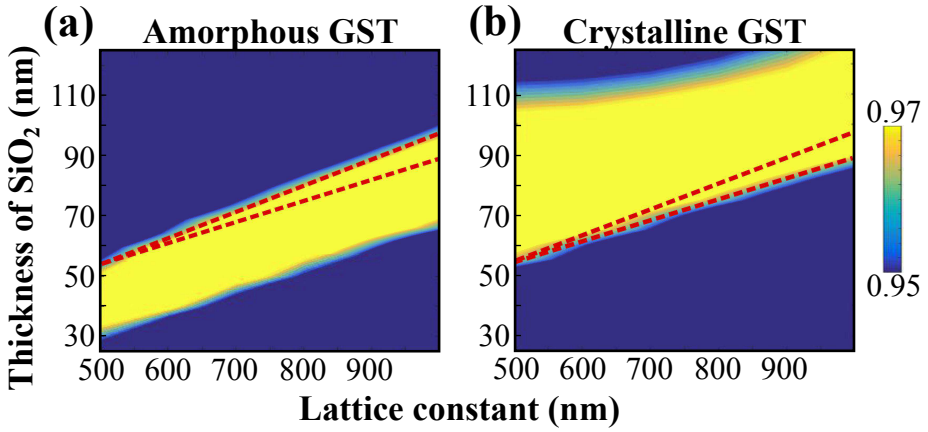

FIGURE 4.10: 2D color maps present the absorption at the plasmonic resonance as a function of lattice constant (x axis) and the thickness of SiO_2 layer (y axis) for (a) amorphous and (b) crystalline GST (Reprinted from [86]).

4.3.3 Conclusions

To summarize, a tunable perfect absorber which can maintain an absorption more than 97% have been demonstrated. The optical contrast associated with GST at different crystallization levels provides a variable dielectric environment for the Au disks which results in the significant spectral shifts. Moreover, the hybrid design of the GST layer on top of the SiO_2 layer limits the change in impedance, maintaining high absorption across the large tuning range.

4.4 Controlling Hotspots in Sub-diffraction Scales

The studies in the previous sections were based on broadband sources, and demonstrated the spectral shifts of the resonators. In this section, a GST-based

system to control the positions of near-field hotspots at a single wavelength will be discussed. This work has been published in Ref. [90].

4.4.1 Design and Simulation

Plasmonic resonators with slightly different resonant frequencies can strongly interference with each other if the distance between them falls into a certain range, forming anti-Hermitian coupling [91]. Anti-Hermitian coupling manifests as a constructive interference taking place in one resonator while destructive interferences in the other resonators. A localized hotspot is therefore generated in such a plasmonic system. In the Zhang's work, the position of the hotspot depends on the wavelength of the excitation beam [91]. Moving forward from his idea, if monochromatic light is used to excite the structure and the resonant wavelengths of the resonators are controlled by a GST film, selective excitation of each resonator can be achieved at different GST crystallization levels. In other words, the spatial manipulation of hotspots with a monochromatic light can be realized.

The proposed structure is drawn in Fig. 4.11. Five pairs of Au nano-bars are placed on a 15 nm-thick layer of GST. The length l of the bars 1 to 5 are 218, 180, 150, 135 and 120 nm, from the longest to the shortest, and the corresponding gap g are 20, 16, 14, 14 and 12 nm. These different values in the lengths and gaps of the resonators are chosen in order to a have comparable field enhancement when each pair of the nano-bars is excited. The centre-to-centre distance d

between the neighboring resonators in y-axis is 100 nm, and the width w and the thickness h of all the resonators are 40 nm.

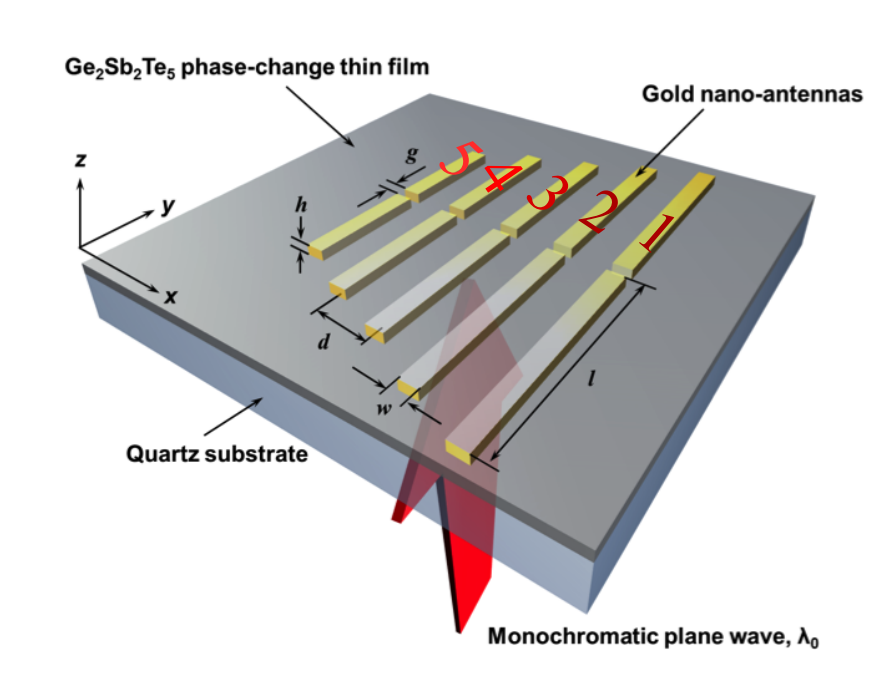

FIGURE 4.11: Schematic diagram of the design for hotspot control. By setting the GST crystallization level, a hotspot can be selectively generated in one of the five gaps of the dipole nano-resonators. The length l of the resonators 1 to 5 are 218, 180, 150, 135 and 120 nm, respectively. The corresponding gap g are 20, 16, 14, 14 and 12 nm (Reprinted from [90]).

Numerical simulations using FDTD are employed to investigate the structure's performance. The structure shown in Fig. 4.11 is enclosed by perfectly matched layers. A total-field scattered-field source (TFSF) is used to excite the structure from the substrate side. Five point monitors are placed in the centers of the five gaps. Firstly, to identify the resonant wavelengths of the nano-bars, a broadband light is injected. Figs. 4.12 a–e show the normalized electric fields recorded by the five point monitors as GST is being crystalized. The percentage marked in each panel is the corresponding crystallization level of GST. It can be seen

that as the GST crystallization level increases, the resonance of each resonator gradually red-shifts. As shown from Figs. 4.12 b–e, the resonant wavelengths recorded in gap 2, 3, 4 and 5 overlap with the resonant wavelength recorded in gap 1 (Fig. 4.12 a) one after another.

Under the single wavelength excitation at $\lambda = 2.16\,\mu$m, the hotspot is selectively excited in one of the five gaps. When the GST thin film is in the amorphous phase, only the the longest antennas are excited, whereas the others are suppressed. By increasing the GST crystallization level, the other four paris of nano-bars are resonating one after another at the working wavelength. The corresponding electric field enhancements at $\lambda = 2.16\,\mu$m are plotted in Figs. 4.12 f–j. The nanoscale energy hotspot is observed to be positioned from gap 1 to gap 5 with the increased GST crystallization levels. Based on the geometry, a step resolution of $\lambda/20$ ($\sim$100 nm) is obtained, which is beyond the diffraction limit.

As pointed out in Ref. [91], the distance d between the neighboring pairs of nano-bars is a crucial parameter, which determines if the selective excitation of the plasmonic resonators can be achieved. In the reference paper, direct near-field coupling dominates at a very small d ($d < 60\,$nm), whereas if d is very large ($d > 390\,$nm), the nano-bars are uncoupled. For our proposed structure, the spectra of the electric field enhancements at $d = 50\,$nm are plotted in Figs. 4.13 a–b to show the situation in which the near-field coupling dominates. In Figs. 4.13 c–d, the spectra of the electric field enhancements at $d = 500\,$nm are plotted to show the effect of uncoupled resonators. As can be observed, the selective excitation of an individual pair of resonators is impossible in these two cases.

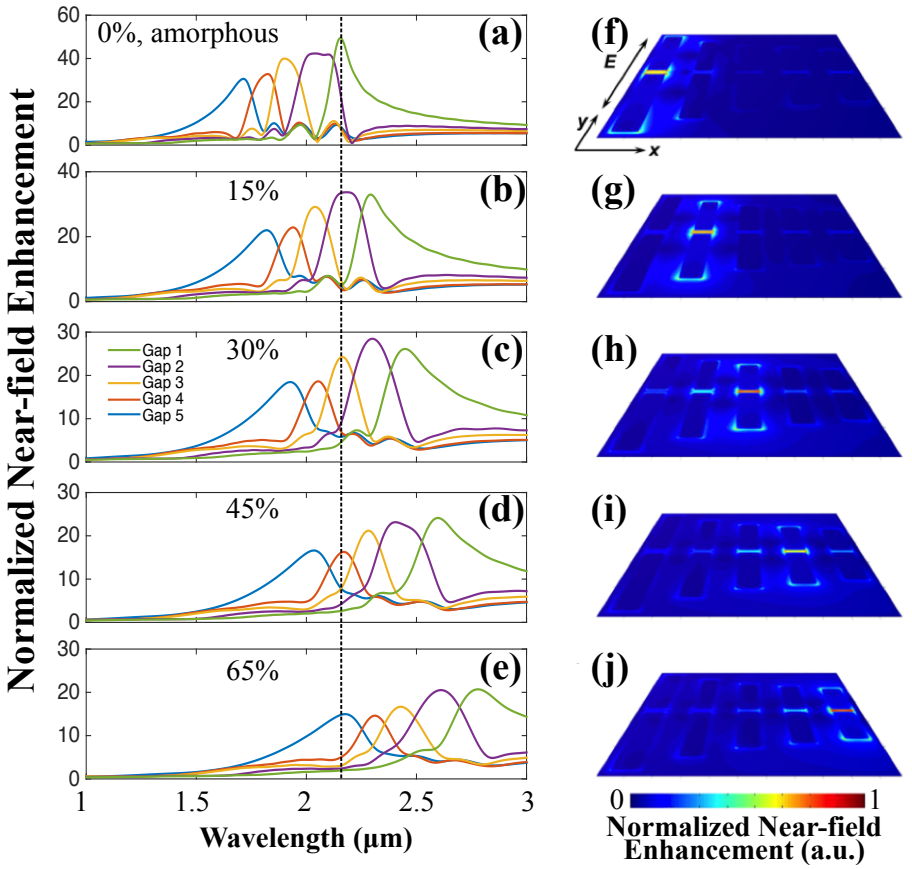

FIGURE 4.12: Near-field enhancement recorded in the gaps of the five pairs of nano-bars as the GST crystallization level set to be at (a) 0% to (b) 15%, (c) 30%, (d) 45% and (e) 65%. The dashed line marks the monochromatic wavelength at 2.16 μm. (f)–(j) The corresponding near-field distributions at $\lambda = 2.16\,\mu m$ for the crystallization levels used in panels (a)–(e) (Reprinted from [90]).

4.4.2 Conclusions

To sum up, controlling the position of the near-field hotspots has been demonstrated through a GST-based plasmonic system. Monochromatic light at $\lambda = 2.16\,\mu m$ is injected to excite the structures. The selective excitation of each individual pair of nano-bars is based on anti-Hermitian coupling. By assigning the corresponding crystallization levels to the GST layer, only one of the five

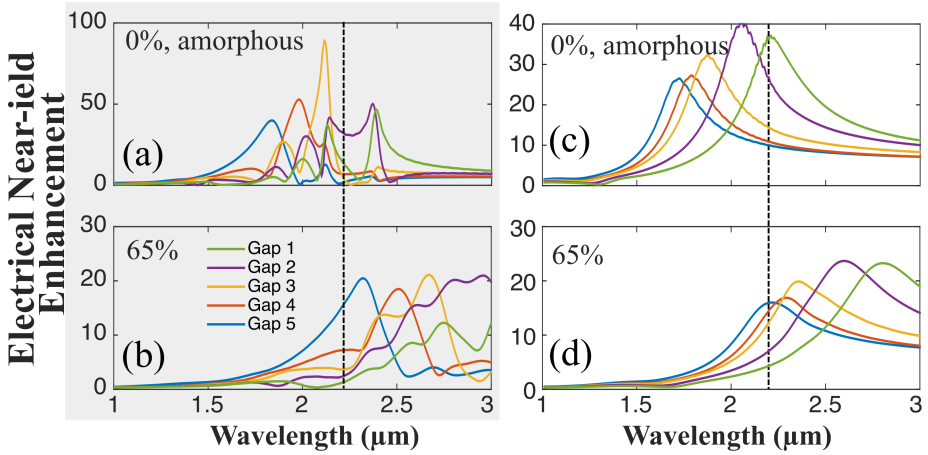

FIGURE 4.13: Panels (a) and (b) demonstrate the near-field enhancement recorded at $d = 50\,\text{nm}$. The direct coupling between the nano-bars dominates at this small d, and the selective excitation of the nano-bars is not observed. Panels (c) and (d) demonstrate the near-field enhancement recorded at $d = 500\,\text{nm}$. Because the antenna are uncoupled at this large d, no selective excitation of the nano-antennas is observed in case.

nano-resonators is resonating at the working wavelength, while the others are suppressed. This work demonstrates that the location of a near-field hotspot can be manipulated by GST-based plasmonic resonators.

4.5 Tuning Resonances of Slits in a Metal Film

Planar lens is a hot research area in plasmonics and nanophotonics. With the growing interest in developing ultra-compact optical systems, the capability of manipulating light at nanoscale becomes increasingly important. Many types of planar lenses have been proposed, for instance photonics crystals [92], zone plates [93–95], and nano-patterned surfaces [96–102]. Among them, nano-slit arrays in a metal film can be regarded as the fundamental design, where each slit transmits light at a certain phase. If each slit is controlled separately, the

phase front of the transmitted light can be engineered to form different focusing patterns. Moving forward from the discussion about tuning the resonances of nanoscale particles, the spectral tuning of slits in a metal film will be discussed in the following sections, together with its application as a tunable planar lens. This work has been published in Ref. [103]

4.5.1 Resonance of a Single Slit

A schematic diagram illustrating the basic structure is plotted in Fig. 4.14 a. A slit in a metallic film is filled with GST. The structure is excited by a transverse magnetic (TM) wave injected from the substrate side. Since GST has a higher refractive index than the air and the substrate (both amorphous and crystalline GST have $n > 4$ at the wavelengths between 1 μm and 2 μm) [63], the GST-air and GST-quartz interfaces serve as mirrors, forming a Fabry-Pérot (FP) cavity which supports a strong resonance. The x-component of the electric field E_x is manifested by the colors in Fig. 4.14 a, illustrating the 1st order FP mode supported by the structure. The FP mode leads to an extraordinary optical transmission (EOT) into free space from the GST-air interface, which can be identified from the transmission spectrum [104–106]. The resonant wavelength λ_{FP} in free space can be roughly estimated as $\lambda_{FP} \propto (h/N) \times n$, where n denotes the refractive index in the slit, h is the height of metallic film and N is the order of the FP mode. Note that perfect reflection at the top and bottom interfaces of the slit is assumed, and the substrate is ignored. This expression suggests that this mode can be shifted with n.

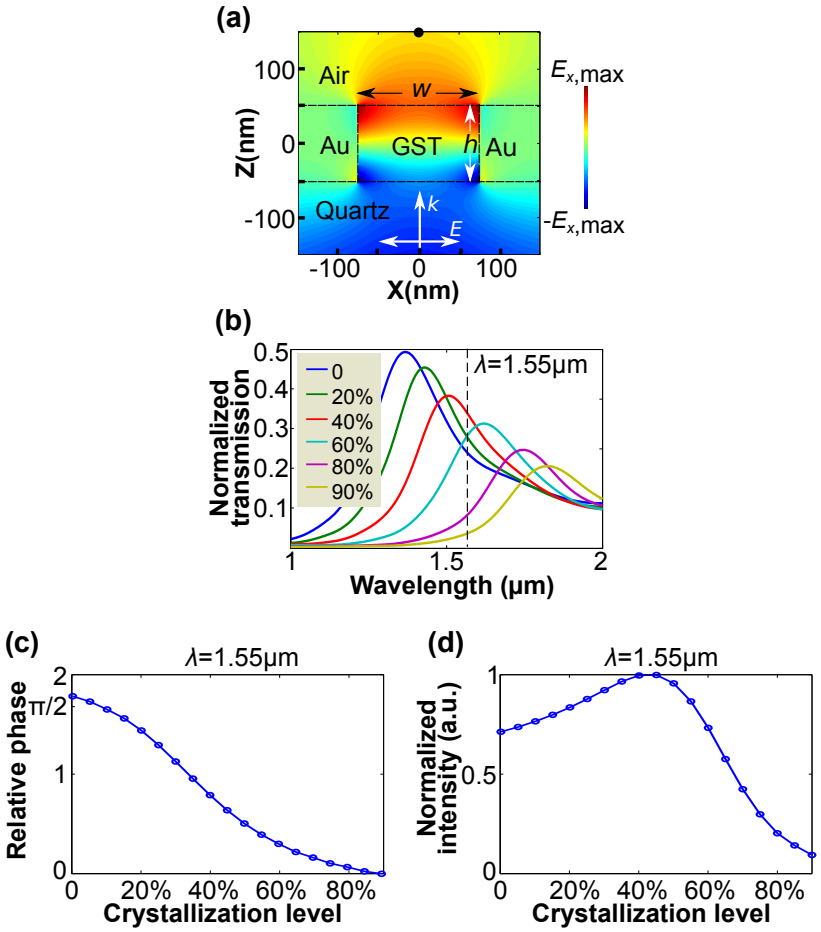

FIGURE 4.14: (a) Electric field distribution of the 1st order Fabry-Pérot resonance supported by the slit. (b) The normalized transmission of the single slit as a function of the GST crystallization level. (c) and (d) The relative phase and normalized intensity measured at the 1.55 μm as a function of the GST crystallization level, respectively. The phase and intensity are collected at the point monitor marked by the black dot in (a) (Reprinted from [103]).

FDTD from Lumerical Solutions, Inc. was used to analyze the optical properties of the single-slit. The structure is constructed in a 2D configuration, enclosed by Perfectly Matched Layers (PML). A x-polarized plane wave is launched toward the structure at normal incident angle. The thickness of the gold film and slit width are $h = 100\,\text{nm}$ and $w = 150\,\text{nm}$ as shown in Fig. 4.14 a. In the slit region, the mesh size is set to be 2 nm by 2 nm. The transmission spectra at various GST crystallization levels are plotted in Fig. 4.14 b. These spectra are normalized

to the transmission spectrum of a slit with the same geometry but filled with air ($n = 1$). As can be observed clearly, the EOT peak is shifted across the telecom wavelength at 1.55 μm. The nature of an oscillator suggests that a phase difference as large as $\pi/2$ can be introduced by detuning the driving frequency across the resonant frequency. From another perspective, if the driving frequency is fixed but the resonant frequency is changed across the driving frequency, the phase of the oscillator is expected to be tuned. Based on this idea, under a monochromatic illumination at 1.55 μm, a considerable phase modulation could be achieved via the spectral tuning of the EOT peak.

To study the phase modulation, a point monitor located along the central axis of the slit and 100 nm above the GST-air interface is used to probe the transmitted electromagnetic field at 1.55 μm. Fig. 4.14 c shows the relative phase as a function of the GST crystallization level at a 5% step increment. The result at 90% crystallized GST is used as the reference so that the values are all positive in sign. Due to the spectral shift of the EOT peak across the working wavelength, the phase difference recorded at $\lambda = 1.55\,\mu\text{m}$ is found to be $0.56\,\pi$. In the control simulation, a 100 nm thick GST film without any metallic structures can only achieve a phase modulation of $0.15\,\pi$ under the same conditions. Due to the resonant nature, the intensities of the transmitted fields are not equivalent during the tuning. Fig. 4.14 d shows the normalized intensity of the transmitted field as a function of crystallization level probed by the same point monitor. The maximum intensity occurs at the GST crystallization level equals to 45%, and this value is used as the reference for normalization.

4.5.2 Theoretical Demonstration of the Focus Tuning

A schematic diagram of the proposed planar lens structure is shown in Fig. 4.15 a. Twenty one of the slits discussed in Fig. 4.14 a are arranged side-by-side. This slit array spans $W = 10\,\mu m$ laterally and the center-to-center distance between the neighboring slits is 500 nm. Similar to the conventional optical lenses, the focusing pattern of a far-field planar lens is determined by the transmitted electromagnetic phase front. The equal optical length principle can be used to predict the electromagnetic phase distribution along x-axis on the lens plane. Suppose a focal point is defined by the nominal focal length $f_{nominal}$ and the nominal lateral offset $l_{nominal}$ with respect to the lens axis at $x = 0$, the phase distribution $\phi(x)$ on the lens surface is calculated as [98, 100]

$$\phi(x) = 2m\pi + \frac{2\pi f_{nominal}}{\lambda} - \frac{2\pi\sqrt{f_{nominal}^2 + (x - l_{nominal})^2}}{\lambda}, \qquad (4.2)$$

where λ is the operating wavelength and m is an integer to keep ϕ within the range from 0 to 2π. To tune a lens, which translates into assigning different values to $f_{nominal}$ and $l_{nominal}$, the lens is required to generate distinct transmitted phase fronts calculated by Eq.4.2.

Note that the phase coverage from the GST-filled slit has a range from 0 to 0.56π, but $\phi(x)$ in Eq.4.2 can be any value between 0 and 2π. To investigate the effect due to the shortage of the phase coverage and prove the feasibility of the proposed tunable lens, it is worthwhile to analytically study the focusing performance of such a lens.

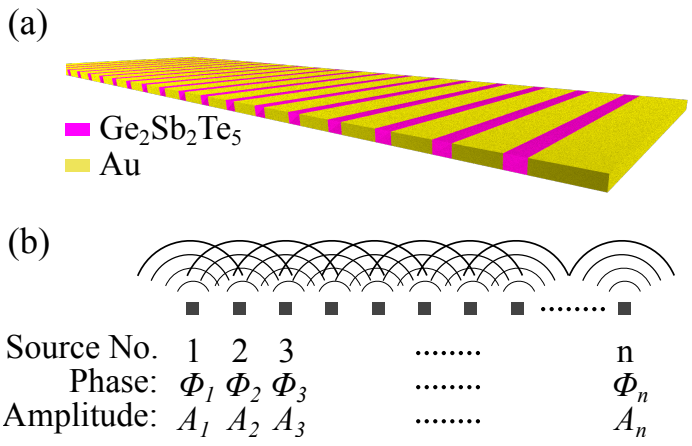

FIGURE 4.15: (a) Schematic of the planar lens. (b) Point source array used in the theoretical calculation to demonstrate how the focal point behaves when the phase ϕ and the amplitude A of each source are pre-designed under several situations.

A 2D analytic model is constructed in MATLAB. The idea is shown in Fig. 4.15 b. The 21 slits are represented by 21 point sources, which radiate p-polarized electromagnetic waves at predefined intensities and phases. For simplicity, the effect of surface plasmons excited on the Au film is not considered in this analytic model. Since $w^2/\lambda = 0.015\,\mu\text{m}$, which is much smaller than the distance between the slit and the positions we consider in the space (the slit width $w = 150\,\text{nm}$ and the wavelength $\lambda = 1.55\,\mu\text{m}$), the angular intensity distribution $P(\theta)$ of the radiation from each source is modeled by the Fraunhofer diffraction pattern based on Ref. [107], which can be expressed as

$$P_n(\theta)^2 = \left(P_n \frac{\sin(\pi w \sin\theta/\lambda)}{(\pi w \sin\theta/\lambda)} \right)^2, \tag{4.3}$$

where n is the index of the source, w represents the width of the slit (150 nm), $\lambda = 1.55\,\mu\text{m}$, and θ is the angle of direction relative to z axis. Note that the

Bessel function in Ref. [107] is replaced by a sin function. This is because these two functions have only a maximum difference of 0.36% within the range of $\pi w \sin\theta/\lambda$. The electromagnetic field at any position in the 2D space above the lens plane can be regarded as a superposition of the waves from the 21 sources. For a point at the coordinate of (x, z) in the 2D plane, the complex H-field contributed by the 21 sources can be expressed as

$$H \propto \Sigma_{n=1}^{21} P_n(\theta) \frac{1 - \lambda/(i2\pi r)}{r} e^{(i2\pi r/\lambda - \phi_n)}, \tag{4.4}$$

where $\theta = \arctan((x - x_{source}(n))/z)$ and $r = \sqrt{(x - x_{source}(n))^2 + z^2}$. The magnetic field intensity, expressed as $|H|^2$, is calculated at the positions across the area ($-10\,\mu\text{m} \leq x \leq 10\,\mu\text{m}$, $2\,\mu\text{m} \leq z \leq 42\,\mu\text{m}$) with 0.04 µm and 0.08 µm separations in x- and z-directions, respectively. $f_{analytic}$ is defined as the z-coordinate of the point of the maximum intensity in the focusing region from this analytic model.

Three cases are considered in the analytic model. The "optimal" planar lens stands for the case that the the phase of each source ($\phi(n)$) is set to be the value determined by Eq.4.2, and the amplitude ($A(n)$) is set to be 1 for all the sources. The "quasi-optimal" planar lens stands for the case that if the calculated $\phi(n)$ of a source is within the range of the GST-slit shown in Fig. 4.14 c, the nearest phase and the corresponding amplitude from the data shown in Figs. 4.14 c and d are assigned to this source. Otherwise, ϕ from Eq.4.2 and amplitude equal to 0.5 will be assigned. Finally, the "realistic" planar lens stands for the case in which only

the phase and amplitude values from Figs. 4.14 c and d are used. If the ϕ from Eq.4.2 is between 0 and 0.56π, the nearest phase data from Fig. 4.14 c and the corresponding amplitude from Fig. 4.14 d are used; if $0.56\pi < \phi < \pi$, the phase and amplitude values at 90% crystallized GST are used; if $\phi \geq \pi$, the value at 0% crystallized GST are used. The "realistic" case serves as an approximation of the proposed planar lens, and the effects of the associated phase coverage shortage and amplitude variation can be revealed from the comparison among the three cases.

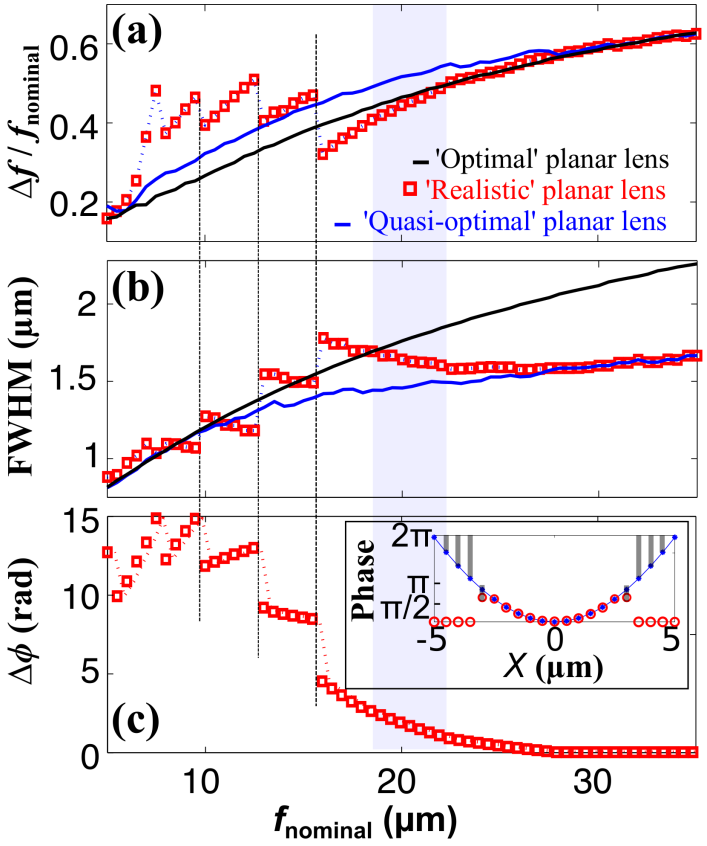

FIGURE 4.16: (a) Focal deviation as a function of the nominal focal length. (b) Full-width at half maximum of the focus as a function of the nominal focal length. (c) Total phase difference accumulated from the 21 point sources in the "realistic" case compared with the "Optimal" case (Reprinted from [103]).

The relative focal deviation $\triangle f / f_{nominal}$ as a function of the $f_{nominal}$ is reported

in Fig. 4.16 a, with $\triangle f$ denoting $|f_{nominal} - f_{analytic}|$. The corresponding full width at half maximum (FWHM) in the x-axis at the focal point is shown in Fig. 4.16 b. It can be seen that both the "optimal" (black curve) and "quasi-optimal" (blue curve) lenses show an increasing focal deviation and FWHM as $f_{nominal}$ increases. At $f_{nominal} < 27.5\,\mu m$, the focal deviation of the "optimal" case is smaller than the "quasi-optimal" case, but "optimal" case possesses a larger FWHM compared with the "quasi-optimal" case. The results of the "realistic" planar lens, denoted by the red squares, have a zigzag pattern in Figs. 4.16 a and b, fluctuating around the reference curves. At large $f_{nominal}$ ($f_{nominal} > 27.5\,\mu m$), $\phi(x)$ calculated by Eq. 4.2 is within the phase modulation range at any x on the lens plane. Therefore, the "realistic" and "quasi-optimal" cases overlap in both Figs. 4.16 a and b since the two cases share the same intensity and phase configuration for each source. For the "optimal" case, it overlaps with the other two cases in terms of the focal deviation, but continues deviating from the other two in terms of FWHM. For the sake of completeness, the phase error ($\triangle\phi$) is shown in Fig.4.16c. This panel explains the discontinuous behavior of "realistic" planar lens in Figs. 4.16 a and b. As an example of how $\triangle\phi$ is calculated, phase configuration at $f_{nominal} = 7.5\,\mu m$ is illustrated in the inset of Fig. 4.16 c. The grey bars denote the phase difference at the each source position. As highlighted by the dashed lines across Figs. 4.16 a-c, the "realistic" planar lens has the same discontinuous zones across the three plots. It can be seen that the abrupt changes in FWHM and $\triangle f$ are due to the discontinuities in $\triangle\phi$. The cause of the discontinuities in $\triangle\phi$ can be ascribed to the piecewise function which is used to determine the phase and intensity of each source.

Several conclusions can be drawn from these three plots. Firstly, the trade-off between the focal deviation and FWHM of a lens is obvious. This can be explained through numerical aperture (NA). Since $f_{analytic}$ is always smaller than $f_{nominal}$ [108], a smaller $\triangle f$ corresponds to a larger $f_{analytic}$ for a fixed $f_{nominal}$, and therefore a smaller NA (the width of the lens is fixed). Because FWHM is inversely proportional to NA, a smaller $\triangle f$ means a larger FWHM. Secondly, $\triangle \phi$ and the slit-to-slit intensity variation, at certain situations, may improve the focusing patterns. As highlighted by the blue band, the "realistic" planar lens shows better performance in terms of both FWHM and $\triangle f$ compared with the "optimal" situation. Indeed, Eq.4.2 assumes the nominal focal point radiates electromagnetic field uniformly in every direction. Once a finite width is assigned to our lens, only a tiny fraction of information from the point source is recorded and used to reproduce the focus. None of the cases considered has abundant information of the focal point due to the small Fresnel number (FN), which is defined as

$$FN = \frac{W^2}{\lambda f_{nominal}} \tag{4.5}$$

where W and λ are the lens span and the working wavelength, respectively. The additional information carried with $\triangle \phi$ and intensity variation can improve the focus in a few situations, such as the band highlighted in blue color.

One may raise questions about the focal deviation associated with the analytic models discussed above. All the three cases demonstrate focal deviation due to

TABLE 4.1: Parameters of planar lenses for comparison

	Lens 1	Lens 2
Lens span, W	10 μm	32 μm
Working wavelength λ	1.55 μm	1.55 μm
Number of point sources	21	21
Nominal focal length, $f_{nominal}$	13.95 μm	44.64 μm
Analytic focal length, $f_{analytic}$	8.92 μm	41.55 μm
$\lvert f_{analytic} - f_{nominal} \rvert / f_{nominal}$	36.1%	6.9%
Numerical aperture, NA	0.34	0.34
The Fresnel number, FN	4.6	14.8

the small FN of the proposed geometry, and will be discussed later. The effect of FN on the focal deviation needs to be emphasized.

To start the discussion, consider the following two planar lenses: lens 1 has a $W = 10\,\mu m$, $f_{nominal} = 13.95\,\mu m$, and $\lambda = 1.55\,\mu m$; lens 2 has a $W = 32\,\mu m$, $f_{nominal} = 44.64\,\mu m$ and $\lambda = 1.55\,\mu m$. Simple calculation shows that these two lenses share the same NA (~ 0.34), however, lens 2 can achieve a much smaller focal deviation compared with lens 1. The specifications of the two lenses calculated by using the "optimal" configuration are summarized in Table 4.1. It can be observed that if λ is not much smaller than W, NA is not adequate to describe a planar lens, since λ is not taken into consideration. FN, on the other hand, is more precise in this situation [108]. As can be seen in Table 4.1, as FN increases from 4.6 (lens 1) to 14.8 (lens 2), the focal deviation reduces from 36.1% to 6.9%. Meanwhile, NA is kept as a constant. It can be concluded that the focal deviation is mainly due to the small W with respect to λ, not the different ways of assigning phase and intensity to each point source described in the "optimal", "quasi-optimal" and "realistic" cases. A comparison among the three cases of the same W, NA and FN is shown in Table 4.2.

TABLE 4.2: Comparisons of "optimal","quasi-optimal" and "realistic" cases at $W = 32\,\mu m$

	Optimal	Quasi-optimal	Realistic
Lens span, W	$32\,\mu m$	$32\,\mu m$	$32\,\mu m$
Working wavelength λ	$1.55\,\mu m$	$1.55\,\mu m$	$1.55\,\mu m$
Nominal focal length, $f_{nominal}$	$13.95\,\mu m$	$13.95\,\mu m$	$13.95\,\mu m$
Analytic focal length, $f_{analytic}$	$13.67\,\mu m$	$13.65\,\mu m$	$13.75\,\mu m$
$\lvert f_{analytic} - f_{nominal}\rvert / f_{nominal}$	2.0%	2.2%	1.4%
FWHM	$0.81\,\mu m$	$0.80\,\mu m$	$0.89\,\mu m$

With the expanded W, the three cases have a similar performance, which suggests that the "realistic" lens is not compromised by the phase coverage shortage and intensity variation. In the following discussion, the original $W = 10\,\mu m$ will be continued. This is because that our setup could only offer a laser spot that covers a $W = 10\,\mu m$ planar lens homogeneously with enough power density to be measured by the detector.

4.5.3 Numerical Simulation of Planar Lens

Based on the analytic study in the previous section, numerical simulations are used to demonstrate that different focusing patterns can be realized by this geometrically fixed planar lens. The lens has 21 slits spanning over $10\,\mu m$ laterally, with a 500 nm center-to-center distance between the neighboring slits. The source and boundary conditions used in the FDTD simulations for the 21-slit lenses are the same as for the single slit configuration described previously. Several examples of varied nominal focal positions are chosen for illustration. Firstly, focal points at different positions along the lens axis are investigated, where $f_{nominal}$ is changed while $l_{nominal} = 0$. Then, the shifting of the focus

parallel to the lens plane will be discussed, in which $f_{nominal}$ is fixed while different $l_{nominal}$ values are tested. For all the examples demonstrated in this section, phase $\phi(n)$ is calculated by Eq. 4.2 for a given pair of $f_{nominal}$ and $l_{nominal}$. Then, a GST crystallization level is chosen in the same way used for "realistic" planar lens described in the analytic model.

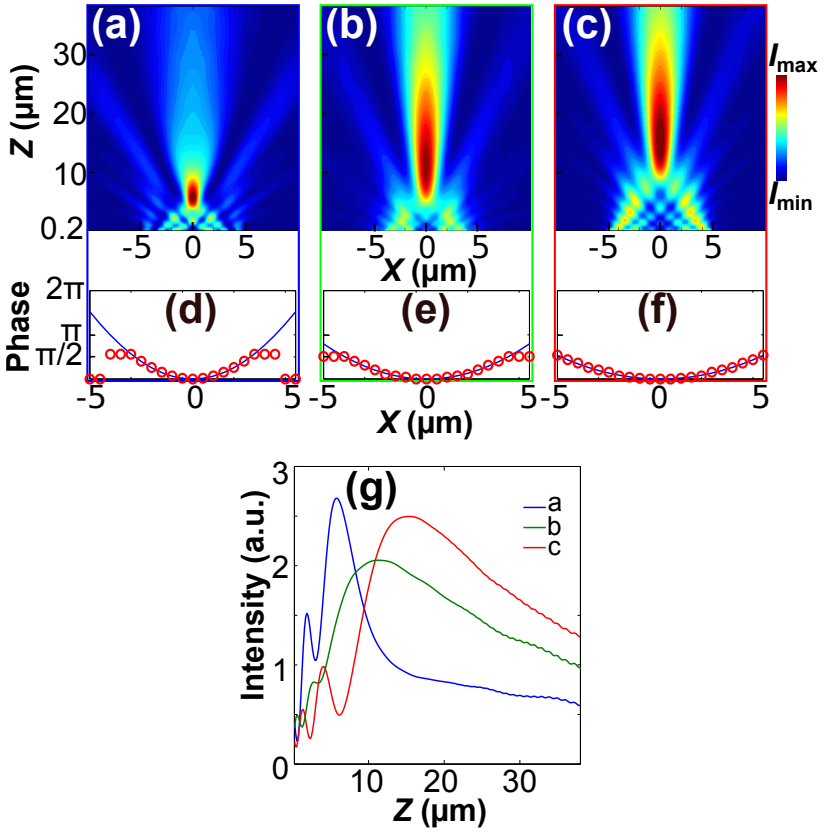

FIGURE 4.17: (a) – (c) Magnetic field distributions of the transmitted field from a slit array with nominal focal lengths of 10, 20 and 30 μm, respectively. (d)–(f) The calculated phase distribution at the sample surface (solid lines) and the discrete phase distribution (red circles) achieved by the GST slits for $f_{nominal}$ = 10, 20 and 30μm. (g) The magnetic field intensities along the lens axis for the three cases (Reprinted from [103]).

Figs. 4.17 a–c illustrate the examples of the longitudinal tuning of the focus. The intensity distributions of the magnetic fields, at $f_{nominal}$ = 10, 20 and 30 μm are plotted. It is clear that the focus is shifted away from the lens as $f_{nominal}$

increases, together with an elongation in the depth of focus. In Figs. 4.17 d-f, the phase fronts obtained from Eq. 4.2 are shown in the solid blue curves, and the discrete phase distributions which are expected to be achieved in the slits are shown in the red circles. From the curves showing the magnetic intensities along the lens axis of the three cases in Fig. 4.17 g, the focal lengths from simulation are found to be 5.8, 11.2, and 15.6 μm, respectively. The deviation between nominal and simulated focal lengths, as a result of small FN associated with this design, was expected [108].

Apart from showing that the focus can be engineered along the lens axis, Figs. 4.18 a-c demonstrate that the lateral shifting of the focus is also feasible. The corresponding ideal phase fronts and engineered discrete phase distributions are shown in Figs. 4.18 d-f. Nominal lateral offsets $l_{nominal}$ are 1, 3 and 5 μm, while $f_{nominal}$ are kept at 20 μm. The intensity distributions of the magnetic field provide a clear evidence of the focus deviating away from the lens axis. The f and l of the three focuses are found to be 0.9 μm and 10.3 μm, 2.1 μm and 11.5 μm, 3.0 μm and 10.8 μm from the simulations, respectively. Fig. 4.18 g, shows the angular-dependent far-field radial component of the time-averaged Poynting vector S_r as a function of the azimuthal angle. It is obvious that a larger $l_{nominal}$ results in a smaller angular aperture. This means a decreased fraction of information is used to reconstruct the focus, therefore, the focusing pattern is expected to degrade at a larger $l_{nominal}$ value.

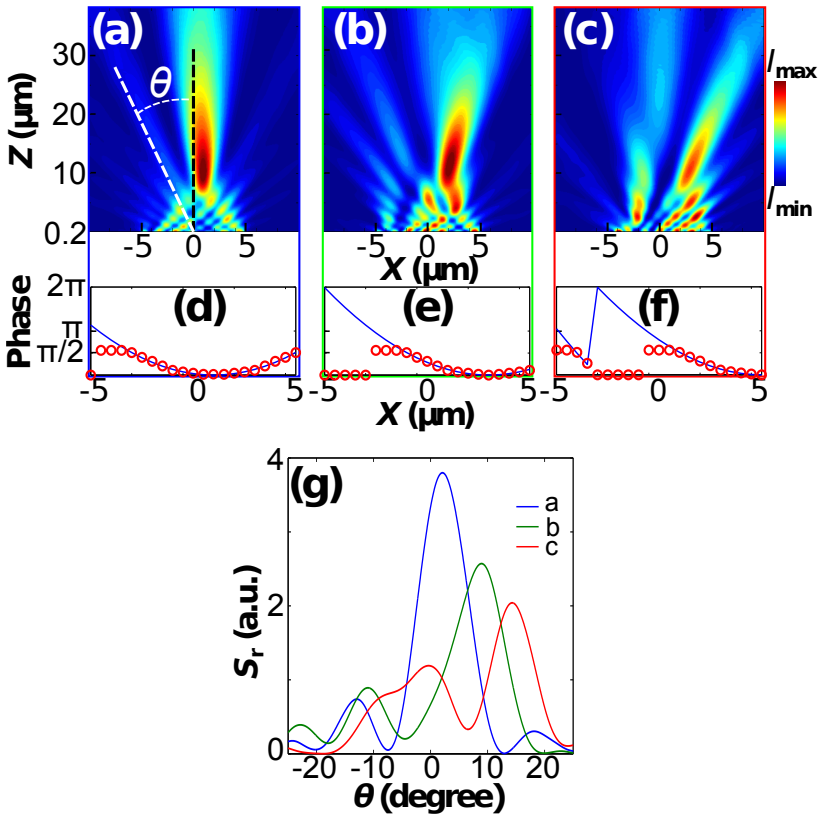

FIGURE 4.18: (a) – (c) Magnetic field distributions of the transmitted field from a slit array with lateral focal offset $X_{nominal}$ equal to 1, 3 and 5 μm, respectively. (d)–(f) The calculated phase distribution at the sample surface (solid lines) and the discrete phase distribution (red circles) achieved by the GST slits for the cases shown in (a)–(c) accordingly. (g) Angular-dependent far-field radial component of the time-avaraged Poynting vector S_r as a function of the azimuthal angle θ (Reprinted from [103]).

4.5.4 Experimental Results of the Planar Lens

A proof-of-concept demonstration of our planar lens is demonstrated in Fig. 4.19. The samples were fabricated by our collaborators, Prof. Luo Xiangang and Dr. Li Xiong from Institute of Optics and Electronics, Chinese Academy of Science, Chengdu, China. The 21 slits were fabricated by focused ion beam (FIB) on a 100 nm-thick gold film as shown in Fig. 4.19 a. Then 100 nm GST was sputtered on the samples covering the entire surfaces. Since our current setup could not

precisely monitor and control the crystallization level of GST inside the slits, the GST being designed to be partially crystallized is now binarized to either amorphous or crystalline phase, depending on whether $\phi(n)$ is more or less than half of the maximum phase modulation value ($0.56\pi/2$). A 4 mW 532 nm-wavelength CW laser was focused on the samples by a 100× objective and scanned along the slits at a speed of 0.2 µm/s to ensure thoroughly crystalized GST inside the slits. As a proof-of-concept demonstration, we illustrate far-field patterns from three samples, namely a control sample without any GST crystallization, followed by two samples with the focal points on and off the lens axis achieved by selectively crystallizing the GST.

Confocal scanning optical microscope (Nanonics Imaging, Ltd.) was used to map the far-field patterns of the samples. The samples were illuminated by a laser beam at 1.55 µm wavelength through the substrate. The laser spot was much larger than the structures. The transmitted field was probed on the other side of the samples by a 50 µm-diameter multimode fiber on the top of a 50× objective lens serving as a pinhole. The photons were collected by an InGaAs IR photon counter over a 15 ms integration time at the other end of the fiber. A piezoelectric stage was used to move the sample in xz-plane.

Fig. 4.19 b shows the focusing pattern of the lens before GST crystallization. Since no variation of crystallization level is introduced among the slits, a nearly flat phase front is expected. As can be seen, the depth of focus is long, exceeding the movement range of the stage in z direction. Fig. 4.19 c shows the lens with

GST crystallized symmetrically about the lens axis. The phase front is a binarized version of the case shown in Fig. 4.17 a ($f_{nominal} = 10\,\mu m$, $l_{nominal} = 0$). Compared with Fig.4.19 b, the entire focus is clearly observed with significantly reduced focal length and depth of focus. This is expected because of the concave phase front created on the top side of the lens. Fig. 4.19 d, with GST crystallized in a binary version rounded from Fig. 4.18 c ($f_{nominal} = 20\,\mu m$, $l_{nominal} = 5\,\mu m$), illustrates an off-axis focus leaning towards the right-hand side. As a result of the asymmetrical phase front about the lens axis, this figure shows a clear sign of lateral tuning. For each case, the calculated phase front and the anticipated discrete phase distributions from the sample are shown in Figs. 4.19 e-g, respectively. Further simulation results based on the experimental conditions, namely using only 0% and 90% crystallized GST that correspond to the binarized discrete phases marked by the red circles in Figs. 4.19 e-g, are shown in the insets of Figs. 4.19 b-d. A relative good agreement is observed between the experimental results and the adapted simulation, exhibiting that the feasibility of our design. The experimental limitations in our setup prevented us from realizing real-time manipulating of GST crystallization level to achieve dynamic tuning of the focus on a single device. However, this issue can be overcome by incorporating electrodes to control GST electrically [39, 63]. In this way, the crystallization level of GST can be accessed by controlling the electric current and it can be monitored by probing the resistance at the same time. The quality of the Fabry-Pérot resonance supported in the GST-slit design can be further improved by employing high-precision planarization technique to remove GST outside of the slits and an optimized GST sputtering process,[109].

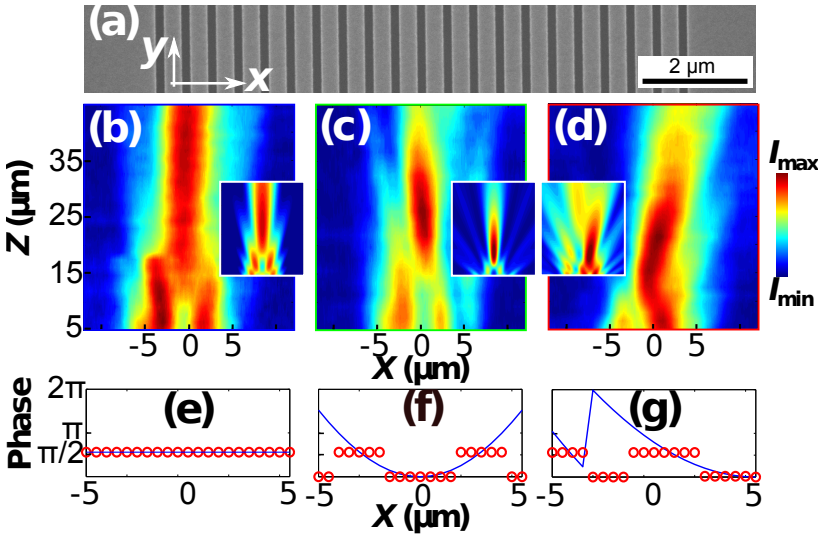

FIGURE 4.19: (a) SEM image of the fabricated planar lens before sputtering GST. (b), (c) and (d) Focusing pattern measured in xz-plane by confocal scanning optical microscopy for amorphous GST in all slits without crystallization, GST being crystallized in the selected slits in an effect to construct phase fronts similar to Figs. 4.17 d and 4.18 f, respectively. Insets of (b), (c) and (d) show the corresponding simulation results of the planar lens in each case using the binarized GST crystallization levels. (e), (f) and (g) The calculated phase fronts $\phi(x)$ (blue curves) and the binarized discrete phase distributions (red circles) which are anticipated from the samples in (b), (c) and (d), respectively (Reprinted from [103]).

4.5.5 Conclusions

A novel planar lens platform working at 1.55 μm by hybridizing the phase-change material GST inside a metallic slit array is demonstrated. The lens can have different focusing patterns without changing the geometry of the structure. Each of the slits supports a strong FP resonance that can be independently shifted across the spectrum by varying the GST crystallization level. The spectral position of the FP resonance in turn determines the phase of the transmitted field at the monochromatic working wavelength. The lens, which consists of 21 such slits, can be engineered to construct phase fronts by assigning the designed GST

crystallization levels to the corresponding slits. Different focusing patterns have been demonstrated using the same geometry numerically, and the preliminary experimental results prove the feasibility of our ideas.

4.6 Summary

In this chapter, tunable nanoscale resonators (nano-disks, nano-bars and nano-slits) has been demonstrated by hybridizing GST into the structures. The large contrast in the optical constant between the amorphous and crystalline GST phases serves as a variable environment, making the spectral shifts of the optical resonances possible. Based on this concept, tunable perfect absorbers that maintain the absorption level above 96% for a tuning range of 650 nm has been shown. Furthermore, the application of GST to the manipulation of hotspot position has been demonstrated on an array of nano-bars excited by monochromatic light. Lastly, phase front engineering has been achieved by selectively shifting the resonances of slits with respect to a fixed working wavelength. This work provides a promising way to realize tunable micro/nano-scaled integrated photonic components, in which extremely flexible and controllable optical responses are required.

Chapter 5

Low-Loss Nanoscale Resonators

Moving forward from the tunable nano-resonators discussed in the previous chapter, low-loss nano-resonators will be investigated in this chapter. As introduced in Chapter 1, current plasmonic materials rely on the free electrons to interact with light. However, the fast scattering rate of the free electrons results in excessive optical losses that significantly limit performance [19, 20]. Polar crystals, on the other hand, support phonon polaritons that interact with light through the vibrations of atoms [20, 36, 48, 110, 111]. A more detailed background of phonon polaritons is provided in Chapter 2. Due to the small damping rate which is about two orders of magnitude lower than plasmon scattering rate in metals, Ohmic losses are significantly reduced in polar crystals.

To investigate the optical performance of phonon polaritons supported by polar crystals in the nanoscale, two types of polar crystals, namely 4H-silicon carbide (SiC) and hexagonal boron nitride (hBN), are considered. SiC nano-pillar arrays are investigated in the first section, followed by the study on hBN nanocones. Samples discussed in this chapter were fabricated by the research groups led by our collaborator Dr. Joshua Caldwell from Naval Research Laboratory in Washington D.C. and Kostya S. Novoselov from University of Manchester in Manchester U.K. The optical modes observed in these nano-resonators are carefully studied, providing the fundamental knowledge for the future designs of phonon polariton-based nanophotonic devices.

5.1 Silicon Carbide Resonators

Silicon carbide is a ceramic material that is widely used in power electronics and optoelectronic applications, as well as a mechanical abrasive and structural material. Recently, due to the low optical losses and Reststrahlen band in the 8-12 μm spectral range, SiC has also become an intriguing material for mid-infrared nanophotonics. The Reststrahlen band of SiC has been studied previously, but the investigations were mainly focused on SiC flakes [36, 112]. This is because nano-patterning on a SiC substrate was observed to induce degradation to the optical performance [113]. Only recently, due to the advances in nanoscale fabrication and improved SiC etching processes, nano-patterning on SiC surface has become feasible [48]. Here, we systematically study the optical response from nano-patterned SiC samples. This work has been published in Ref. [53].

5.1.1 Experimental

To investigate the optical modes supported by nanoscale SiC structures, the simple and basic geometry – nano-pillar array – is chosen. A SEM image of representative sample is presented in Fig. 5.1 a. The SiC nano-pillars were patterned on a semi-insulating SiC substrate followed by our collaborator Dr. Joshua Caldwell. The SiC nano-pillars therefore reside on the SiC substrate, unlike a plasmonic sample in which metal resonators are supported by a substrate of a different material. In this way, the samples are robust and a large aspect ratio (defined as h/d) can be achieved. A zoom-in view of the structure is shown in Fig. 5.1 b with the geometric parameters highlighted. The infrared reflection spectra were collected by a Bruker FTIR with a microscope. The objective lens was a 15× Cassegrain objective with 0.58 NA, which illuminates the sample at a weighted average incident angle of 25°. Finite-element-method-based calculations were performed by using commercial COMSOL multiphysics modeling software. P-polarized plane waves are launched at an incident angle of 25° in the xz-plane to approximate the experimental conditions. The height h was chosen to be 1 μm for all the samples to prevent damping that might occur due to the proximity effect if h is smaller than 800 nm [48]. Several sets of samples with varied diameter d and gap sizes G will be studied to provide a comprehensive picture of the optical modes supported by this geometry.

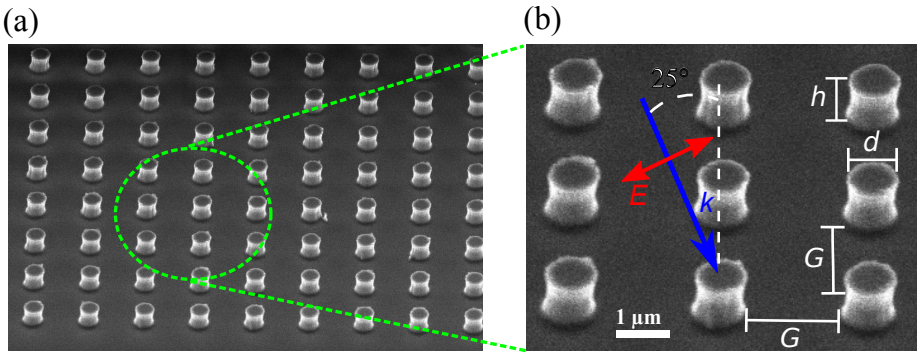

FIGURE 5.1: (a) SEM image of a representative sample showing the periodic SiC nano-pillar array. (b) Zoom-in view of the periodic SiC nano-pillar array with highlights of the geometric parameters (Reprinted from [53]).

5.1.2 Results and Discussion

5.1.2.1 Reflection Spectrum of a SiC Substrate

The optical response from a SiC substrate is studied first to ensure that the COMSOL model is configured correctly. Fig. 5.2 demonstrate the simulated and the measured reflection spectra. The high-reflection window due to the Reststrahlen band can be clearly identified, and a good agreement between the two results can be confirmed.

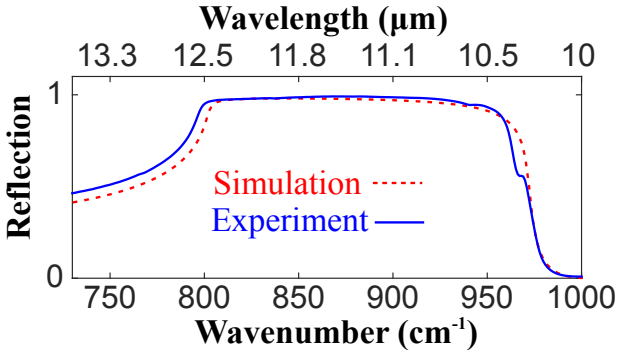

FIGURE 5.2: Simulation result of the reflection spectrum from a SiC slab and the measured reflection spectrum from a SiC wafer. The thickness of SiC in the simulation is set to be 3 μm.

5.1.2.2 Localized SPhP Modes in SiC Nano-pillars

The sample with $h = 1\,\mu\text{m}$, $d = 1\,\mu\text{m}$, $G = 2\,\mu\text{m}$ is used as an example to illustrate the localized surface phonon polaritons (LSPhP) modes. The reflection spectra from both experiment and COMSOL calculation are plotted in Fig. 5.3. Three modes can be identified. To reveal the nature of each modes, the near-field profiles are investigated.

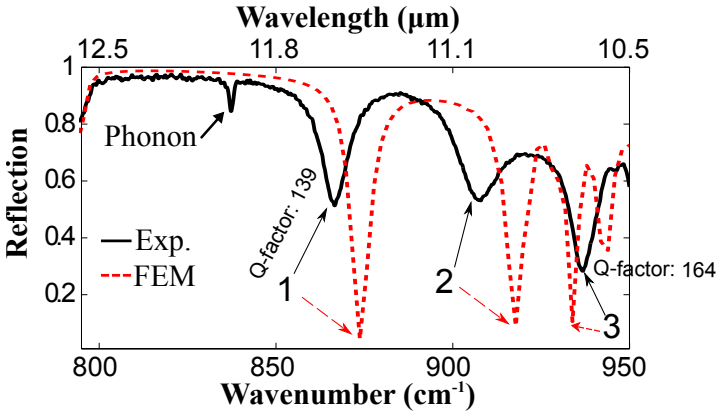

FIGURE 5.3: Experimental (black solid) and FEM (red dashed curve) reflection spectra of 1 μm diameter and 1 μm high SiC nano-pillars in square lattices with a 2 μm interpillar gap (Reprinted from [53]).

Fig. 5.4 shows the near-field profiles of mode 1, which is known as a monopolar mode. The presence of the homogeneous negative permittivity from the underlying SiC substrate enables the stimulation of this mode. As can be observed in Fig. 5.4 a, the charges oscillating along the pillar and on the substrate in its vicinity are counterbalanced by the charges of the opposite sign on a ring at the bottom of the nano-pillar. The charge of the opposite sign at the bottom of the nano-pillar is depicted by the cross section of E_z at $z = -5$ nm below the substrate surface as shown in Fig 5.4 c. It can be regarded as a modified longitudinal mode along the pillar with charge neutrality being provided by the substrate.

Due to its nature as a longitudinal mode, this mode can only be excited by an out-of-plane electric field [48]. As a result of the circularly symmetric charge distribution around the nano-pillars, the near-field profile in the cross-section at $x = 0$ is almost identical to the cross-section at $y = 0$ despite that the incident wave is linearly polarized in the xz-plane, which is clearly shown in Figs 5.4 d and e.

For the other two dips marked by numbers 2 and 3 in Fig 5.3, the charge and near-field distributions are plotted in Figs. 5.5 and 5.6. In contrast to the circularly symmetric charge distribution of the monopole, the charge distributions of these two modes present a clear dipolar pattern, which is due to the electric field component in the x-axis of the incident field. Therefore, these two modes are referred to as transverse dipole 1 (TD1) and transverse dipole 2 (TD2).

5.1.2.3 Size and Interpillar Gap Dependence in Square Lattices

Changing the geometry of a nanostructure is a common and convenient method to fine-tune the spectral response of a nanophotonic system. In this section, the spectral shifts of the three modes supported by the nano-pillar arrays as a function of the gap size G are investigated.

Samples with diameters $d = 0.5\,\mu\text{m}$, $0.75\,\mu\text{m}$ and $1\,\mu\text{m}$ at varied G were measured by FTIR. The spectral evolutions of the SiC nano-pillars arrays for each diameter are shown in Fig. 5.7. The dashed lines serve as a guide to the eye and highlight the spectral shifts of the monopole, TD1 and TD2 as the interpillar gap G increases.

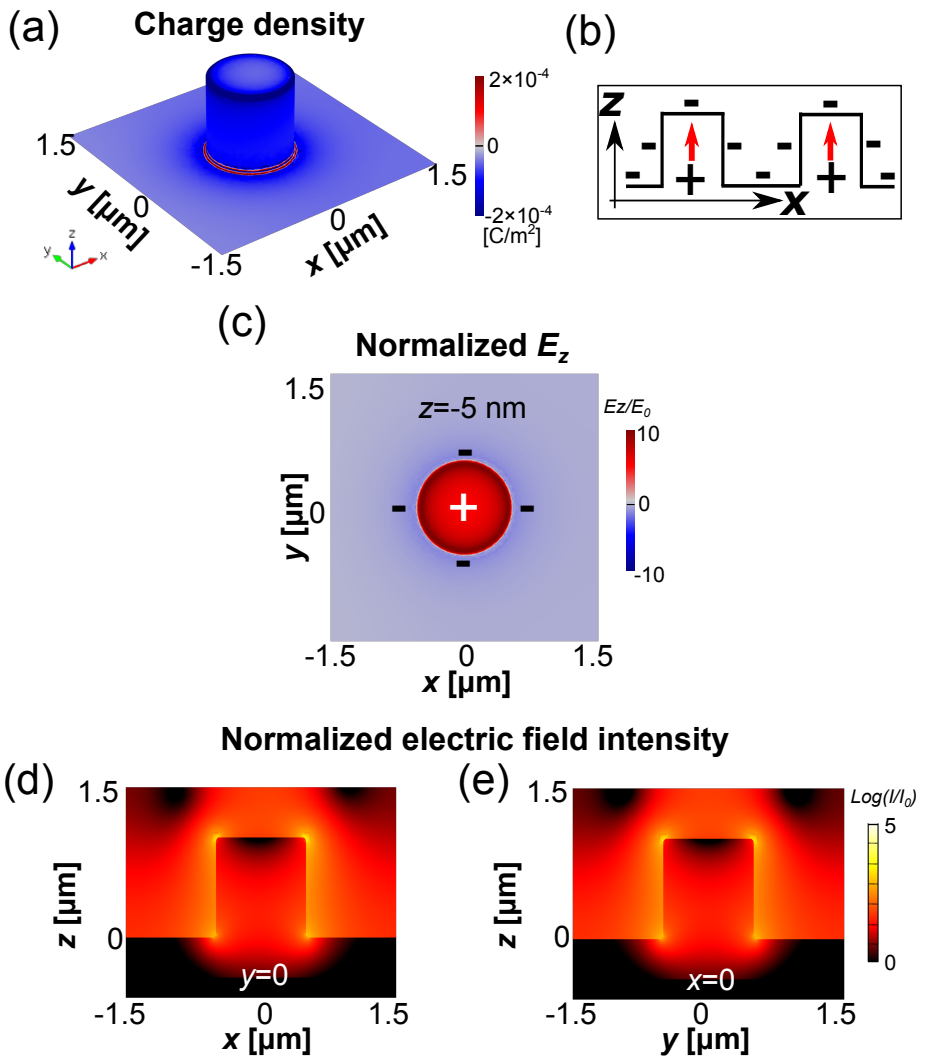

FIGURE 5.4: (a) 3D view of the charge distribution for the monopole mode. Panel (b) shows the schematic charge configurations of two neighbouring pillars for this mode, with '+' and '-' denoting the charges and red arrows showing the electric field direction. (c) Normalized E_z in the xy plane at -5 nm below the surface of the substrate. Please note the color is saturated in order to show the sign flip of E_z. (d) and (e) Normalized electric intensities in the planes $y = 0$ and $x = 0$, respectively. Note that these two cross-sections are extremely similar to each other, despite the fact that the incident field is p-polarized in the xz plane. The charge density and E_z distributions are in linear scale and the electric field intensities are shown in log scale (Reprinted from [53]).

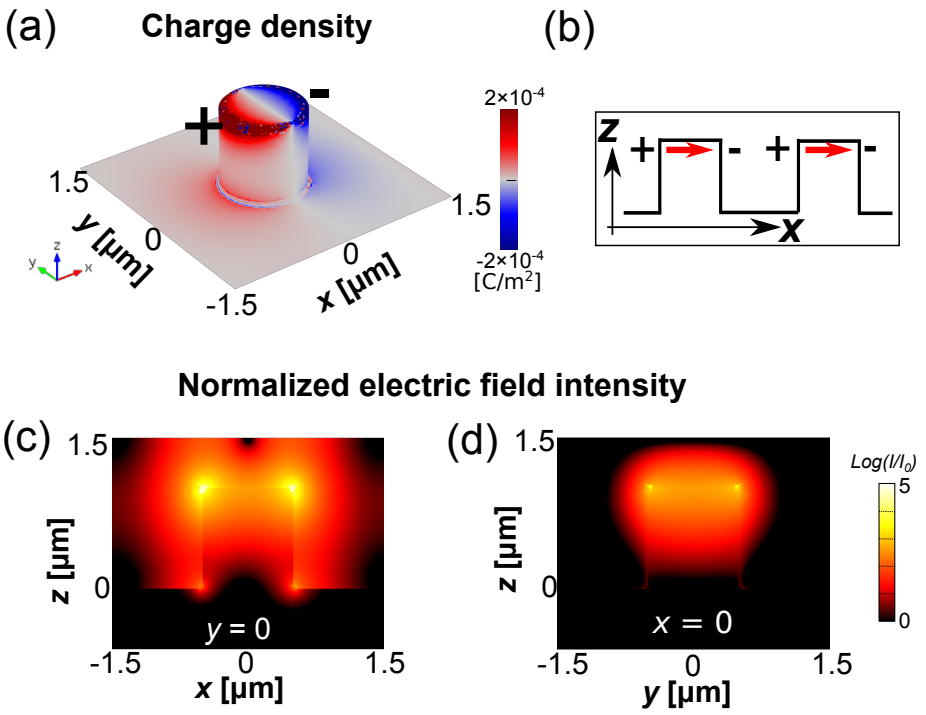

FIGURE 5.5: (a) 3D views of the charge density of the TD1. (b) Schematic of charge distribution of two neighboring pillars in the polarization plane for the mode, with '+' and '-' denoting the charges and red arrows showing the electric field direction. (c) and (d) show the normalized electric field intensity in the $x = 0$ and $y = 0$ planes for the TD1. The charge density distributions are in linear scale and the electric field intensities are shown in log scale (Reprinted from [53]).

In general, the monopole is coincident with TD1 at small gaps and therefore cannot be identified. As G increases, the monopole is observed to red-shift. In contrast, the two dipolar modes blue-shift with increasing G, which is consistent to observations for dipolar plasmonic resonances. To better illustrate their spectral behaviors, the resonant positions of each mode are plotted in Figs 5.8 a-c as a function of G for the corresponding diameters. Furthermore, at a fixed gap size, Figs 5.8 a-c clearly demonstrate that decreasing diameter causes the transverse dipolar modes to shift to higher wavenumbers, while the monopoles are observed to shift towards to lower values. This inverse dependence on G can be explained

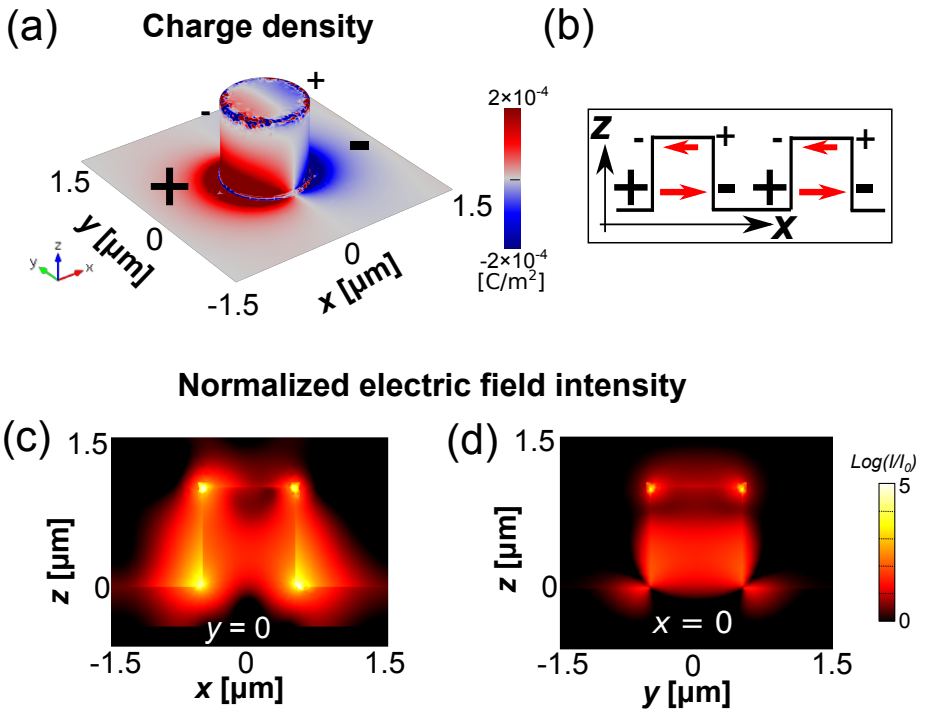

FIGURE 5.6: (a) 3D views of the charge density of the TD2. (b) Schematic of charge distribution of two neighboring pillars in the polarization plane for the mode, with '+' and '-' denoting the charges and red arrows showing the electric field direction. (c) and (d) show the normalized electric field intensity in the $x = 0$ and $y = 0$ planes for the TD2. The charge density distributions are in linear scale and the electric field intensities are shown in log scale (Reprinted from [53]).

by the transverse and longitudinal nature of the resonant modes.

The opposite trends between monopole and transverse dipoles suggest that different near-field coupling mechanisms are associated with these modes. Plasmonic hybridization theory is used to explain the observation [114–117]. Schematic diagrams illustrating the charge distributions are shown in Figs. 5.4 b, 5.5 b and 5.6 b for the monopole, TD1 and TD2 respectively. For the monopolar resonance, adjacent pillars exhibit charge distributions that are of the same sign. Therefore,

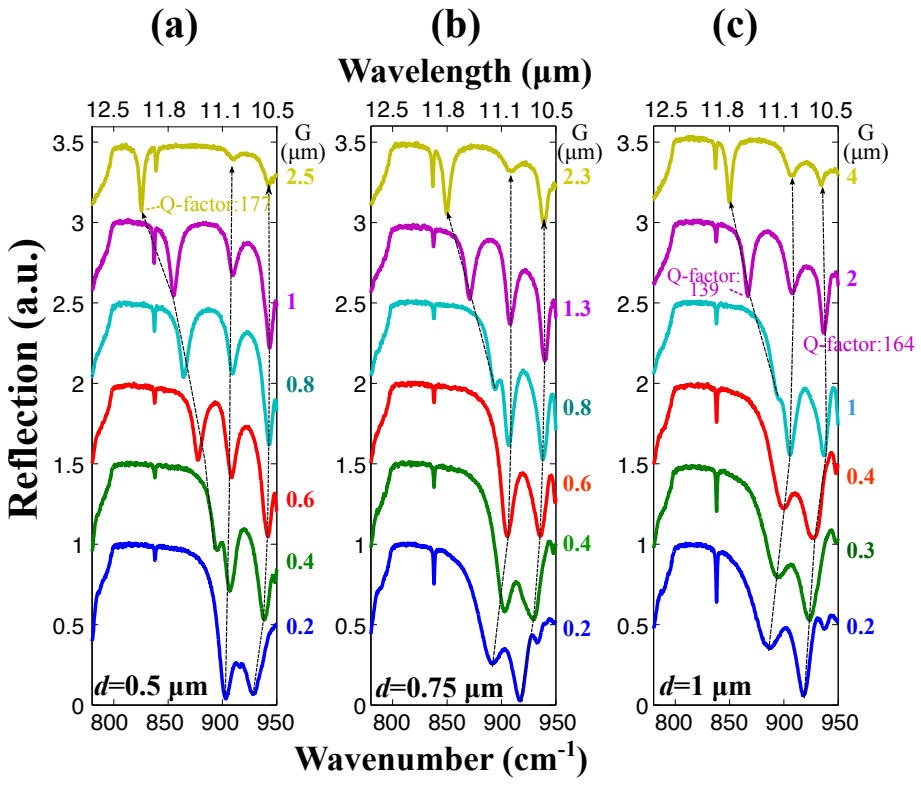

FIGURE 5.7: Evolution of the experimental reflection spectra of the nano-pillar arrays in square lattices as the interpillar gap size changes for a diameter (a) $d = 0.5\,\mu m$, (b) $d = 0.75\,\mu m$ and (c) $d = 1\,\mu m$, respectively (Reprinted from [53]).

decreasing the interpillar gap translates into an increased coulomb repulsion, resulting in a shifting of these modes to a higher energy (a larger wavenumber). For the TD1 and TD2 modes, which are excited by an in-plane electric component of the incident field, they have the charges changing sign across the diameter along x-axis, forming a '+ - + -' configuration between neighbouring nano-pillars. Reductions in interpillar gaps thus result in increased coulomb attraction, shifting these modes to lower frequencies.

To rule out the possibility that diffractive coupling is the cause of the spectral shifts, randomly arranged pillar arrays are considered as control samples. An

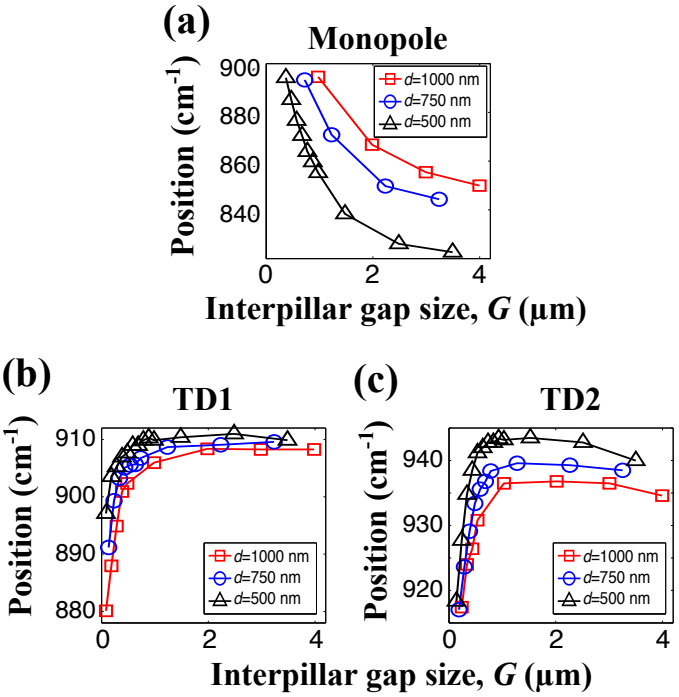

FIGURE 5.8: Spectral positions of (a) monopoles, (b) TDI and (c) TD2 from the experimental reflection spectra of the nano-pillar arrays in square lattices as the function of the interpillar gap size (Reprinted from [53]).

SEM image of such randomly arranged pillar arrays is shown in Fig. 5.9. The reflection spectra of these samples are compared with their periodic counterparts, which are related through the filling fraction (FF). FF is defined as the ratio between the area covered by the pillars and the area of the patterned region, which can be expressed as FF $= \pi d^2/4(G+d)^2$, where d is the diameter of the nano-pillar and G the interpillar gap. From Figure. 5.10, a good agreement between the periodic and random arrays can be observed for each set of samples, which confirms the coupling among the SiC nano-pillars only happens through near-field interactions, instead of diffractive coupling.

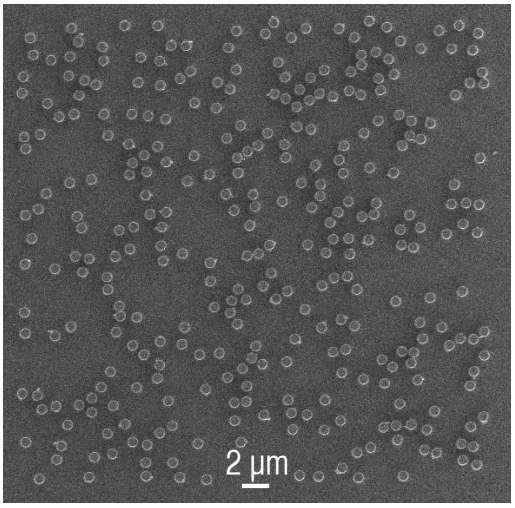

FIGURE 5.9: SEM image of the randomly arranged nano-pillar array with diameter $d = 1\,\mu m$ and FF = 10%.

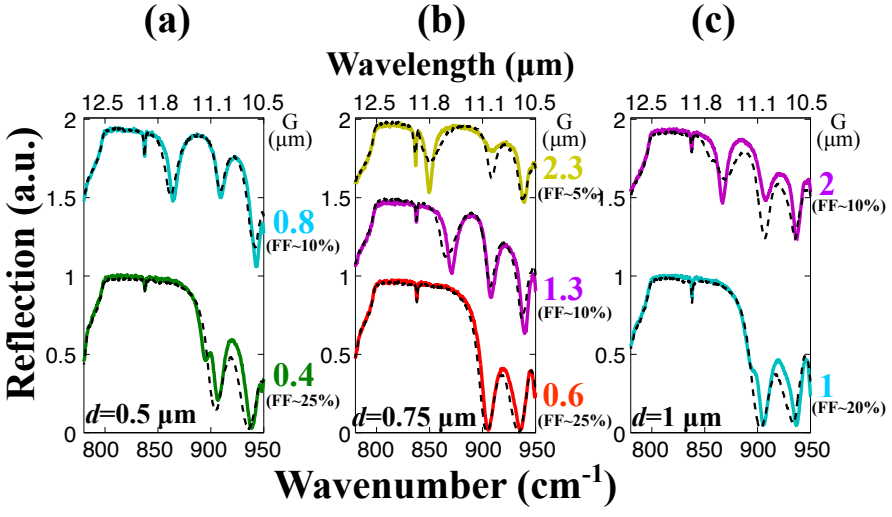

FIGURE 5.10: Reflection spectra of randomly arranged nano-pillar arrays compared with periodic nano-pillar arrays of the same filling fractions.

5.1.2.4 Spectral Tuning of Monopoles with Constant Efficiency

One anomalous behavior of the modes supported by SiC nano-pillars is the constant modal efficiency of the monopolar resonance with large changes in the periodicity or filling fraction. Here, this phenomenon is highlighted by reporting the intensities (estimated as 1-Reflection) as a function of the filling fraction for various diameters, which are plotted in Fig. 5.11. Sharp changes in the in-

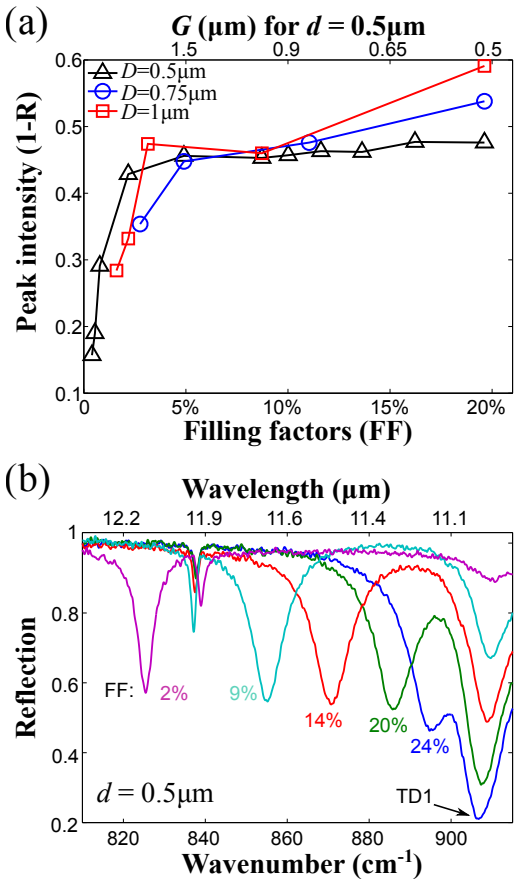

FIGURE 5.11: (a) Intensities of the monopoles calculated by 1-R at the peaks of the experimental spectra as a function of the filling factors. Panel (b) shows the representative spectra from the samples with diameter d =0.5 μm, presenting a nearly constant magnitude. The fractions under the monopoles are the corresponding FFs (Reprinted from [53]).

tensity can be observed at small FF ($< 5\%$), however, the modal amplitude

becomes nearly constant for larger FF over a broad range of nano-pillar densities (5% <FF< 20%). The "constant-intensity" monopole shifts for a range of $\sim$60 cm^{-1}, until the mode merges with TD1 making its identification and quantification of its intensity difficult. For the case of $d = 0.5\,\mu\mathrm{m}$, it is seen that an order of magnitude difference in FF (2% <FF< 20%) leads to a significant spectral shift ($> 60\,\mathrm{cm}^{-1}$), while the mode intensity is nominally constant at about 45%, as shown in Fig. 5.11 b. In contrast, TD1 exhibits a progressive reduction in intensity with the increasing gap size (decreasing FF), as one would intuitively expect.

The reason for such a constant-efficiency behavior of the monopole resonance can be understood from its surface charge distribution. The charged area due to the monopolar resonance covers the nearby substrate surface. When FF is above 5%, these charged areas on the substrate overlap, resulting in a coupled resonance mode that covers the entire surface between the pillars. As the FF decreases below 5%, the distance between pillars is increased, until a point where the surface charged areas no longer overlap and the resonances become nominally independent of each other. Fig. 5.12 demonstrates the charge density distributions of a sample with $d = 0.5\,\mu\mathrm{m}$ and $G = 5\,\mu\mathrm{m}$ (FF=0.65%) as an example. The isolated monopole can be clearly seen in this case. The dashed circle denotes the position of charge density at 1/e of the maximum value, the radius R is about 0.7 µm.

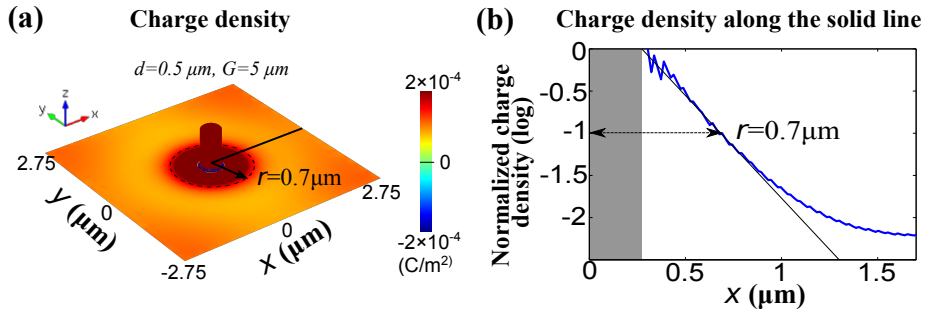

FIGURE 5.12: (a) Simulated charge density distribution of a SiC nano-pillar at its monopolar resonance with diameter $d = 0.5\,\mu m$, interpillar gap $G = 5\,\mu m$ and period=5.5 μm. The dashed circle denotes the position of charge density dropped to 1/e of the maximum value under the effect of the monopole. (b) Normalized charge distribution in logarithmic scale along the solid line in (a), note that -1 corresponds to 1/e in linear scale. The solid black line is a linear fitting to show the charge density close to the pillar decays exponentially (Reprinted from [53]).

5.1.3 Conclusions

SiC nano-pillars attached to a ground-plane have been studied. The monopole exhibits remarkable optical behaviors, with a nearly constant intensity observed despite the variations in the filling fraction (periodicity) over an order of magnitude. This extraordinary property allows an unprecedented spectral tuning. The intriguing mode also demonstrates exceptionally high quality factors. This low-loss property is accompanied by the strong field localization in the inter-resonator space. Moreover, we have provided a detailed study of all the modes supported by these SiC resonators, elucidating their intricate spectral dependence on the geometry through both FTIR spectroscopy and numerical simulations. The coupling among the nano-pillars is mainly through the near-field interaction due to their highly sub-wavelength nature, which has been confirmed by the comparison with random structures. This work has laid the ground work for the design of

future mid-infrared nanophotonics that benefits from the potential of SiC resonators, and enables a wide array of applications, for instance, surface-enhanced spectroscopy in the mid-infrared.

5.2 Hexagonal Boron Nitride Resonators –from Isotropic to Hyperbolic

Nano-resonators made of hyperbolic polar crystal hexagonal boron nitride (hBN) will be discussed in this section. Compared with the isotropic SiC nano-resonators, hBN nano-resonators support exotic hyperbolic modes, which follow rigid directionality and are volume-confined. This work has been published in Ref. [118], and it is the first manuscript demonstrating that hyperbolic nano-resonators can be realized through a natural material.

5.2.1 Introduction to Hyberbolic Materials

Hyperbolic materials are a group of materials in which the principal components of the dielectric tensor have opposite signs [119]. To simplify the discussion, $\epsilon_x = \epsilon_y$ is assumed. Two possible situations of hyperbolic materials can be expected, $\epsilon_{x,y} > 0$, $\epsilon_z < 0$, and $\epsilon_{x,y} < 0$, $\epsilon_z > 0$. The interesting features of such materials can be explained by the iso-frequency surface, which is a plot of all the possible wave vectors k at a single frequency.

The dispersion equation $\frac{k^2}{\epsilon} = (\frac{\omega}{c})^2$ of a conventional medium can be therefore expanded as

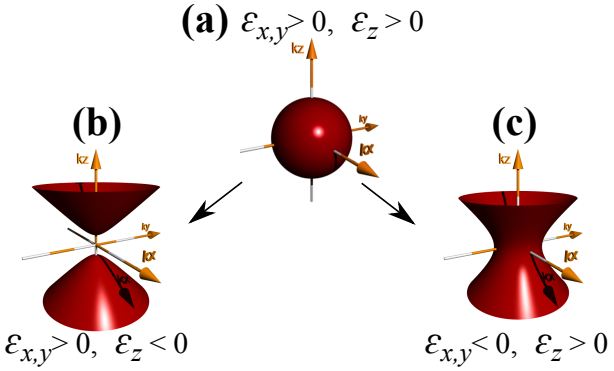

FIGURE 5.13: (a) Conventional dielectric media with $\epsilon_{x,y} > 0$ and $\epsilon_z > 0$ have a closed iso-frequency surface. The iso-frequency surface of a medium with (b) $\epsilon_{x,y} > 0$, $\epsilon_z < 0$ or (c) $\epsilon_{x,y} > 0$, $\epsilon_z < 0$ is an open hyperbolic surface (Reprinted from [118]).

$$\frac{k_x^2 + k_y^2}{\epsilon_z} + \frac{k_z^2}{\epsilon_{x,y}} = (\frac{\omega}{c})^2, \tag{5.1}$$

where $k^2 = k_x^2 + k_y^2 + k_z^2$, ω is the frequency and c is the speed of light in vacuum. By assigning different signs to $\epsilon_{x,y}$ and ϵ_z, the iso-frequency surface drastically changes from a sphere or spheroid with a closed surface into open-surface hyperbolic shapes, which are shown in Fig.5.13. The open-surface nature of the hyperbolic curves suggests that k can be infinitely large. In other words, the hyperbolic medium can support waves propagating at an infinitely small wavelength.

Hyperbolic properties have been previously explored by using artificial materials, for instance, metamaterials of alternating layers of metal and dielectric [34, 120–122]. The possible applications include super-resolution imaging, nanofabrication and cloaking [12, 123, 124]. However, due to the Ohmic losses associated with the metal and the tedious fabrication steps, identifying alternatives

to the man-made materials has been a hot research topic [15].

Hexagonal boron nitride (hBN) is a polar crystal and a van der Waals crystal at the same time, as shown in Fig.5.14. On one hand, it exhibits metal-like optical properties with low losses due to the phonon polaritons supported within its Reststrahlen bands. On the other hand, the layered crystal structure gives rise to an anisotropic permittivity due to different in-plane and inter-layer covalent bonds. With the mentioned properties, hBN appears as a promising candidate of hyperbolic materials in the mid-infrared. In the following sections, the optical properties of hBN and the optical response from the nano-patterned hBN resonators will be discussed.

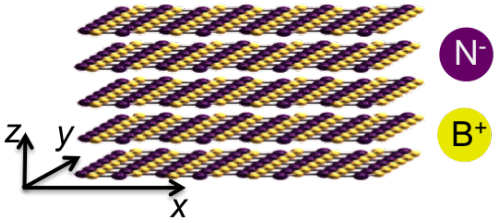

FIGURE 5.14: Schematic drawing of hBN, which is a typical van der Waals crystal consisting of multi atomic planes.

5.2.2 Optical Properties of hBN

Two frequency bands in which hBN shows hyperbolic properties can be identified from its permittivity retrieved from the infrared reflection and transmission spectra. As shown in Fig. 5.15, the upper band starts from 1360 cm^{-1} to 1610 cm^{-1} (6.2 µm to 7.3 µm) and the lower band starts from 760 cm^{-1} to 825 cm^{-1} (12.1 µm to 13.2 µm). In the upper band, $\mathrm{Re}(\epsilon_z) > 0$ and $\mathrm{Re}(\epsilon_{x,y}) < 0$. In the lower band, $\mathrm{Re}(\epsilon_z) < 0$ and $\mathrm{Re}(\epsilon_{x,y}) > 0$. The upper band resembles alternating layers of

metal and dielectric, while the lower band resembles a metamaterial of metal wire arrays embedded in a dielectric medium.

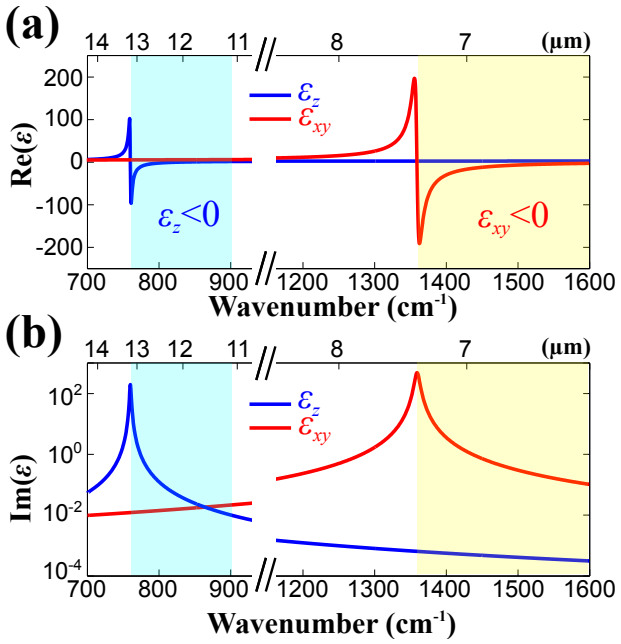

FIGURE 5.15: Real part (a) and imaginary part (b) of the permittivity of a hBN flake along the extraordinary optical axis z (blue curve) and in the xy-plane perpendicular to the extraordinary optical axis (red curve). The band highlighted in blue marks the lower Reststrahlen Band with $\mathrm{Re}(\epsilon_z) < 0$ and the band highlighted in yellow marks the upper Reststrahlen Band with $\mathrm{Re}(\epsilon_{x,y}) < 0$.

5.2.3 Geometry of Nano-patterned hBN

To study the optical response from hBN nano-resonators, the first barrier is to couple the light from the free space into the structures. As illustrated in Fig. 5.16, a momentum mismatch from free space (marked by the red circle) to hBN (marked in blue color) always exists. AFM tip-assisted coupling has been demonstrated in the study of a hBN flake [111]. In our research to investigate the nanoscale hBN structures, the momentum matching can be provided by the sharp edges on the structures themselves. Here, we investigate nano-cone

structures as shown in Fig. 5.17. The important parameters are highlighted, with h representing the height and d_1 (d_2) denoting the top (bottom) diameter.

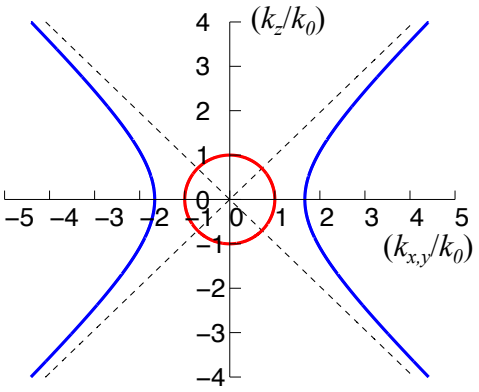

FIGURE 5.16: Typical k-space plot of hBN in the upper Reststrahlen band. A momentum mismatch between free space and hBN always exists in both Reststrahlen bands.

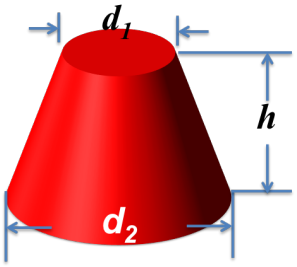

FIGURE 5.17: Schematic drawing of the hBN nanostructure with geometric parameters highlighted.

In the following sections, an array of cones with $d_1 = 200\,nm$, $d_2 = 480\,nm$, $h = 390\,nm$ and a period of $P = 600\,nm$ in both x and y directions are investigated to demonstrate the modes supported by the nano-patterned hBN structures. Samples were fabricated on a hBN flake by our collaborators Dr. Joshua Caldwell, Kostya S. Novoselov and their team members. A SEM image of the sample is shown in Fig. 5.18. FTIR was used to characterize the far-field optical

response. Numerical simulations in COMSOL were used to reveal the nature of the corresponding modes.

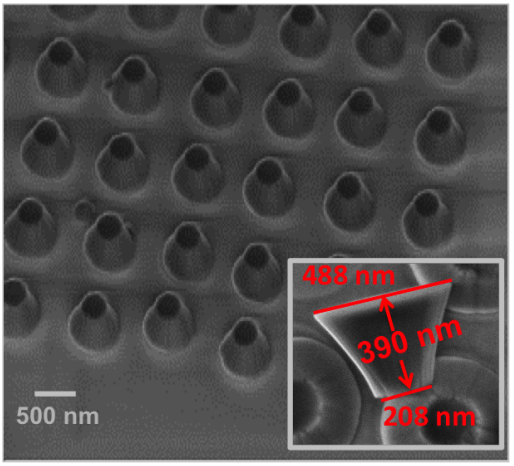

FIGURE 5.18: SEM image of the fabricated hBN nanostructures (Reprinted from [118]).

5.2.4 Modes of Nano-patterned hBN resonators

5.2.4.1 Upper Reststrahlen Band

The upper Reststrahlen band, which is between 1360 cm^{-1} and 1610 cm^{-1} (from 6.2 µm to 7.3 µm), is investigated first. The spectra were collected by three objective lenses. A ZnSe objective with an incident angle less than 2° obtains spectra at near normal incidence, the grazing angle objective (GAO) injects and collects EM waves at large incident angles and the 36× Cassegrain objective provides incident angles close to 25°. The experimental measurements and simulation results are shown in Figs. 5.19 a and b, with a good quantitative agreement. It is obvious that the peaks at small incident angles are more pronounced, and at large incident angles, the modes are suppressed. This observation suggests

that the modes are more efficiently coupled at normal incidence. The modes are named in the form of ${}^{\mathrm{R}}\mathrm{TM}_{ml}$, where R denotes the Reststrahlen band, with 'U' (or 'L') representing upper (or lower) band. TM refers to the transverse magnetic nature of the optical mode, and m and l are the z axis angular momentum and orbital indices, respectively.

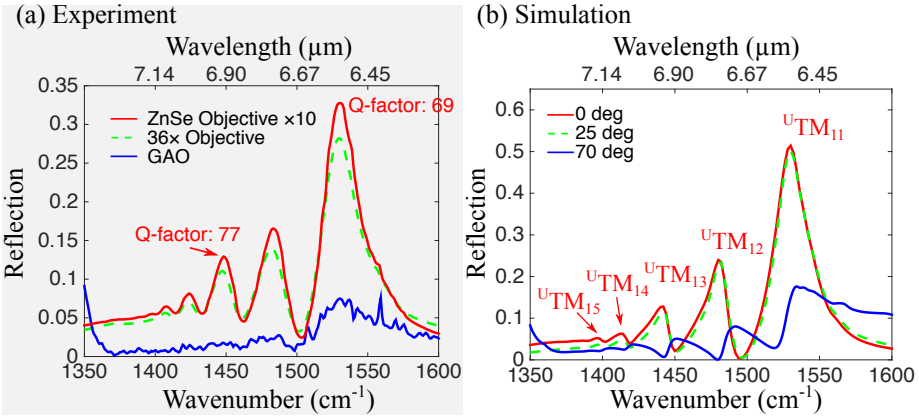

FIGURE 5.19: (a) Measured reflection spectra of the hBN nanostructure array by ZnSe objective (red solid line), 36× Cassegrain objective (green dashed line) and grazing-angle objective (blue solid line) in the upper Reststrahlen Band. (b) The corresponding reflection spectra at normal incidence (red solid line), 25° incidence (green dashed line) and 70° incidence (blue solid line) from numerical simulations (Reprinted from [118]).

The near-fields at the five peaks marked as ${}^{\mathrm{U}}\mathrm{TM}_{11} - {}^{\mathrm{U}}\mathrm{TM}_{15}$ in Fig. 5.19 b are plotted in Fig. 5.20. Unlike a metal nanoparticle that has most of the electric field outside nanoparticles, hBN is a medium that supports propagating modes inside. Therefore, the cross-sections showing the fields inside the nano-cone are chosen to illustrate the modes. These near-fields show a clear cross-hatch patten, and the number of the crosses increases along z axis with the mode order.

To understand the reason for such a near-field pattern, the unique properties associated with hyperbolic materials need to be considered. Based on Eq. 5.1,

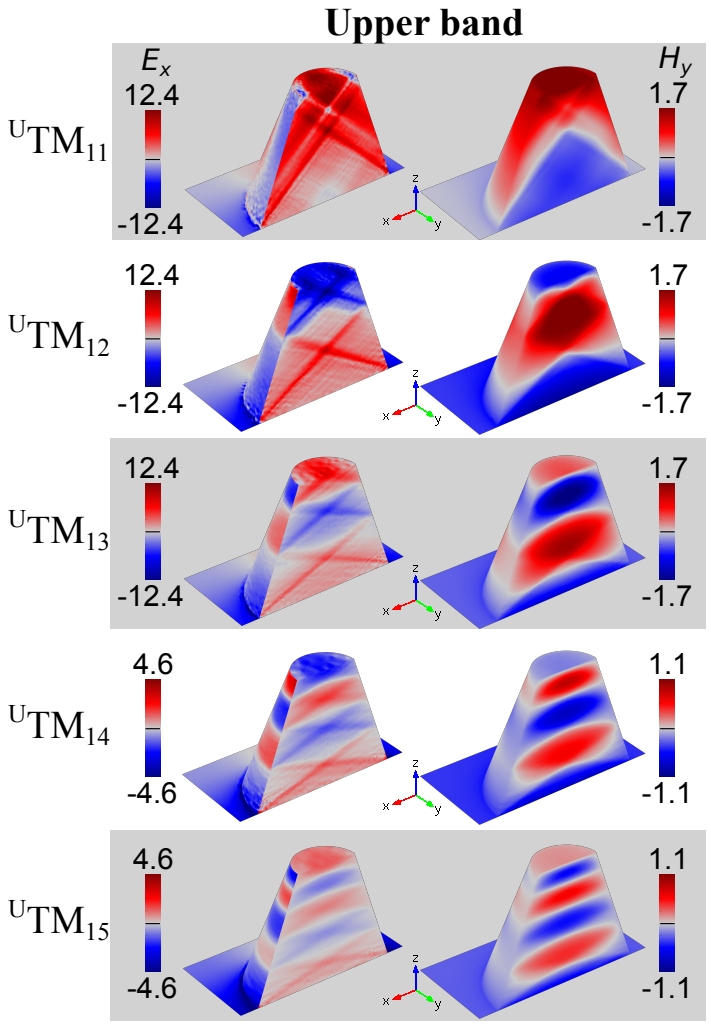

FIGURE 5.20: Near-field distributions of the five modes identified from the simulation at normal incidence (Reprinted from [118]).

if we consider a point with $k \gg k_0$, it corresponds to a point on the hyperbolic surface close to the asymptotic lines. An example has been plotted in Fig. 5.21 a, with four black dots marking the relative positions in k-space of such a mode. It is obvious that at such positions, the ratio between k_z and $k_{x,y}$ can be well estimated as the gradient of the asymptotic lines, in other words, $\frac{k_z}{k_{x,y}} = \sqrt{\frac{-\epsilon_{x,y}}{\epsilon_z}}$. To include the frequency term, the above equation can be further written as

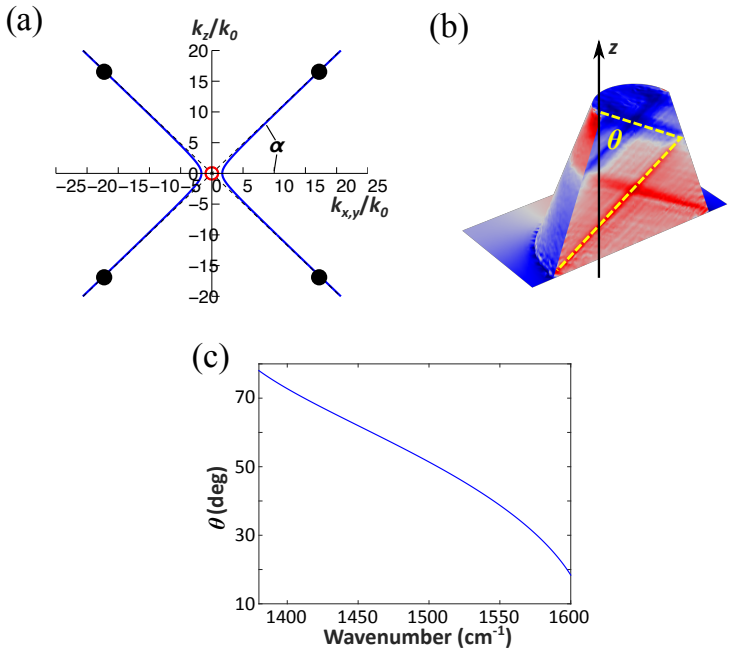

FIGURE 5.21: (a) Typical k-space plot of hBN in the upper Reststrahlen band, with four black dots highlighting the relative position in the k-space of a mode supported by the hBN nano-cone. The red circle marks the k_0 in the free space and α denotes the angle of the asymptotic lines. (b) Electric near-field distribution of the hBN nano-cone, with θ marking the direction of the mode relative to z axis. These two panels are based on the 2nd mode in Fig.5.20. (c) Relation between θ and wavenumber is calculated by Eq.5.3.

$$\frac{k_z}{k_{x,y}} = \sqrt{\frac{-\epsilon_{x,y}(\omega)}{\epsilon_z(\omega)}}, \tag{5.2}$$

Considering the nanoscale geometries of the cones and the wavelength range that the nano-cones are excited ($\sim 7\,\mu$m), the condition $k \gg k_0$ can be regarded as satisfied. The direction of propagation relative to the z axis can be estimated as $\theta = \arctan(\frac{k_z}{k_{x,y}})$ (see Fig. 5.21 b). Combined with Eq.5.2, θ depends solely on the frequency ω, which can be expressed as Eq.5.3.

$$\theta = \arctan(\frac{k_z}{k_{x,y}}) = \arctan(\sqrt{\frac{-\epsilon_{x,y}(\omega)}{\epsilon_z,(\omega)}}) \tag{5.3}$$

By assigning $\epsilon_{x,y}(\omega)$ and $\epsilon_z(\omega)$ with the data shown in Fig. 5.15, the relation between θ and wavenumber can be plotted as shown in Fig. 5.21 c. At small wavenumbers, the angle θ is large, which means multiple cross-hatch patterns can be stacked along z direction in a nano-cone. While at large wavenumbers, θ becomes smaller and therefore the number of cross-hatch patterns in the z direction reduces.

Indeed, the hBN nano-cone works as a Fabry-Pérot (FP) cavity, albeit with the standing wave condition met by the deeply sub-diffractional polariton wavelength, instead of the free-space value. The field inside hBN nano-cone forms a standing wave, and the order of the mode is determined by both the wavenumber (the angle θ) and the geometry (if an integer number of the cross-hatch pattern could be hosted). This geometry factor is taken into consideration by the aspect ratio, which is defined as d_{avg}/h, with $d_{avg} = \sqrt{\frac{1}{3}(d_1^2 + d_2^2 + d_1 d_2)}$. Fig. 5.22 illustrates the spectral positions of the modes supported by the hBN nano-cones as a function of the aspect ratio.

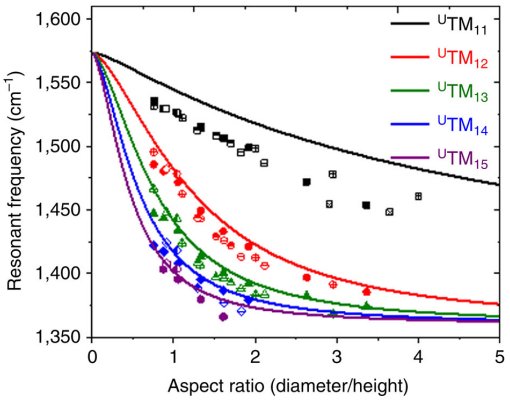

FIGURE 5.22: Spectral positions of the five modes in the upper Reststrahlen band as a function of the aspect ratio (Reprinted from [118]).

5.2.4.2 Lower Reststrahlen Band

In contrast to the upper Reststrahlen band, the spectral response in the lower Reststrahlen band of hBN nano-cones are significantly different. As shown in Fig. 5.23 a, several strong peaks are observed in the spectrum collected by the grazing incidence objective (GAO), while the peaks in the spectra collected by the ZnSe and 36× Cassegrain objectives are weak. This suggests that the interaction between the light and the nanostructure is more intense at a larger incident angle, which corresponds to a more pronounced component E_z parallel to the negative permittivity axis (z-axis). Results from numerical simulations show a good agreement with the experimental data.

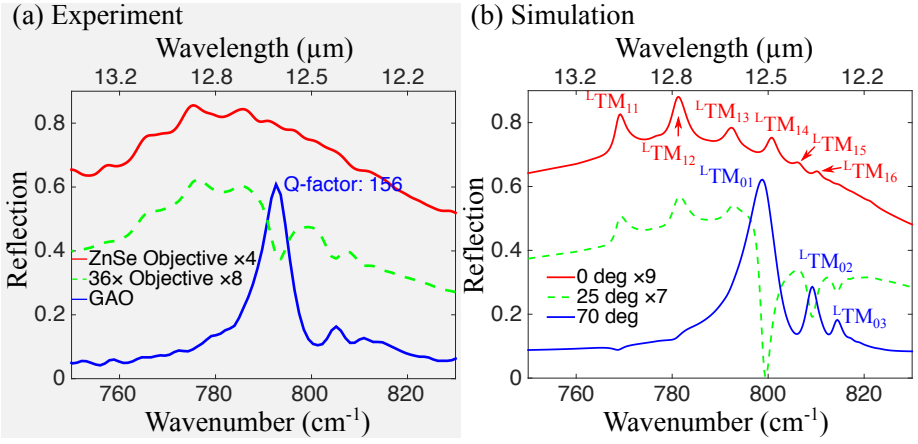

FIGURE 5.23: (a) Measured reflection spectra of the hBN nanostructure array by ZnSe objective (red solid line), 36× Cassegrain objective (green dashed line) and grazing-angle objective (blue solid line) in the lower Reststrahlen Band. (b) The corresponding reflection spectra at normal incidence (red solid line), 25° incidence (green dashed line) and 70° incidence (blue solid line) from numerical simulations (Reprinted from [118]).

The near-field distributions of the weakly coupled modes marked as $^{\mathrm{L}}\mathrm{TM}_{11}$ $-^{\mathrm{L}}\mathrm{TM}_{15}$ under 0° incident angle are plotted in Fig. 5.24. Please note that in the lower band, $\epsilon_{x,y}$ is positive; while in the upper band, $\epsilon_{x,y}$ is negative. Similarities can be

found in the near-fields between the lower band and the upper band. As shown in Fig. 5.24, the cross-hatch patterns can be identified. However, in contrast to the upper band, higher order modes appear at larger wavenumbers.

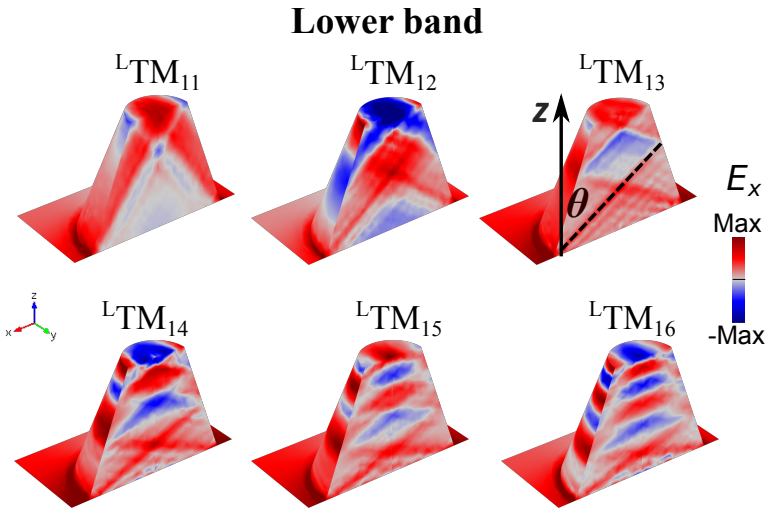

FIGURE 5.24: Near-field distributions of the modes ($^{L}TM_{10}$–$^{L}TM_{16}$) identified from the simulation at normal incident excitation (0°) in the lower Reststrahlen band.

This difference in how the higher order modes shift between the two spectral bands is due to the directionality of modes θ (the angle marked in the inset of Fig. 5.25) as a function of the wavenumber, which is of the opposite trend compared with the upper band. The property can be attributed to the permittivity of hBN. By taking the permittivity of hBN in the lower band into the Eq. 5.3, the trend of θ as a function of wavenumber is revealed in Fig. 5.25.

The near-field distributions of the strongly coupled modes marked as $^{L}TM_{01}$ –^{L} TM_{03} at 70° incident angle are plotted in Fig.5.26. Different from the series of modes discussed above, these modes have no nodes in the x-axis. They are the longitudinal modes with the order increasing in z-axis. Note that z-axis is the only

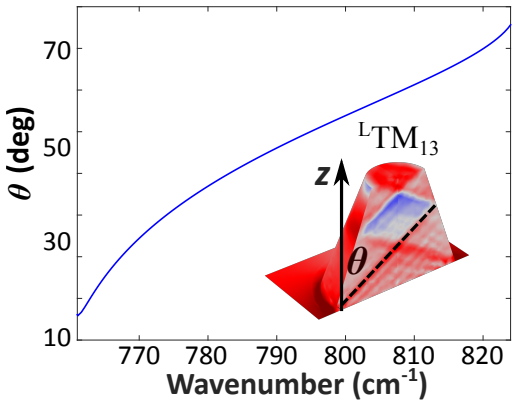

FIGURE 5.25: Relation between θ and wavenumber calculated by Eq.5.3. The inset shows the electric near-field distribution of mode $^{L}TM_{13}$, with θ marking the angle of the cross-hatch pattern relative to z axis.

axis with negative permittivities in the lower band.

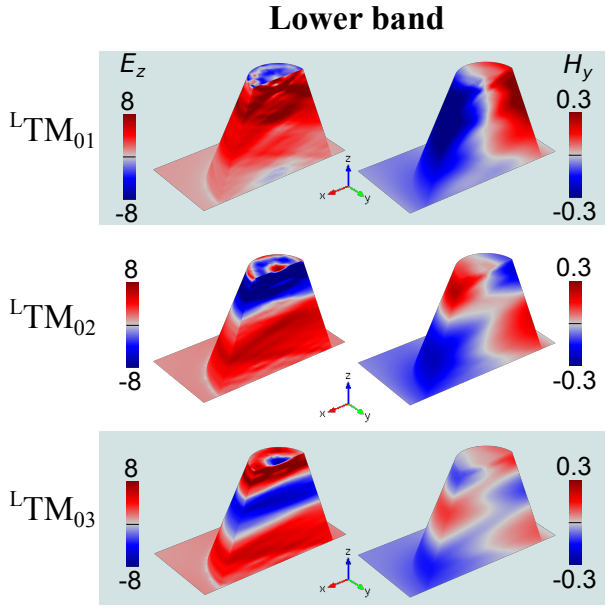

FIGURE 5.26: Near-field distributions of the three modes ($^{L}TM_{01}$–$^{L}TM_{03}$) identified from the simulation at grazing incident angle (70°) in the lower Reststrahlen band (Reprinted from [118]).

5.2.5 Conclusions

To conclude, the optical response of hBN nano-cone arrays has been investigated. Two types of hyperbolic behaviors are studied by investigating different series of hyperbolic modes. Compared with metamaterials, the fabrication steps of the naturally hyperbolic hBN is straightforward. Due to the excitations of phonon polaritons, hBN nano-resonators exhibit narrow resonances with exceptionally high quality factors (> 60 in the upper band and > 150 in the lower band). This low-loss property, together with the volume-confined nature of the optical modes makes hBN attractive for practical applications, such as nanophotonic circuits, flat optics and superresolution imaging.

5.3 Summary

In this chapter, SiC and hBN nano-resonators that support phonon polaritons have been studied, respectively. Exotic modes from isotropic to hyperbolic phonon polaritons have been observed and examined in detail. The ability to confine light into sub-diffractional volumes from these materials has been demonstrated, and the low-loss property has been clearly proven by the large quality factors associated with the resonances. In contrast, gold resonators demonstrate Q-factors ≤ 20 across the frequency range from visible to THz, and the Q-factor of a metal-based hyperbolic structure is ~ 4 [42, 43, 77, 115, 125, 126]. This work has pushed forward the research of phonon polaritons as an alternative

to plasmonics, and serves as guidelines for future nanophotonic devices in the mid-infrared.

Chapter 6

Conclusions

6.1 Conclusions

Tunable and low-loss nano-resonators were studied both theoretically and experimentally in this thesis. As highlighted in the introduction, current approaches to realize functional nanophotonics/plasmonics devices are hampered by a lack of tunability and the inherent losses from charge carrier transport in conductors. Throughout this thesis, new structures and materials were investigated to address these two main issues. Although the solutions provided in this thesis are still at a preliminary stage, they present new options, serving as references and guidelines for future research.

The attempt to achieve tunable nano-resonators were based on phase-change material GST. A thin layer of GST was proposed to be placed in the vicinity of plasmonic resonators to serve as a changeable environment. Firstly, preliminary

tests on a GST film showed significant changes in the transmission spectra as the film was crystallized from the as-deposited amorphous phase. By using effective medium theory, GST at partially crystallized phases can be well modeled. To study the ability of spectrally tuning a plasmonic resonance, GST thin film was placed below an Au nano-disk array. The gradual shifting of the lattice resonance was demonstrated, with a tuning range exceeding 500 nm achieved by a 20 nm-thick GST film. Based on this result, two applications were demonstrated numerically. One is a tunable perfect absorber, which has an absorption peak maintained above 96% with a tuning range of $\sim$ 600 nm. The other one is a plasmonic system that can selectively excite one of five nano-resonators, with a position control of the hotspot at a step resolution about $\lambda/20$. Following the discussion of tunable nanoparticles, a slit in a metal film filled with GST was proposed. Such a design can support a spectrally tunable EOT peak, with a phase modulation of $\sim \pi/2$. A planar lens consisting of 21 slits was constructed, based on which the phase front of the transmitted field was engineered and different focusing patterns were demonstrated.

The other part of the thesis discussed the use of phonon polaritons as a low-loss alternative to plasmonics. As shown in Chapter 2, surface phonon polaritons share a similar dispersion curve with surface plasmon polaritons. Due to the absence of free charge carriers, Ohmic losses are suppressed in phonon polaritons. There were very few studies about phonon polariton modes supported by nano-patterned polar crystals. Therefore, fundamental studies of such nano-resonators were desired. In this thesis, silicon carbide nano-pillar arrays fabricated by Dr.

Caldwell's group were investigated first. The spectral evolution of the peaks as a function of the interpillar gap suggested that two kinds of modes were excited, shifting in the opposite directions when the gaps were enlarged. Near-field distributions from COMSOL simulations confirmed the excitation of monopolar modes which are a special longitudinal mode, and transverse dipoles at either the top or bottom of the pillars. The extraordinary constant extinction of the monopoles was further studied in detail. After this study of SiC, hexagonal BN nano-cones fabricated by the joint efforts of Dr. Caldwell's and Prof. Novoselov's teams were investigated. Two hyperbolic bands were identified and several series of modes were studied in detail at normal incidence as well as grazing-angle incidence. The directionality of the modes and their abnormal scaling were observed and analyzed. The resonances, which due to the reduced losses so that we observed, were coupled with large quality factors (approaching 300) and strong confinement (nanoscale structures with optical responses around 10 μm).

From the results shown in this thesis, it is clear that practical nanophotonic applications can be successfully realized through the combinations of different functional materials, and the continuous effort in identifying alternative low-loss materials. However, there are no general solutions that could solve all the challenges in nanophotonics. Moreover, the capabilities in fabricating more complicated structures of a wide range of materials have to be pushed forward at the same time.

6.2 Future Work

The possible future work includes

1. Phase-change materials and polar crystals can be combined to demonstrate tunable phonon polaritons in the mid-infrared. Based on the work from Ref. [127], a large optical contrast can be obtained around 10 μm in $Ge_3Sb_2Te_6$ between its amorphous and crystalline phases. The wavelength of SiC phonon polaritons is in the similar range, and given its dependence on the dielectric constant of the surrounding environment, $Ge_3Sb_2Te_6$ can be used as the tunable environment for SiC nano-resonators, and different crystallization levels of $Ge_3Sb_2Te_6$ are expected to cause the resonance to shift accordingly. The possible applications of such tunable phonon polaritons include selective thermal absorption, emission, and spectrum-resolved thermal imaging.

2. Dielectric resonators, such as silicon structures, can interact with the magnetic field to support magnetic resonances [128]. The magnetic resonances can be engineered to be at the same frequencies as the monopoles and the transverse dipoles supported by the SiC structures shown in Chapter 5. Combining the silicon resonator and SiC phonon polariton resonator in the same unit cell, extraordinary light manipulations should be achievable because the electric and magnetic components of the incident light can be modulated separately. Possible applications include cloaking and lensing in the mid-infrared [129].

References

[1] R. W. Wood, "On a remarkable case of uneven distribution of light in a diffraction grating spectrum," Proc. Phys. Soc. London **18**, 269–275 (1902).

[2] R. H. Ritchie, "Plasma Losses by Fast Electrons in Thin Films," Phys. Rev. **106**, 874–881 (1957).

[3] A. K. Rengan, M. Jagtap, A. De, R. Banerjee, and R. Srivastava, "Multifunctional gold coated thermo-sensitive liposomes for multimodal imaging and photo-thermal therapy of breast cancer cells," Nanoscale **6**, 916–923 (2014).

[4] M. Fleischmann, P. J. Hendra, and A. J. McQuillan, "Raman spectra of pyridine adsorbed at a silver electrode," Chem. Phys. Lett. **26**, 163–166 (1974).

[5] M. S. Anderson, "Surface enhanced infrared absorption by coupling phonon and plasma resonance," Appl. Phys. Lett. **87** (2005).

[6] A. Alu and N. Engheta, "Achieving transparency with plasmonic and metamaterial coatings," Phys. Rev. E **95**, 16623 (2005).

[7] D. Schurig, J. J. Mock, B. J. Justice, S. A. Cummer, J. B. Pendry, A. F. Starr, and D. R. Smith, "Metamaterial electromagnetic cloak at microwave frequencies," Science **314**, 977–980 (2006).

[8] W. Cai, U. K. Chettiar, A. V. Kildishev, and V. M. Shalaev, "Optical cloaking with metamaterials," Nat. Photonics **1**, 224–227 (2007).

[9] N. Fang, H. Lee, and X. Zhang, "Sub-diffraction-limited optical imaging with a silver superlens," Science **308**, 534–537 (2005).

[10] W. Cai, D. A. Genov, and V. M. Shalaev, "Superlens based on metal-dielectric composites," Phys. Rev. B **72**, 193101 (2005).

[11] Z. Jacob, L. V. Alekseyev, and E. Narimanov, "Optical hyperlens: Far-field imaging beyond the diffraction limit," Opt. Express **14**, 8247–8256 (2006).

[12] Y. Xiong, Z. Liu, and X. Zhang, "A simple design of flat hyperlens for lithography and imaging with half-pitch resolution down to 20 nm," Appl. Phys. Lett. **94**, 19–21 (2009).

[13] E. T. F. Rogers, J. Lindberg, T. Roy, S. Savo, J. E. Chad, M. R. Dennis, and N. I. Zheludev, "A super-oscillatory lens optical microscope for subwavelength imaging," Nature Mater. **11**, 432–5 (2012).

[14] L. Novotny, "Effective wavelength scaling for optical antennas," Phys. Rev. Lett. **98** (2007).

[15] J. B. Khurgin and G. Sun, "Scaling of losses with size and wavelength in nanoplasmonics and metamaterials," Appl. Phys. Lett. **99**, 2009–2012 (2011).

[16] J. B. Khurgin and A. Boltasseva, "Reflecting upon the losses in plasmonics and metamaterials," MRS Bulletin **37**, 768–779 (2012).

[17] P. R. West, S. Ishii, G. V. Naik, N. K. Emani, V. M. Shalaev, and A. Boltasseva, "Searching for better plasmonic materials," Laser Photon. Rev. **4**, 795–808 (2010).

[18] A. Boltasseva and H. A. Atwater, "Low-Loss Plasmonic Metamaterials," Science **331**, 290–291 (2011).

[19] M. Bosman, E. Ye, S. F. Tan, C. a. Nijhuis, J. K. W. Yang, R. Marty, A. Mlayah, A. Arbouet, C. Girard, and M.-Y. Han, "Surface plasmon damping quantified with an electron nanoprobe," Sci. Rep. **3**, 1312 (2013).

[20] J. D. Caldwell, L. Lindsay, V. Giannini, I. Vurgaftman, T. L. Reinecke, S. A. Maier, and O. J. Glembocki, "Low-loss, infrared and terahertz nanophotonics using surface phonon polaritons," Nanophotonics **4** (2015).

[21] J. Y. Ou, E. Plum, J. Zhang, and N. I. Zheludev, "An electromechanically reconfigurable plasmonic metamaterial operating in the near-infrared," Nature nanotech. **8**, 252–255 (2013).

[22] X. Liu and W. J. Padilla, "Dynamic manipulation of infrared radiation with MEMS metamaterials," Adv. Opt. Mater. **1**, 559–562 (2013).

[23] J. Y. Ou, E. Plum, L. Jiang, and N. I. Zheludev, "Reconfigurable photonic metamaterials," Nano Lett. **11**, 2142–2144 (2011).

[24] H. Tao, A. Strikwerda, K. Fan, W. Padilla, X. Zhang, and R. Averitt, "Reconfigurable terahertz metamaterials," Appl. Phys. Lett. **103**, 147401 (2009).

[25] H. T. Chen, W. J. Padilla, J. M. O. Zide, A. C. Gossard, A. J. Taylor, and R. D. Averitt, "Active terahertz metamaterial devices," Nature **444**, 597–600 (2006).

[26] S. H. Mousavi, I. Kholmanov, K. B. Alici, D. Purtseladze, N. Arju, K. Tatar, D. Y. Fozdar, J. W. Suk, Y. Hao, A. B. Khanikaev, R. S. Ruoff, and G. Shvets, "Inductive tuning of Fano-resonant metasurfaces using plasmonic response of graphene in the mid-infrared," Nano Lett. **13**, 1111–7 (2013).

[27] J. Gu, R. Singh, X. Liu, X. Zhang, Y. Ma, S. Zhang, S. A. Maier, Z. Tian, A. K. Azad, H. T. Chen, A. J. Taylor, J. Han, and W. Zhang, "Active control of electromagnetically induced transparency analogue in terahertz metamaterials," Nat. Commun. **3**, 1151 (2012).

[28] T. Driscoll, H. T. Kim, B. G. Chae, B. J. Kim, Y. W. Lee, N. M. Jokerst, S. Palit, D. R. Smith, M. Di Ventra, and D. N. Basov, "Memory metamaterials," Science **325**, 1518–1521 (2009).

[29] T. Driscoll, S. Palit, M. M. Qazilbash, M. Brehm, F. Keilmann, B. G. Chae, S. J. Yun, H. T. Kim, S. Y. Cho, N. M. Jokerst, D. R. Smith,

and D. N. Basov, "Dynamic tuning of an infrared hybrid-metamaterial resonance using vanadium dioxide," Appl. Phys. Lett. **93**, 024101 (2008).

[30] Z. L. Samson, K. F. MacDonald, F. De Angelis, B. Gholipour, K. Knight, C. C. Huang, E. Di Fabrizio, D. W. Hewak, and N. I. Zheludev, "Metamaterial electro-optic switch of nanoscale thickness," Appl. Phys. Lett. **96**, 143105 (2010).

[31] K. Appavoo, D. Y. Lei, Y. Sonnefraud, B. Wang, S. T. Pantelides, S. A. Maier, and R. F. Haglund, "Role of defects in the phase transition of VO2 nanoparticles probed by plasmon resonance spectroscopy," Nano Lett. **12**, 780–786 (2012).

[32] M. J. Dicken, K. Aydin, I. M. Pryce, L. A. Sweatlock, E. M. Boyd, S. Walavalkar, J. Ma, and H. A. Atwater, "Frequency tunable near-infrared metamaterials based on VO2 phase transition," Opt. Express **17**, 18330–18339 (2009).

[33] M. G. Blaber, M. D. Arnold, and M. J. Ford, "A review of the optical properties of alloys and intermetallics for plasmonics," J. Phys.: Condens. Matter **22**, 143201 (2010).

[34] Z. Jacob, I. I. Smolyaninov, and E. E. Narimanov, "Broadband Purcell effect: Radiative decay engineering with metamaterials," Appl. Phys. Lett. **100**, 534–537 (2012).

[35] J. Kim, G. V. Naik, A. V. Gavrilenko, K. Dondapati, V. I. Gavrilenko, S. M. Prokes, O. J. Glembocki, V. M. Shalaev, and A. Boltasseva, "Optical

properties of gallium-doped zinc oxide-a low-loss plasmonic material: First-principles theory and experiment," Phys. Rev. X **3**, 1–9 (2014).

[36] R. Hillenbrand, T. Taubner, and F. Keilmann, "Phonon-enhanced light matter interaction at the nanometre scale," Nature **418**, 159–162 (2002).

[37] N. Yamada, M. Otoba, K. Kawahara, N. Miyagawa, H. Ohta, N. Akahira, and T. Matsunaga, "Phase-change optical disk having a nitride interface layer," Jpn. J. Appl. Phys. **37**, 2104–2110 (1998).

[38] M. Wuttig, D. Lüsebrink, D. Wamwangi, W. Wełnic, M. Gillessen, and R. Dronskowski, "The role of vacancies and local distortions in the design of new phase-change materials," Nature Mater. **6**, 122–128 (2007).

[39] F. Xiong, A. D. Liao, D. Estrada, and E. Pop, "Low-power switching of phase-change materials with carbon nanotube electrodes," Science **332**, 568–570 (2011).

[40] N. Yamada, "Origin, secret, and application of the ideal phase-change material GeSbTe," Phys. Status Solidi B **249**, 1837–1842 (2012).

[41] D. Loke, T. H. Lee, W. J. Wang, L. P. Shi, R. Zhao, Y. C. Yeo, T. C. Chong, and S. R. Elliott, "Breaking the speed limits of phase-change memory," Science **336**, 1566–1569 (2012).

[42] B. Ng, S. M. Hanham, V. Giannini, Z. C. Chen, M. Tang, Y. F. Liew, N. Klein, M. H. Hong, and S. A. Maier, "Lattice resonances in antenna arrays for liquid sensing in the terahertz regime," Opt. Express **19**, 14653–14661 (2011).

[43] X. Yang, J. Yao, J. Rho, X. Yin, and X. Zhang, "Experimental realization of three-dimensional indefinite cavities at the nanoscale with anomalous scaling laws," Nat. Photonics **6**, 450–454 (2012).

[44] S. A. Maier, *Plasmonics: Fundamentals and Applications* (Springer, 2007).

[45] H. Raether, *Surface Plasmons on Smooth and Rough Surfaces and on Gratings*, vol. 111 of *Springer Tracts in Modern Physics* (Springer Berlin Heidelberg, 1988).

[46] W. L. Barnes, A. Dereux, and T. W. Ebbesen, "Surface plasmon subwavelength optics," Nature **424**, 824–830 (2003).

[47] H. Mutschke, A. C. Andersen, D. Clement, T. Henning, and G. Peiter, "Infrared properties of SiC particles," Astronomy & Astrophysics **345**, 187–202 (1999).

[48] J. D. Caldwell, O. J. Glembocki, Y. Francescato, N. Sharac, V. Giannini, F. J. Bezares, J. P. Long, J. C. Owrutsky, I. Vurgaftman, J. G. Tischler, V. D. Wheeler, N. D. Bassim, L. M. Shirey, R. Kasica, and S. A. Maier, "Low-loss, extreme subdiffraction photon confinement via silicon carbide localized surface phonon polariton resonators," Nano Lett. **13**, 3690–3697 (2013).

[49] T. Tiwald, J. Woollam, S. Zollner, J. Christiansen, R. Gregory, T. Wetteroth, S. Wilson, and A. Powell, "Carrier concentration and lattice absorption in bulk and epitaxial silicon carbide determined using infrared ellipsometry," Phys. Rev. B **60**, 11464–11474 (1999).

[50] M. Haraguchi, M. Fukui, and S. Muto, "Experimental observation of attenuated-total-reflection spectra of GaAs/AlAs superlattice," Phys. Rev. B **41**, 1254–1257 (1990).

[51] W. J. Moore and R. T. Holm, "Infrared dielectric constant of gallium arsenide," J. Appl. Phys. **80**, 6939 (1996).

[52] C. F. Bohren and D. R. Huffman, *Surface Modes in Small Particles* (Wiley-VCH Verlag GmbH, 1998), pp. 325–380.

[53] Y. Chen, Y. Francescato, J. D. Caldwell, V. Giannini, T. W. W. Maß, O. J. Glembocki, F. J. Bezares, T. Taubner, R. Kasica, M. Hong, and S. A. Maier, "Spectral tuning of localized surface phonon polariton resonators for low-loss mid-IR applications," ACS Photonics **1**, 718–724 (2014).

[54] E. S. Barnard, J. S. White, A. Chandran, and M. L. Brongersma, "Spectral properties of plasmonic resonator antennas," Opt. Express **16**, 16529–16537 (2008).

[55] J. Z. Zhang and C. Noguez, "Plasmonic optical properties and applications of metal nanostructures," Plasmonics **3**, 127–150 (2008).

[56] K. B. Crozier, A. Sundaramurthy, G. S. Kino, and C. F. Quate, "Optical antennas: Resonators for local field enhancement," J. Appl. Phys. **94**, 4632–4642 (2003).

[57] J. Aizpurua, G. W. Bryant, L. J. Richter, F. J. García De Abajo, B. K. Kelley, and T. Mallouk, "Optical properties of coupled metallic nanorods for field-enhanced spectroscopy," Phys. Rev. B **71** (2005).

[58] V. Giannini, A. I. Fernández-Domínguez, Y. Sonnefraud, T. Roschuk, R. Fernández-García, and S. A. Maier, "Controlling light localization and light-matter interactions with nanoplasmonics," Small **6**, 2498–2507 (2010).

[59] V. Giannini, A. I. Fernández-Domínguez, S. C. Heck, and S. A. Maier, "Plasmonic nanoantennas: fundamentals and their use in controlling the radiative properties of nanoemitters," Chem. Rev. **111**, 3888–3912 (2011).

[60] K. M. Mayer and J. H. Hafner, "Localized surface plasmon resonance sensors," Chem. Rev. **111**, 3828–3857 (2011).

[61] S. Kuiper, H. V. Wolferen, C. V. Rijn, W. Nijdam, G. Krijnen, and M. Elwenspoek, "Fabrication of microsieves with sub-micron pore size by laser interference lithography," J. Micromech. Microeng. **11**, 33–37 (2000).

[62] Q. Xie, M. H. Hong, H. L. Tan, G. X. Chen, L. P. Shi, and T. C. Chong, "Fabrication of nanostructures with laser interference lithography," J. Alloys Compd. **449**, 261–264 (2008).

[63] N. Yamada, "Development of materials for third generation optical storage media," in "Phase change materials: science and applications," , S. Raoux and M. Wuttig, eds. (Springer US, Boston, MA, 2009), chap. 10, pp. 199–226.

[64] H. W. Verleur, A. S. Barker, and C. N. Berglund, "Optical properties of VO2 between 0.25 and 5 eV," Phys. Rev. **172**, 788–798 (1968).

[65] K. Shportko, S. Kremers, M. Woda, D. Lencer, J. Robertson, and M. Wuttig, "Resonant bonding in crystalline phase-change materials." Nature Mater. **7**, 653–8 (2008).

[66] S. Raoux, C. T. Rettner, J. L. Jordan-Sweet, A. J. Kellock, T. Topuria, P. M. Rice, and D. C. Miller, "Direct observation of amorphous to crystalline phase transitions in nanoparticle arrays of phase change materials," J. Appl. Phys. **102**, 094305 (2007).

[67] U. Russo, D. Ielmini, and A. L. Lacaita, "Analytical modeling of chalcogenide crystallization for PCM data-retention extrapolation," IEEE Trans. Electron Devices **54**, 2769–2777 (2007).

[68] N. V. Voshchinnikov, G. Videen, and T. Henning, "Effective medium theories for irregular fluffy structures: aggregation of small particles," Appl. Optics **46**, 4065–4072 (2007).

[69] Y. G. Chen, T. S. Kao, B. Ng, X. Li, X. G. Luo, B. Luk'yanchuk, S. A. Maier, and M. H. Hong, "Hybrid phase-change plasmonic crystals for active tuning of lattice resonances," Opt. Express **21**, 13691–13698 (2013).

[70] V. Weidenhof, I. Friedrich, S. Ziegler, and M. Wuttig, "Atomic force microscopy study of laser induced phase transitions in Ge2Sb2Te5," J. Appl. Phys. **86**, 5879–5887 (1999).

[71] C. H. Chu, C. D. Shiue, H. W. Cheng, M. L. Tseng, H.-P. Chiang, M. Mansuripur, and D. P. Tsai, "Laser-induced phase transitions of

Ge2Sb2Te5 thin films used in optical and electronic data storage and in thermal lithography," Opt. Express **18**, 18383–18393 (2010).

[72] C. M. Chang, C. H. Chu, M. L. Tseng, H. P. Chiang, M. Mansuripur, and D. P. Tsai, "Local electrical characterization of laser-recorded phase-change marks on amorphous Ge2Sb2Te5 thin films," Opt. Express **19**, 9492–9504 (2011).

[73] E. D. Palik, *Handbook of Optical Constants of Solids*, vol. 1 of *Academic Press handbook series* (Academic Press, 1985).

[74] G. Vecchi, V. Giannini, and J. Gómez Rivas, "Surface modes in plasmonic crystals induced by diffractive coupling of nanoantennas," Phys. Rev. B **80**, 201401 (2009).

[75] L. Gross, R. R. Schlittler, G. Meyer, A. Vanhaverbeke, and R. Allenspach, "Fabrication of ultrathin magnetic structures by nanostencil lithography in dynamic mode," Appl. Phys. Lett. **90**, 093121 (2007).

[76] N. I. Landy, S. Sajuyigbe, J. J. Mock, D. R. Smith, and W. J. Padilla, "Perfect metamaterial absorber," Phys. Rev. Lett. **100**, 207402 (2008).

[77] N. Liu, M. Mesch, T. Weiss, M. Hentschel, and H. Giessen, "Infrared perfect absorber and its application as plasmonic sensor," Nano Lett. **10**, 2342–2348 (2010).

[78] H. Zhou, F. Ding, Y. Jin, and S. He, "Terahertz metamaterial modulators based on absorption," Prog. Electromagen. Res. **119**, 449–460 (2011).

[79] B. Zhang, Y. Zhao, Q. Hao, B. Kiraly, I.-C. Khoo, S. Chen, and T. J. Huang, "Polarization-independent dual-band infrared perfect absorber based on a metal-dielectric-metal elliptical nanodisk array," Opt. Express **19**, 15221–15228 (2011).

[80] K. Aydin, V. E. Ferry, R. M. Briggs, and H. A. Atwater, "Broadband polarization-independent resonant light absorption using ultrathin plasmonic super absorbers," Nat. Commun. **2**, 517 (2011).

[81] J. Hendrickson, J. Guo, B. Zhang, W. Buchwald, and R. Soref, "Wideband perfect light absorber at midwave infrared using multiplexed metal structures," Opt. Lett. **37**, 371–373 (2012).

[82] Y. Cui, K. H. Fung, J. Xu, H. Ma, Y. Jin, S. He, and N. X. Fang, "Ultrabroadband light absorption by a sawtooth anisotropic metamaterial slab," Nano Lett. **12**, 1443–1447 (2012).

[83] M. Diem, T. Koschny, and C. Soukoulis, "Wide-angle perfect absorber/thermal emitter in the terahertz regime," Phys. Rev. B **79**, 033101 (2009).

[84] S. Dai, D. Zhao, Q. Li, and M. Qiu, "Double-sided polarization-independent plasmonic absorber at near-infrared region," Opt. Express **21**, 13125–13133 (2013).

[85] J. Yang, F. Luo, T. S. Kao, X. Li, G. W. Ho, J. Teng, X. Luo, and M. Hong, "Design and fabrication of broadband ultralow reflectivity black Si surfaces by laser micro/nanoprocessing," Light Sci. Appl. **3**, e185 (2014).

[86] Y. Chen, X. Li, X. Luo, S. A. Maier, and M. Hong, "Tunable near-infrared plasmonic perfect absorber based on phase-change materials," Photon. Res. **3**, 54–57 (2015).

[87] M. P. Hokmabadi, D. S. Wilbert, P. Kung, and S. M. Kim, "Design and analysis of perfect terahertz metamaterial absorber by a novel dynamic circuit model," Opt. Express **21**, 16455–16465 (2013).

[88] F. Costa, S. Genovesi, A. Monorchio, and G. Manara, "A Circuit-based model for the interpretation of perfect metamaterial absorbers," IEEE Trans. Antennas Propag. **61**, 1201–1209 (2013).

[89] D. Zhu, M. Bosman, and J. K. W. Yang, "A circuit model for plasmonic resonators," Opt. Express **22**, 9809–9819 (2014).

[90] T. S. Kao, Y. G. Chen, and M. H. Hong, "Controlling the near-field excitation of nano-antennas with phase-change materials," Beilstein journal of nanotechnology **4**, 632–637 (2013).

[91] S. Zhang, Z. Ye, Y. Wang, Y. Park, G. Bartal, M. Mrejen, X. Yin, and X. Zhang, "Anti-Hermitian plasmon coupling of an array of gold thin-film antennas for controlling light at the nanoscale," Phys. Rev. Lett. **109**, 193902 (2012).

[92] E. Moreno, F. García-Vidal, and L. Martín-Moreno, "Enhanced transmission and beaming of light via photonic crystal surface modes," Phys. Rev. B **69**, 121402 (2004).

[93] M. Peuker, "High-efficiency nickel phase zone plates with 20 nm minimum outermost zone width," Appl. Phys. Lett. **78**, 2208 (2001).

[94] Y. Wang, W. Yun, and C. Jacobsen, "Achromatic Fresnel optics for wide-band extreme-ultraviolet and X-ray imaging," Nature **424**, 50–53 (2003).

[95] V. Pacheco-Pena, B. Orazbayev, V. Torres, M. Beruete, and M. Navarro-Cia, "Ultra-compact planoconcave zoned metallic lens based on the fishnet metamaterial," Appl. Phys. Lett. **103**, 183507 (2013).

[96] H. J. Lezec, A. Degiron, E. Devaux, R. A. Linke, L. Martin-Moreno, F. J. Garcia-Vidal, and T. W. Ebbesen, "Beaming light from a subwavelength aperture." Science **297**, 820–822 (2002).

[97] Z. Sun and H. K. Kim, "Refractive transmission of light and beam shaping with metallic nano-optic lenses," Appl. Phys. Lett. **85**, 642 (2004).

[98] H. Shi, C. Wang, C. Du, X. Luo, X. Dong, and H. Gao, "Beam manipulating by metallic nano-slits with variant widths," Opt. Express **13**, 6815–6820 (2005).

[99] F. M. Huang, T. S. Kao, V. A. Fedotov, Y. Chen, and N. I. Zheludev, "Nanohole array as a lens," Nano Lett. **8**, 2469–2472 (2008).

[100] L. Verslegers, P. B. Catrysse, Z. Yu, J. S. White, E. S. Barnard, M. L. Brongersma, and S. Fan, "Planar lenses based on nanoscale slit arrays in a metallic film," Nano Lett. **9**, 235–238 (2009).

[101] H. Gao, J. K. Hyun, M. H. Lee, J.-C. Yang, L. J. Lauhon, and T. W. Odom, "Broadband plasmonic microlenses based on patches of nanoholes," Nano Lett. **10**, 4111–4116 (2010).

[102] T. S. Kao, E. T. F. Rogers, J. Y. Ou, and N. I. Zheludev, ""Digitally" addressable focusing of light into a subwavelength hot spot," Nano lett. **12**, 2728–2731 (2012).

[103] Y. Chen, X. Li, Y. Sonnefraud, A. I. Fernández-Domínguez, X. Luo, M. Hong, and S. A. Maier, "Engineering the phase front of light with phase-change material based planar lenses," Sci. Rep. **5**, 8660 (2015).

[104] J. Porto, F. Garcia-Vidal, and J. Pendry, "Transmission resonances on metallic gratings with very narrow slits," Phys. Rev. Lett. **83**, 2845–2848 (1999).

[105] A. Fernández-Domínguez, F. García-Vidal, and L. Martín-Moreno, "Resonant transmission of light through finite arrays of slits," Phys. Rev. B **76**, 235430 (2007).

[106] M. Beruete, M. Navarro-Cia, S. A. Kuznetsov, and M. Sorolla, "Circuit approach to the minimal configuration of terahertz anomalous extraordinary transmission," Appl. Phys. Lett. **98**, 014106 (2011).

[107] E. Hecht, *Optics* (Addison Welsey, San Francisco, 2002).

[108] P. Ruffieux, T. Scharf, H. P. Herzig, R. Völkel, and K. J. Weible, "On the chromatic aberration of microlenses," Opt. Express **14**, 4687–4694 (2006).

[109] W.-C. Ren, B. Liu, Z.-T. Song, Y.-H. Xiang, Z.-T. Wang, B.-C. Zhang, and S.-L. Feng, "Nano-scale gap filling and mechanism of deposit—etch—deposit process for phase-change material," Chin. Phys. B **21**, 115203 (2012).

[110] T. Wang, P. Li, B. Hauer, D. N. Chigrin, and T. Taubner, "Optical properties of single infrared resonant circular microcavities for surface phonon polaritons," Nano Lett. **13**, 5051–5055 (2013).

[111] S. Dai, Z. Fei, Q. Ma, A. S. Rodin, M. Wagner, A. S. McLeod, M. K. Liu, W. Gannett, W. Regan, K. Watanabe, T. Taniguchi, M. Thiemens, G. Dominguez, A. H. Castro Neto, A. Zettl, F. Keilmann, P. Jarillo-Herrero, M. M. Fogler, and D. N. Basov, "Tunable phonon polaritons in atomically thin van der Waals crystals of boron nitride," Science **343**, 1125–1129 (2014).

[112] T. Taubner, "Near-field microscopy through a SiC superlens," Science **313**, 1595 (2006).

[113] N. Ocelic and R. Hillenbrand, "Subwavelength-scale tailoring of surface phonon polaritons by focused ion-beam implantation," Nature Mater. **3**, 606–609 (2004).

[114] B. Auguié and W. Barnes, "Collective resonances in gold nanoparticle arrays," Phys. Rev. Lett. **101**, 143902 (2008).

[115] N. J. Halas, S. Lal, W. S. Chang, S. Link, and P. Nordlander, "Plasmons in strongly coupled metallic nanostructures," Chem. Rev. **111**, 3913–3961 (2011).

[116] P. Alonso-Gonzalez, M. Schnell, P. Sarriugarte, H. Sobhani, C. Wu, N. Arju, A. Khanikaev, F. Golmar, P. Albella, L. Arzubiaga, F. Casanova, L. E. Hueso, P. Nordlander, G. Shvets, and R. Hillenbrand, "Real-space mapping of Fano interference in plasmonic metamolecules," Nano Lett. **11**, 3922–3926 (2011).

[117] J. D. Caldwell, O. Glembocki, F. J. Bezares, N. D. Bassim, R. W. Rendell, M. Feygelson, M. Ukaegbu, R. Kasica, L. Shirey, C. Hosten, and C. E. T. Al, "Plasmonic nanopillar arrays for large-Area, high-enhancement surface-enhanced Raman scattering sensors," ACS Nano **5**, 4046–4055 (2011).

[118] J. D. Caldwell, A. V. Kretinin, Y. Chen, V. Giannini, M. M. Fogler, Y. Francescato, C. T. Ellis, J. G. Tischler, C. R. Woods, A. J. Giles, M. Hong, K. Watanabe, T. Taniguchi, S. A. Maier, and K. S. Novoselov, "Sub-diffractional volume-confined polaritons in the natural hyperbolic material hexagonal boron nitride," Nat. Commun. **5**, 5221 (2014).

[119] S. V. Zhukovsky, O. Kidwai, and J. E. Sipe, "Physical nature of volume plasmon polaritons in hyperbolic metamaterials," Opt. Express **21**, 14982–14987 (2013).

[120] C. L. Cortes, W. Newman, S. Molesky, and Z. Jacob, "Quantum nanophotonics using hyperbolic metamaterials," J. Opt. **14**, 063001 (2012).

[121] Y. Guo, W. Newman, C. L. Cortes, and Z. Jacob, "Applications of hyperbolic metamaterial substrates," Adv. Optoelectron. **2012**, 452502 (2012).

[122] S. A. Biehs, M. Tschikin, and P. Ben-Abdallah, "Hyperbolic metamaterials as an analog of a blackbody in the near field," Phys. Rev. Lett. **109**, 104301 (2012).

[123] Z. Liu, H. Lee, Y. Xiong, C. Sun, and X. Zhang, "Far-field optical hyperlens magnifying sub-diffraction-limited objects," Science **315**, 1686 (2007).

[124] S. Ishii, A. V. Kildishev, E. Narimanov, V. M. Shalaev, and V. P. Drachev, "Sub-wavelength interference pattern from volume plasmon polaritons in a hyperbolic medium," Laser Photon. Rev. **7**, 265–271 (2013).

[125] T. Driscoll, G. O. Andreev, D. N. Basov, S. Palit, S. Y. Cho, N. M. Jokerst, and D. R. Smith, "Tuned permeability in terahertz split-ring resonators for devices and sensors," Appl. Phys. Lett. **91**, 062511 (2007).

[126] R. Singh, I. A. I. Al-Naib, M. Koch, and W. Zhang, "Sharp Fano resonances in THz metamaterials," Opt. Express **19**, 6312–6319 (2011).

[127] A.-K. U. Michel, D. N. Chigrin, T. W. W. Maß, K. Schönauer, M. Salinga, M. Wuttig, and T. Taubner, "Using low-loss phase-change materials for mid-infrared antenna resonance tuning," Nano Lett. **13**, 3470–3475 (2013).

[128] J. C. Ginn, I. Brener, D. W. Peters, J. R. Wendt, J. O. Stevens, P. F. Hines, L. I. Basilio, L. K. Warne, J. F. Ihlefeld, P. G. Clem, and M. B. Sinclair, "Realizing optical magnetism from dielectric metamaterials," Phys. Rev. Lett. **108**, 1–5 (2012).

[129] J. Valentine, J. Li, T. Zentgraf, G. Bartal, and X. Zhang, "An optical cloak made of dielectrics," Nature Mater. **8**, 568–571 (2009).